USGS-OFR-91-357

UNITED STATES

DEPARTMENT OF THE INTERIOR

GEOLOGICAL SURVEY

GEOPHYSICAL LOGS FROM A COPPER OXIDE DEPOSIT, SANTA CRUZ PROJECT, CASA GRANDE, ARIZONA

by

Philip H. Nelson

Open-File Report 91-357

Denver, Colorado
1991

ABSTRACT

A joint industry-government project, cosponsored by the Santa Cruz Joint Venture[1] and the U.S. Bureau of Mines, is investigating the use of in-situ leaching to recover copper from an oxide ore deposit near Casa Grande, Arizona. Chemical solutions will be circulated through boreholes penetrating the deposit so that copper may be dissolved from chrysocolla and atacamite, put into solution, and brought to surface. At this stage, test holes have been drilled and logged, and some preliminary hydrological tests have been completed. Objectives of the logging effort are to provide information regarding structure, fracturing, alteration mineralogy, and properties related to fluid flow. In this report we compile and explain the core and log data and then illustrate the progress made thus far towards the objectives.

Using logging technology developed for the petroleum industry, Schlumberger has acquired a complete suite of logs in five 9 7/8-inch rotary boreholes, including caliper, density, neutron, electrical resistivity, dipmeter, gamma spectrometry, sonic waveform, and neutron activation spectrometry. The USGS acquired logs in a nearby 3.6-inch corehole, including caliper, neutron, resisitivity, gamma-ray, sonic velocity, induced polarization, and magnetic susceptibility. Asarco and the USBM have contributed geological description, copper and other elemental analyses, fracture density, and mineralogical estimates.

The data set is unique in that neutron-induced gamma-ray spectrometry logs have been collected for the first time in a mineral deposit. These logs provide direct estimates of the elements Al, Cl, Ca, S, Si, Fe, and Ti. Natural gamma-ray spectrometry adds K, U, and Th. Atacamite, a chlorine-bearing mineral, is the main copper oxide ore in the deposit. Although copper has not been detected directly as an element, it can be predicted with good accuracy using chlorine and other logs.

Mineral concentrations can be estimated by applying an element-to-mineral transformation, although this requires that the elemental concentrations be well determined. In our case, the presence of casing and cement corrupted the elemental determinations. The elemental concentrations were recalculated through the artifice of setting the calcium concentration (contributed almost totally by the cement) to zero, and the mineral transform was then applied. Use of such transformations required that the suite of permissible minerals be carefully restricted and that the results be calibrated against geological and petrological data. After such comparisons were made, the mineral computations produced reasonable estimates of quartz, potassium feldspar, and clay within the granite host rock.

The granite is pervasively fractured, so fractures are expected to control porosity and permeability and to be related to the intensity of alteration. Correlations among sonic velocity, rock strength (mechanical tests on core), and alteration indicators (neutron and potassium logs) demonstrate a very close linkage between the state of alteration and the mechanical state of the rock. Spinner logs of borehole flow during injection were used to ascertain permeable zones. These flow logs were made after the holes were cased and perforated, and hence were influenced by the condition of the perforations. Various indicators of flow from open-hole logs were compared to the flow logs. At this stage of the investigation, sonic properties (velocity and attenuation) appear to be the best indicator of flow. The sonic properties generally demarcate zones where fluid left the borehole during the injection tests, but the correspondence is not sufficiently good that either attenuation or velocity can be used as a reliable predictor of permeability.

[1] The Santa Cruz Joint Venture is a joint venture between wholly owned subsidiaries of ASARCO Incorporated and Freeport McMoRan Inc.

CONTENTS

INTRODUCTION

A series of holes has been drilled into the Santa Cruz ore body to conduct a pilot study of in-situ leaching of a copper oxide ore body. The pilot project is being conducted by the U. S. Bureau of Mines and the Santa Cruz Joint Venture. The Santa Cruz Joint Venture, the owner of the property, is a joint-venture partnership of subsidiaries of ASARCO Incorporated and Freeport-McMoRan Incorporated. The site is located about 7 miles west of Casa Grande, Arizona.

In brief, the project plan is to inject acid into a central injection hole of a "five-spot" pattern (hole T-3 in figure 1) and recover copper-bearing solution in the four surrounding holes. The copper oxide minerals atacamite and chrysocolla are present between 1200 and 1800 feet subsurface. Dissolution of these minerals by sulfuric acid forms copper sulfate in solution. Efficient injection, dissolution, and recovery rests on a number of geological factors including the disposition of copper minerals along fractures and pores where it is accessible to fluid flow, adequate permeability of the rock to conduct fluids, and the absence of major fracture zones more permeable than bulk rock so that fluids do not preferentially flow through a small portion of the total mineralized volume.

Geophysical logs were obtained in cored hole C-1 and in five rotary holes T-1 through T-5. In this report we discuss the logs obtained in these holes along with a variety of geological, mineralogical, and geochemical data. The logs can furnish information relevant to the success of the leach project; specifically, insights and data on structure, alteration, fracturing, porosity, and permeability are desired. The logs can be displayed in profiles across the five-spot to show variations in physical properties.

Many of these logs have never before been acquired on a mining property. Among the oil-field logs run in the large 10-inch T-holes drilled for injection and tracer tests were neutron-induced gamma spectrometry. These logs provide estimates of the concentration of six key elements. Aluminum concentration is provided by a separate system and K, U, and Th are provided by natural gamma-ray spectrometry. Thus a total of 10 elements are measured continuously with depth.

All data, whether geophysical, geological, mineralogical, or chemical, were entered as "curves" into a data base. Conceptually, a curve is a string of values extending from top to bottom of the borehole interval, stored at a spatial density determined by the densest data set. Well logging software makes it easy to organize and plot disparate data types as long as they are available as curves. A curve can be a gamma-ray log, bulk density from core measurements, or an elemental concentration from chemical analysis. We now describe the sources of data that were entered as curves into the well log data base.

SOURCES OF DATA

Geological Units

Four lithology types recognized in core were entered as curves: granite, granite breccia, diabase, and quartz monzonite porphyry. The following explanations were furnished by ASARCO. Granite is the typical Precambrian granite of southern Arizona (Ruin Granite and Oracle Granite are commonly used names). Laramide biotite quartz feldspar porphyry intrusive rocks are lumped under the heading of quartz monzonite porphyry. Diabase is premineral, occurring as dikes and sills. Granite breccia is unclassified breccia. Geological units observed in the cored holes are presented as recorded on the geological log. In the T-holes, rather than use the geological observations based on cuttings, the diabase sill and other occurrences were picked from the openhole logs.

Copper Assays

Copper assay values (weight percent copper) were divided among the copper minerals visible in hand specimen. Values stored in a curve named "atacamite" are actually "weight percent copper in atacamite". Values for chrysocolla, copper-in-plagioclase, and chalcocite are treated similarly. On log plots, the four copper curves can be plotted singly or cumulatively. When plotted cumulatively, the maximum value represents the total weight percent copper as determined by chemical assay.

Alteration Products

Three categories of mineral species observed in core were entered as curves: total limonite, sericite plus clay, and biotite. Values are in volume percent. Wherever "tr" (trace) occurred, we entered a value of 0.5%. Alteration mineralogy from visual observation was available only from holes C-1 and C-2. Observations for SC-19, an older borehole, were in a different format and available only for the lower portion of the hole, and are not presented here. Only cuttings were available from the rotary-drilled T-holes. Alteration minerals such as clay, sericite, and limonite are ground into fines and thus are not readily discernible in the drilling mud. Consequently, no data on alteration mineralogy from the T-holes are presented.

Mechanical Properties

Visual inspection of the core reveals that the core is highly fractured. Even the intact lengths of core are highly fractured, with fracture densities often as high as several to ten per centimeter. Mechanical integrity is preserved by the healing of these microfractures with various minerals including copper and iron oxides. Where copper oxides occur, they are predominantly distributed on fracture surfaces and can be observed as thin arcuate lines where fractures intersect the surface of the core.

Two measures of rock strength were logged by ASARCO geologists. A "rock quality designation" (RQD) was determined to be equal to the cumulative length of pieces of core greater than four inches in length divided by the total footage in a core run. A piece of core was not counted if it was determined to be of extremely low strength by the criterion listed below.

A more detailed classification of rock strength was based on the scheme shown in Table 1.

Table 1. Classification of rock strength, attributed to R. Cummings of ASARCO.

Code	Core Strength
6	Very high strength (3 blows with hammer)
5	High strength (2 blows to fracture)
4	Medium strength (one blow to fracture)
3	Low strength (one slight blow to fracture)
2	Very low strength (breaks by hand)
	Extremely low strength (may be fault gouge)
1.0	Granular (fragments with no cohesion)
0.8	Firm (can make impression with thumb)
0.6	Slightly firm (impression with thumb)
0.4	Soft (impression with slight pressure)
0.2	Very soft (molded with fingers)

The numerical code was assigned to intervals of core in the core run. A core run could be any length up to the 10-foot length of the core barrel. The total length of core recovered was designated "ftrecv". The numerical code for the weakest core that comprised one foot or more of the recovered core was assigned the name "wkindx"; its length is called "wkftg". The average numerical code for the core not included in the weakest footage was called "wkinav"; by subtraction its length is "ftrecv-wkftg". From these values a single strength index was computed by prorating the wkftg and wkinav parameters according to their footage,

$$\text{strngth} = \text{wkindx}*\text{wkftg}/\text{ftrecv} + \text{wkinav}*(\text{ftrecv}-\text{wkftg})/\text{ftrecv}$$

In addition to the strength data, zones of faulting noted by the geologist were simply entered as a 0 (no fault) or a 1 (fault) into a log curve called "fault".

Fracture data were collected in hole T-1 with a borehole video camera and analyzed by L. Dahl of the U. S. Bureau of Mine. Dip angle was not determined because in most cases only a portion of the fracture was visible on the borehole wall. However, the dip azimuth (direction of dip vector relative to true north) was determined and entered as a curve, although it is not presented in this report.

Porosity Data

Samples were selected from cored holes C-2 and SC-19 for determination of density and porosity. The samples had been split with a core splitter and weighed between 100 to 500 grams. Measurements were performed in the Petrophysical Laboratory of the USGS in Denver and by the USBM in Minneapolis. At the USGS laboratory, samples were dried overnight in an oven at 90°C, then weighed. Saturation was carried out under vacuum for 24 hours or until bubbling stopped, then weighed. To determine the volume, the saturated sample was suspended in a tared pan of water, and the pan reweighed. By Archimede's principle, the weight difference is equal to the sample volume. Inspection of the weights measured by the two laboratories indicated lower saturation was attained by the USBM, and a volume displacement method used by the USBM to determine volume was less precise than the weight method; consequently, data from the USBM are not presented here. Data from the USGS are given in Table 2.

Note the close agreement in both the average density and porosity values from the two holes, given at the bottom of the tables.

Table 2. Density and porosity of 59 samples; measurements by U.S. Geological Survey. Density of dry and saturated samples designated by rhod and rhos; grain density, rhog; porosity, por.; average, aver.; standard deviation, stddv.

	Borehole C-2					Borehole SC-19			
Depth feet	Rhod g/cc	Rhos g/cc	Rhog g/cc	Por. %	Depth feet	Rhod g/cc	Rhos g/cc	Rhog g/cc	Por. %
1602.0	2.60	2.64	2.70	4.0	1629.0	2.52	2.58	2.70	6.7
1611.0	2.54	2.62	2.76	7.9	1630.0	2.59	2.64	2.72	4.7
1619.0	2.40	2.48	2.62	8.3	1643.0	2.50	2.55	2.63	5.1
1626.0	2.37	2.46	2.61	9.2	1643.5	2.47	2.54	2.64	6.3
1639.0	2.47	2.54	2.64	6.4	1645.0	2.48	2.52	2.60	4.7
1639.5	2.45	2.51	2.61	6.4	1655.0	2.59	2.63	2.71	4.2
1650.0	2.49	2.54	2.63	5.5	1675.0	2.54	2.58	2.65	4.2
1656.0	2.54	2.59	2.67	4.9	1679.0	2.52	2.57	2.64	4.4
1656.5	2.61	2.66	2.75	4.8	1689.0	2.34	2.46	2.66	11.9
1668.0	2.35	2.46	2.62	10.2	1697.0	2.57	2.61	2.67	3.6
1678.0	2.48	2.53	2.60	4.6	1704.0	2.59	2.66	2.78	6.9
1686.0	2.44	2.54	2.70	9.5	1709.0	2.57	2.60	2.65	2.9
1694.0	2.23	2.39	2.66	16.1	1723.0	2.72	2.76	2.82	3.5
1700.0	2.40	2.50	2.65	9.2	1732.0	2.41	2.50	2.64	8.7
1707.0	2.53	2.61	2.75	8.0	1742.0	2.60	2.68	2.81	7.2
1724.0	2.43	2.51	2.65	8.5	1746.0	2.42	2.50	2.63	8.0
1732.0	2.48	2.54	2.62	5.3	1756.0	2.49	2.55	2.64	5.9
1763.0	2.51	2.59	2.72	7.7	1764.0	2.46	2.54	2.69	8.3
1773.0	2.45	2.53	2.68	8.6	1769.0	2.63	2.73	2.94	10.7
1783.0	2.50	2.55	2.63	5.1	1778.0	2.34	2.48	2.71	13.6
1792.0	2.55	2.61	2.71	6.1	1784.0	2.39	2.52	2.75	12.9
1800.0	2.36	2.45	2.59	9.1	1798.0	2.31	2.44	2.64	12.5
1810.0	2.47	2.55	2.68	7.6	1799.0	2.32	2.46	2.68	13.6
1819.0	2.50	2.55	2.63	4.8	1800.0	2.51	2.58	2.71	7.5
1826.5	2.42	2.49	2.62	7.8	1808.0	2.45	2.51	2.61	6.1
1836.5	2.69	2.78	2.97	9.5	1821.0	2.41	2.50	2.64	8.7
1845.0	2.47	2.54	2.67	7.5	1831.0	2.42	2.53	2.72	10.8
					1837.0	2.33	2.45	2.66	12.6
					1837.5	2.28	2.42	2.64	13.4
					1839.0	2.47	2.53	2.62	5.5
					1858.0	2.50	2.53	2.59	3.5
					1860.0	2.57	2.61	2.68	3.9
Aver.	2.47	2.55	2.67	7.5	Aver.	2.48	2.55	2.68	7.6
StdDv.	0.09	0.08	0.08	2.5	StdDv.	0.11	0.08	0.07	3.5

Petrological Data

Petrological data were made available by the U. S. Bureau of Mines (table 3) from inspection of thin sections cut from samples from cored hole SC-19. The data were used to establish the mineral suite for computations based on Schlumberger's geochemical tool.

In subsequent discussions with H. Kreis of ASARCO and D. Earley of USBM, it was concluded that plagioclase is completely altered to other minerals in the granite. Consequently, plagioclase was deleted from the list of minerals present in the granite. However, some calcium was detected in the granite by the Schlumberger neutron activation tool. If plagioclase is indeed nil, then what mineral contains calcium? With further petrographic microprobe inspection, D. Earley (pers. comm.) found that calcium is present in smectites, at about the 5 to 8% level. As smectite is a small proportion of whole rock, the calcium percentage is quite low, as confirmed by chemical analysis (see section "chemical data").

Table 3. Modal mineralogy (volume % of total minerals) from cored hole SC-19 from petrographic examination by U. S. Bureau of Mines staff. Conventions: atacamite, ata; biotite, bio; chrysocolla, chry; mostly kaolinite, clay; chlorite, chl; mostly goethite, feox; jarosite, jar; orthoclase, kspr; plagioclase, plag, quartz, qrtz; sericite, ser; mostly leucoxene, tiox. Bottom line (rhomn) gives densities assigned to each mineral so that grain density (rhog, righthand column) could be computed for each sample.

Depth	Ata	Bio	Chry	Clay	Chl	Feox	Jar	Kspr	Plag	Qrtz	Ser	Tiox	Rhog
1286	0.0	1.5	4.4	13.2	0.7	3.4	0.0	29.1	0.4	46.8	0.5	0.0	2.68
1288	1.3	0.0	1.4	5.1	0.0	0.8	0.0	31.2	3.1	41.9	15.1	0.1	2.68
1305a	4.4	1.3	4.4	3.4	1.7	2.5	0.0	31.9	1.3	46.5	2.5	0.0	2.71
1305b	0.0	1.1	8.6	1.1	1.9	0.7	0.0	61.5	2.7	14.2	8.1	0.0	2.60
1278	6.4	0.2	0.9	13.0	0.0	1.6	0.0	26.3	5.8	33.9	11.0	0.9	2.76
1383	0.2	0.1	0.9	4.8	0.0	1.4	0.0	29.5	2.7	54.7	5.7	0.0	2.66
1391	0.0	0.0	0.1	1.5	0.0	0.2	0.0	13.3	1.0	70.2	13.3	0.3	2.67
1213	0.0	0.0	1.1	3.4	0.0	0.1	0.0	65.2	1.3	17.2	11.5	0.2	2.62
1675a	16.0	0.0	0.0	2.1	0.3	0.9	0.0	8.8	0.0	52.1	19.5	0.3	2.88
1675b	4.8	0.0	0.0	1.1	0.0	2.9	0.0	28.3	0.0	49.2	13.2	0.4	2.77
1377	0.0	0.0	0.9	7.6	0.9	1.7	0.0	41.5	1.1	29.8	16.2	0.2	2.67
1384	0.0	0.0	0.2	1.6	2.7	3.3	0.0	51.6	1.1	32.0	7.3	0.2	2.70
1401	0.0	1.7	0.2	18.1	1.0	0.8	0.0	28.5	9.5	37.0	3.0	0.2	2.65
126Mw	0.0	0.0	7.7	0.4	0.0	2.4	0.4	44.4	0.0	39.8	4.9	0.0	2.65
1279	2.6	0.0	4.6	1.5	0.0	2.0	0.7	40.7	0.0	35.8	12.1	0.0	2.70
1686	15.7	0.0	0.0	0.0	0.0	0.4	0.0	35.0	0.0	38.9	9.9	0.0	2.82
1750	3.4	0.0	0.0	5.6	0.0	2.6	0.7	20.4	0.0	38.8	28.5	0.0	2.79
1277	5.6	0.0	1.6	8.4	0.2	1.8	0.0	25.5	9.6	40.6	6.6	0.0	2.73
1407a	0.0	0.0	5.4	1.1	0.0	4.9	8.0	47.1	0.1	31.7	1.3	0.4	2.83
1407b	0.0	0.0	1.2	8.7	0.3	3.2	5.5	51.3	0.3	28.9	0.3	0.3	2.76
1407c	0.0	0.0	6.1	2.6	0.0	5.9	9.2	45.0	0.1	30.2	0.6	0.3	2.87
rhomn	3.76	2.90	2.20	2.59	2.80	4.80	4.30	2.57	2.69	2.65	2.83	4.25	

The modal mineralogy provides an opportunity to compute grain density. To do so, handbook values of mineral density were assigned to each mineral; these are tabulated as "rhomn" in the bottom row of Table 3. The sum of the products of mineral density times mineral volume percent then yields the grain density; these are tabulated as "rhog" in the right-hand column of Table 3.

Mineral Composition

Chemical formulae for the minerals identified in Table 3 are given in Table 4, with plagioclase excepted. These formulae will be useful when discussing the relationships between geochemical logs and mineralogy.

Table 4. Chemical composition of selected minerals.

Atacamite	$Cu_2Cl(OH)_2$
Chrysocolla	$CuSiO_32H_2O$
Kaolinite	$Al_2Si_2O_5(OH)_4$
Sericite	$KAl_3Si_3O_{10}(OH)_2$
Goethite	$FeO(OH)$
Hematite	Fe_2O_3
Pyrite	FeS_2
Jarosite	$KFe_3(OH)_6(SO_4)_2$
Biotite	$K(Mg,Fe)_3AlSi_3O_{10}(OH)_2$
Orthoclase	$KAlSi_3O_8$
Quartz	SiO_2

Chemical Data

Chemical analyses were performed on 14 composite samples from cored hole C-2 (Table 5), by inductively-coupled plasma emission. Selection of sample intervals was based on the character of alteration mineralogy from observation of core. Each element was entered as a curve in the well log data base.

Table 5. Elemental analysis (weight %) of composited samples from cored hole C-2 by Skyline Labs, Inc., Tucson, Arizona, October 1990. Loss on ignition (LOI) represents volatiles driven off by heating to 900°C.

Depth	SiO_2	Al_2O_3	MgO	CaO	Na_2O	K_2O	MnO	Fe_2O_3	Cl	CO_2	LOI
1205-1247	74.6	13.1	0.26	0.07	0.32	5.7	0.01	2.0	0.15	0.00	1.6
1247-1351	76.3	12.3	0.23	0.10	0.38	5.6	0.01	1.5	0.10	0.00	2.1
1351-1400	74.6	12.8	0.18	0.11	0.37	5.8	0.01	2.5	0.05	0.00	2.4
1400-1439	73.0	13.8	0.20	0.10	0.42	6.6	0.01	2.2	0.05	0.00	1.9
1439-1449	53.9	17.0	1.50	0.48	0.15	3.5	0.05	10.1	0.05	0.00	7.2
1449-1500	75.0	12.0	0.22	0.09	0.20	4.0	0.02	4.5	0.05	0.05	3.2
1500-1573	76.1	12.1	0.21	0.05	0.26	4.9	0.01	2.9	0.05	0.10	1.9
1573-1621	72.9	12.1	0.30	0.04	0.22	4.8	0.01	2.5	1.20	0.20	4.0
1621-1660	75.1	12.1	0.38	0.06	0.32	5.5	0.01	2.5	0.65	0.00	2.6
1660-1683	75.6	12.5	0.22	0.05	0.28	5.3	0.01	3.1	0.00	0.20	1.6
1683-1694	74.0	12.9	0.26	0.05	0.18	4.5	0.01	3.7	0.25	0.20	2.5
1694-1754	75.4	12.0	0.16	0.06	0.32	5.4	0.01	2.1	0.55	0.00	2.3
1754-1794	78.0	12.0	0.23	0.05	0.20	4.2	0.01	2.3	0.05	0.00	1.9
1794-1851	75.5	12.5	0.15	0.05	0.32	5.5	0.01	2.1	0.05	0.00	1.4

Water Resistivity and Chemistry

It is useful to know the water resistivity when examining the response of the electrical resistivity logs. Analysis of water samples reported by Errol L. Montgomery & Associates, Inc. from the T-holes gave values as follows: 5.99 ohm-m at 25°C from T-1, 8.06 ohm-m at 32.3°C from T-2, 4.92 ohm-m at 29.5°C from T-3, and 4.96 ohm-m at 31.0°C from T-4. The value from T-1 is the average of four samples, other values are each from one sample. After temperature correction to 25°C, these values are 5.99, 9.32, 5.40 and 5.60 ohm-m, respectively, with an average of 6.58 ohm-m. At total depth in hole C-1, the measured temperature was 37.2°C (99°F). Converting the average resistivity to an effective resistivity at 37.2°C gives 5.21 ohm-m.

Sulfate is the dominant anion in the groundwater, averaging 362 mg/l for four samples obtained from T-1. Chloride averages 246 mg/l, and bicarbonate averages 86 mg/l. Of the cations, sodium averages 261 mg/l, calcium averages 64 mg/l, and potassium averages 40 mg/l. Total dissolved solids average 1126 mg/l in hole T-1.

Drilling Methods

Rotary drills with mud were used to drill the T-holes below the water table. In general, bentonite-based mud with soda ash was used above the 1200-foot level and polymer-based mud was used below 1200 feet. Mud weight during drilling ranged from 8.1 to 8.9 pounds per gallon. During reaming, mud density was increased to 8.7 to 9.4 pounds per gallon to facilitate cleanout.

Logs from cored hole C-1

Geophysical logs were obtained in cored hole C-1 by the U. S. Geological Survey during January 13-15, 1989. All USGS logging tools have diameters of 2.25 inches or less; specifications are given by Nelson (1988). At the time of logging, the hole was cased from surface to 626.9 feet. Bit sizes were 3.685 inches from 630 to 1715 feet and 2.98 inches from 1715 to 2050 feet. Although total depth was 2050 feet, logs were obtained only to a depth of about 1975 feet where a blockage was encountered. Log values were nulled above 630 feet where casing existed and from 1689 to 1711 feet where a core barrel had been left in the hole and subsequently drilled out permitting passage of the logging tools.

Logs were run singly in the following order: temperature and fluid resistivity, caliper, resistivity, induced polarization, magnetic susceptibility, density, gamma-ray and neutron, borehole deviation, and sonic velocity. Temperature and fluid resistivity were obtained on a down run; all other logs were up runs. Total logging time was 32.5 hours.

During logging of C-1, the magnetic susceptibility tool failed to maintain a constant oven temperature, resulting in severe drift. The drift was removed by eye, and the susceptibility values were left unscaled. The peaks are quite valid, but trends could have been removed erroneously. For example, the susceptibility from 630 to 750 feet may be greater than shown (figure 4).

The four resistivity traces have been corrected for borehole effect using a sequence of trial values of Rw, the borehole fluid resistivity. For each trial Rw, the algorithm recomputes the apparent resistivity for each trace, producing a set of four traces which approximate the true formation resistivity. A value of 6 ohm-meters produced the optimum overlay of the four traces. This value is not much different from the adjusted average value of 5.2 ohm-m cited in the preceding section "Water Resistivity and Chemistry".

The induced polarization (IP) and spontaneous polarization (SP) were run with a downhole reference electrode instead of a surface electrode. As a consequence, the SP trace shows the SP gradient rather than total SP.

A five-point (2.5-foot) running average filter has been applied to smooth the density log. A seven-point filter was applied to the temperature gradient log, which was derived from the temperature log by taking a 5-foot difference. No other logs were filtered.

Plotting of core data against log data showed a five-foot discrepancy in depth. To match the two data sets, all core data from C-1 were shifted up 5 feet, that is, 5 feet were subtracted from core depths.

Logs from five T-holes

Logs were acquired by Schlumberger in the five T-holes. The "openhole" logs were acquired during July through November 1989 before casing was installed; after casing was installed the geochemical tool (GLT) was run in all five T-holes during February 1990. In addition, spinner logs were run both before and after casing was installed. A few logs were also run by Schlumberger above 1200 feet but these are not examined here. Table 6 gives the dates and depths of the openhole and geochemical logs. Note that all but a few logs (Dual Laterolog, Array Sonic, Compensated Sonic) were run in all five holes.

Table 6. Depth range (feet) and date of logs obtained by Schlumberger Well Services in boreholes T-1 through T-5. The mnemonics for the primary traces are listed below the name of log. If several runs were made, only the last run is listed. Runs that do not span the 1200-1800 foot depth range are not listed.

Name of Log	T-1	T-2	T-3	T-4	T-5
Comp. Neut.-Lithodensity	1215-1867	1202-1866	1204-1870	1200-1915	1200-1872
cali, sgr, pef, rhob, nphi	08/04/89	08/24/89	07/13/89	11/01/89	11/18/89
Dual Induction-SFL	1215-1864	1202-1863	1204-1867	1200-1912	1200-1869
gr, sp, sfl, ild, ilm	08/04/89	08/23/89	07/12/89	11/01/89	11/18/89
Dual Laterolog-Micro-SFL	1215-1855			1200-1901	1200-1860
cali, gr, sp, lls, lld	08/04/89			11/02/89	11/19/89
Borehole Comp. Sonic				1200-1905	1200-1863
gr, cali, dt				11/01/89	11/18/89
Array Sonic Tool	1215-1855	~1200-TD	1204-1873	1200-1910	~1200-TD
sdt	08/04/89	na	07/14/89	11/01/89	na
Gamma-Ray Spectrometry	1215-1835	1202-1834	1204-1838	1200-1878	1200-1835
cgr, sgr, uran, pota, thor	08/04/89	08/24/89	07/13/89	11/01/89	11/18/89
Temperature	0 - 1825	0 - 1747		0 - 1903	0 - 1861
sgr, mtem, dtem	08/04/89	08/21/89		11/01/89	11/18/89
X-Y Caliper	1215-1870	1202-1760	1204-1790	1200-1916	1200-1875
gr, c1, c2	08/04/89	08/21/89	07/09/89	11/01/89	11/19/89
Continuous Dipmeter	1215-1870	1202-1869	1141-1799	1200-1916	1200-1875
gr, c1, c2, pads 1,2,3,4	08/04/89	08/24/89	unknown	11/01/89	11/19/89
Thermal Decay Time	650-1821	650-1812	650-1829	650-1894	650-1869
gr, tscn, tscf, sigm	12/21/89	12/08/89	11/18/89	12/21/89	11/19/89
Geochemical (GLT) Open hole					1200-1828
					11/18/89
Geochemical (GLT) Cased hole	1210-1826		1200-1824	1186-1929	1190-1840
	02/16/90		02/16/90	02/16/90	02/16/90

Television Log of Fractures in Hole T-1

A video camera was run in hole T-1 before the hole was cased. The service was provided by Strata-vision, a division of Nowsco Well Service Ltd, using their C250SS color side scan camera. L. Dahl of the U.S. Bureau of Mines analyzed the video tapes and picked the dip azimuth of fractures occurring between 1274 and 1807 feet. Dip magnitude could not be ascertained. In some intervals, lack of water clarity prevented a good view of the borewall. In other intervals, the borewall was covered with mud. In particular, the depth interval 1500 to 1620 feet was mostly mudcaked, preventing observation of fractures.

Diverter Flowmeter in Hole T-2

During August, 1989, a diverter flowmeter was run in holes T-1 and T-2. Test results from T-1 were erratic and are not used here. Results from T-2 were considered usable and are included. The diverter flowmeter utilizes an inverted "umbrella" that opens to fill the hole and funnel water past a spinner (Piers, 1989). The tool is operated through a lubricator while the hole is under injection from the surface. Calibration is carried out in casing where the flow is known. The tool is set at different depths in the hole, the spin rate measured, and the injection rate recorded. The fractional flow into an interval is computed by taking differences between adjacent stations. For hole T-2, the footage intervals and fractional flow data are: 1202-1276, 0.13; 1276-1289, 0.06; 1289-1339, 0.04; 1339-1405, 0.09; 1405-1416, 0.18; 1416-1428, 0.20; 1428-1473, 0.12; 1473-1524, 0.18; 1524-1760 (TD), 0.00.

Casing and Perforations

From 1200 feet to total depth, the five T-holes were drilled with a 9 7/8-inch diameter bit and cased with 7-inch (nominal) o.d. fiberglass (FRP) casing. The casing has a nominal i.d. of six inches and a wall thickness of one inch. The casing was cemented in place using a mix specified in Table 7.

Table 7. Material used to cement fiberglass casing to rock. Material used to cement fiberglass to steel casing above 1200 feet is not given here.

Material & Amount	T-1	T-2	T-3	T-4	T-5
Water (gal)	8400	4200	4494	2100	2100
Superflush (gal)	420	420	-	420	420
Water (gal)	420	420	-	420	420
Tail Slurry Depth (ft)	1172-1820	1052-1870	842-1870	950-1870	?-?
Tail Slurry (gal)	2100	2520	2759	2625	2575
a. type II cement (lb)	15390	19270	21150	17860	19728
b. bentonite (lb)	770	964	1058	893	986
c. gilsonite (lb)	-	-	-	1900	-
d. water (gal)	1445	1745	2638	1682	1860
Water (gal)	2814	2772	2638	2831	2755

Chemical analysis of Type I/II Portland Cement is as follows: silicon dioxide 21.97%, aluminum oxide 3.69%, ferric oxide 2.66%, calcium oxide 63.34%, magnesium oxide 4.15%, sulphur trioxide 2.50%, loss on ignition 1.23%, insoluble residue 0.53%, and alkalies 0.47%. The analysis was performed by the Arizona Portland Cement Company.

Perforations were shot at one-foot intervals in all T-holes. In holes T-1, T-3, T-4, and T-5, each shot was placed at a 90 degree angle from the one above, forming a spiral geometry. In hole T-2, each sequence of shots was co-planar, with the next sequence oriented at some uncontrolled angle with respect to its neighbor.

Perforation intervals are at very similar depths in all T-holes except T-3 (Table 8). Due to a depth reference error, the perforations in T-3 are about 23 feet deeper than designed.

Table 8. Perforated intervals (ft) and shots/interval.

T-1	T-2	T-3	T-4	T-5
1570-1620 50	1570-1617 48	1593-1643 50	1570-1620 50	1570-1620 50
1620-1656 36	1622-1666 45	1648-1696 45	1625-1670 45	1625-1670 45
1656-1694 38	1672-1716 45	1701-1746 45	1675-1720 45	1675-1720 45
1694-1732 38	1722-1770 49	1751-1796 45	1725-1770 45	1725-1770 45
1732-1770 38				

The perforations were acidized and fractured to increase permeability. Acidization was performed with straddle packers isolating a four-foot injection zone. The surface breakdown pressures applied to each four-foot interval were entered as curves to see if the pressures would correlate with any logs that reflect permeability variations.

After perforation, acidization, and acid recovery, a video camera was run in each of the five T-holes (Melzer, 1990). The depths of observable casing collars and perforations were recorded. Not all perforations could be seen due to murky fluid in the wellbore, so this record does not appear to be useful for showing perforations. Instead we rely on the depth intervals over which perforations were shot. However, the camera did reliably locate the casing collars. Blips on the casing collar locator log run on Schlumberger production tools are not casing collars, but are caused by metallic centralizers that are not located at the collars.

Full-bore spinner flow logs in five T-holes

Schlumberger ran its full-bore spinner tool to record flow profiles in holes T-1 through T-5 during the time period June 13-16, 1990. The flow logs were run in cased hole while water was being injected from surface. Eight passes were made in each hole: an up-run and a down-run at four different pull rates (figure 2). The up-run and down-run separate at or near the bottom of the perforated interval in all five wells, indicating that flow is exiting the wellbore. Examples of logs obtained at the highest pull rate are shown in figure 3, one for each well.

Schlumberger's analysis of the spinner logs followed a format suited to completion of a petroleum production well where non-perforated intervals are interspersed with perforated intervals. After conversation with P. Scholes of Schlumberger, we determined that their analysis was not suitable for the continuously perforated intervals in the T-holes, and we reanalyzed the flow logs. Taking the log obtained at the highest pull rate, we divided the flow log into intervals where variations in rate could be seen and then simply apportioned the spread between the up and down runs over those intervals. Some intervals selected for T-4 are shown in figure 2; results for all five holes are given in Table 9. For example, in well T-1, 12.3% of total flow exits the well between 1580 and 1600 feet. Typical injection rates during the time the flow logs were run are given in figure 3. The rates are approximate and were taken from data supplied by SAIC. Because injection rates into wells T-1 and T-5 were considerably less than into the other three wells, the spin rate of the tool is reduced, and the reliability of the percentage flow estimates are therefore lower.

Table 9. Percent flow from fullbore spinner during injection tests. Depth columns give top of depth range (feet).

T-1		T-2		T-3		T-4		T-5	
Depth	%	Depth	%	Depth	%	Depth	%	Depth	%
1500	0.0	1500	0.0	1500	0.0	1500	0.0	1500	0.0
1569	4.4	1568	17.4	1590	27.1	1569	15.5	1568	17.9
1580	12.3	1576	7.8	1615	8.6	1575	4.4	1600	2.9
1600	5.3	1589	5.5	1628	1.4	1605	8.9	1635	25.7
1610	0.0	1600	5.8	1670	0.0	1636	11.1	1726	11.4
1647	9.6	1647	5.5	1783	62.9	1654	17.8	1736	42.1
1659	2.6	1764	58.0	1794	0.0	1670	4.4	1772	0.0
1670	0.0	1773	0.0	1800	-	1675	0.0	1800	-
1715	0.0	1800	-			1755	37.8		
1733	9.6					1773	0.0		
1746	34.2					1800	-		
1758	21.9								
1770	0.0								
1800	-								

LOGS FROM CORED HOLE C-1

Logs and core data from hole C-1 that pertain most to the effects of alteration and porosity are displayed in figure 4. Logs most relevant to mechanical and flow properties are shown in figure 5, and logs pertaining to mineralogy are shown in figure 6. Logs displayed in these figures extend from 600 to 2000 feet, a depth range greater than that logged in the T-holes. A directional survey (not shown) found that hole inclination is generally one degree or less; measured footages along hole are within 0.2 feet of true vertical depth and radial displacement of bottom is 19.8 feet from the top. Most of the features displayed in these figures will be discussed in the Section "Geological Features"; here we make a few introductory remarks.

The caliper log (fig. 4) shows that borehole rugosity is minimal, producing no adverse effect on the logs. Diametral openings do not exceed 0.5 inches except at the bottom of casing.

The general high level of gamma-ray activity (fig. 4) is attributed to potassium and thorium in feldspars and clays (the Schlumberger natural gamma spectrometry logs in the T-holes show that uranium generally contributes much less to the total gamma response than potassium and thorium). Potassium and thorium depletion occurs at two locations within the leached cap, at 775 to 820 feet and at 935 to 980 feet. Both zones also have anomalously low values of resistivity.

The neutron and resistivity logs (figs. 4 and 6) track one another fairly closely, especially in the oxidized zone below the leached cap. The sonic log (fig. 5) also tracks the neutron and resistivity fairly well. Because they track so well, it can be assumed that porosity is the primary control on these three logs, although clay content is an important factor. Because of clay content, it is not straightforward to compute porosity from any of these three logs. The neutron response is shown on a "porosity" scale, but the recorded values are much higher than true porosity because water in the clay and sericite also thermalizes neutrons and contributes to the neutron porosity. Resistivity is also greatly affected by clay content; direct application of Archies law without considering the clay contribution yields a porosity estimate which is much too high. Good porosity estimates can only be obtained if the clay content is taken into account.

The temperature increase (fig. 5) at 630 feet occurs at the bottom of casing and is attributed to the casing. The temperature log reveals three other cooling anomalies that are attributed to the injection of drilling fluid into the formation. These zones are located at 855-885, 1025-1060, and 1950-1985 feet. The differential SP curve, which sometimes responds to flow, is anomalous at the upper and lower of the three. The strength log and sonic travel time also indicate a higher degree of fracturing in the upper and lower three zones. The caliper shows minor borehole roughness at all three intervals. It is likely that these three zones are exceptionally fractured and permeable.

OPEN HOLE LOGS FROM T-HOLES

The openhole logs are presented in two formats: well by well and log by log. The well-by-well format (figures 7-11) displays the most important Schlumberger logs for each well. We use these figures to introduce the logs; the columns in the figures are referred to as "tracks". Nomenclature is given in a table preceding figures 7-11. The geological features that can be discerned in the logs are discussed under the subsequent section "Geological Features".

The caliper log, in track 1, shows the diameter of the hole. For comparison the bit diameter of 9.875 inches is shown as a straight dashed line. It is often useful to check a log against the caliper to see if it might be influenced by rough hole. From figures 7-11 we see that the biggest "washouts" occur at 1200 feet, immediately below the bottom of steel casing. Below that, typical borehole enlargements are usually 2 to 3 inches. All holes are somewhat rugose above 1400 feet. Below that depth, there is no particular pattern to the rugosity.

The temperature logs, also in track 1, display a very uniform and linear temperature increase with depth. There are no fluctuations that would reflect the loss of drilling fluid into the rock. Without a record of the time elapsed since drilling fluid was last circulated before logging, we cannot comment on the absence of temperature anomalies.

The gamma-ray log, in track 1, is the sum of the contributions from the uranium, potassium and thorium curves shown in tracks 2 and 3. Note that in some places the gamma-ray curve reflects the character of the uranium curve; where uranium content is low, the gamma-ray reflects the character of the potassium and thorium curves. Potassium and thorium track each other quite closely.

Electrical resistivity and self potential (SP) are shown in track 4. Where the laterolog was available, the msfl, lls, and lld are shown (figures 7, 10, and 11); otherwise the sfl, ilm and ild from the induction tool are shown. It is clear from the figures that the msfl has much higher resolution than the sfl. Resistivity decreases where sulfides are present as in the interval 1500-1600 feet in hole T-1 (figure 7). Resistivity also decreases where porosity increases, as at 1630 feet in hole T-2 (figure 8). In particular, porosity increases and resistivity decreases in the diabase sill located near 1450 feet in holes T-1 and T-2. The SP curve responds to sulfide mineralization (1500-1600 feet in T-1, 1550 feet in T-5) but otherwise does not appear to be a very useful curve.

Sonic travel times of three wave modes are shown in track 5. Travel time is equivalent to the reciprocal of velocity and as it increases to the left, porosity and fracturing increase. The scales were selected such that the shear and compressional curves overlie one another wherever the ratio of compressional to shear velocity is 1.8. The Stonely wave arrives later than the shear.

Porosity derived from the neutron log (track 6) is plotted increasing to the left so it will deflect in the same direction as the electrical resistivity and sonic curves. The neutron porosity reads a higher value than true porosity because bound water in clays contributes to its response. Both thermal neutron and epithermal neutron curves are shown in figures 7-11. The thermal neutron (CNL) logs were acquired in open hole with the density (LDT) log; the epithermal neutron (CNT-G) logs were acquired with the geochemical (GLT) log in cased hole. In wells T-1 and T-3 the epithermal log was improperly calculated and hence the enphi scale is unrealistically high. In wells T-4 and T-5 the enphi scales have been adjusted to produce overlap; however the enphi values exceed the nphi results by 2 to 6 volume percent. This excess is attributed to the contribution of casing and cement.

Bulk density, shown in track 7, deflects to the left wherever porosity increases. In many rocks, the density log tracks the neutron porosity curve quite well, but here it has a very noisy character due to the presence of several elements of high atomic weight, such as iron and copper. The heavier elements are also detected by the photoelectric effect (Pe) curve and the thermal absorption (sigma) curve. An obvious example occurs between 1700 and 1750 feet in hole T-3 (figure 9).

GEOLOGICAL FEATURES

In this section we illustrate and discuss geological and mineralogical features that can be discerned in the logs. Some of the figures, such as figure 12, display just one or two variables for all five wells. In these figures, the five-spot geometry is arrayed in the shape of a capital "N", with the southwest well T-4 at the left, and the northeast well T-1 at the right. The inner three wells on the plot, T-2, T-3, and T-5, comprise a cross-section with the view to the northeast, while the outer two, T-4 and T-1, together with the central hole T-3, comprise a cross-section with the view to the northwest. Keep in mind that the two eastern wells T-1 and T-5 appearing on the right side of the plots have very little copper whereas the three wells T-4, T-2, and T-3 appearing on the left contain appreciable copper oxide mineralization.

Diabase.

The physical properties of diabase are sufficiently different from granite that several logs can be used to distinguish and locate diabase. In cored hole C-1 (figure 4), diabase causes the spikelike increases on the magnetic susceptibility from 1850 to 1980 feet, as confirmed by visual comparison of the logs with core. The corresponding spikes on the neutron log are attributed to thermal neutron absorption by mafic minerals in the diabase; this is confirmed by the relatively high concentrations of iron and magnesium determined by chemical analysis in cored hole C-2 (figure 18). Increases in sonic transit time and decreases in resistivity indicate that the diabase is more altered and probably has higher porosity than the host granite. That more clay minerals are present in the diabase than in the granite is substantiated by the increase in loss-on-ignition shown in figure 18. Where the diabase intercepts are thick, as at 1422 to 1438 feet, the gamma-ray activity is reduced. The magnetic susceptibility and thermal neutron logs appear to be the most reliable discriminators of diabase.

Diabase Sill.

A near-horizontal diabase sill varying in thickness from 3 to 16 feet can be discerned in four of the T-holes. In three of the T-holes. the intercept is unambiguous with the same characteristics as seen in cored hole C-1: gamma-ray and resistivity decrease while neutron porosity increases. The depth intervals are 1446-1456 in T-1, 1436-1451 in T-2 and 1410-1426 in T-4. In T-5 the diabase is much thinner, occuring at 1416-1419 feet, and the pick is less certain; "diabase dikelets" were diagnosed from the cuttings.

The characteristic diabase signature is not present in the central hole T-3. Instead, over the interval 1414-1434, the gamma-ray log is high instead of low and resistivity does not change much. Neutron porosity is high. Observation of cuttings at this depth in T-5 indicated high iron oxide content and very little diabase. Better information comes from cored hole C-2 which lies within 30 feet of T-3 at this depth. The geological description for C-2 notes that diabase and diabase breccia are present from 1439 to 1449 feet within a fault zone extending from 1420 to 1472 feet, described as "strongly broken and crushed with local soft and hard gouge". Faulting within the region penetrated by T-3 and C-2 has altered the physical properties of the diabase. However, on the basis of the neutron response, we believe the diabase is present at a depth of 1414-1434 in T-3.

Uranium distribution.

The Schlumberger natural gamma spectrometry log provides abundances of potassium, uranium, and thorium. Shown in figure 12 are uranium logs in five T-holes and the location of the diabase sill. Above the sill and within a zone more or less coincident with the upper copper oxide zone, uranium content is around 10 ppm. Note that the diabase sill coincides with the lower boundary of the upper zone where uranium content is higher than below the sill. Arithmetic means are tabulated in table 10 for three zones in each hole. Uranium content is around 2 to 4 ppm below the sill and 5 to 8 ppm near the bottom of the holes. Because of the magnitude of environmental corrections for the NGT tool, the uncertainty in uranium concentration may be several ppm. Nevertheless, table 10 and figure 12 provide valid comparisons of the uranium distribution with depth.

Table 10. Uranium content (ppm) averaged from spectral gamma-ray logs over three depth zones (feet) in each hole.

T-1	T-2	T-3	T-4	T-5
1268-1464 10.7	1255-1455 13.0	1245-1438 9.4	1220-1426 8.5	1250-1435 14.9

Table 10. Uranium content (ppm) averaged from spectral gamma-ray logs over three depth zones (feet) in each hole.

1464-1730 3.4	1455-1706 2.6	1438-1708 2.4	1426-1668 3.5	1435-1700 4.2
1730-1870 5.8	1706-1820 5.7	1708-1872 8.0	1668-1796 5.7	1700-1830 6.0

Figure 13 show the concentrations of potassium, uranium, and thorium as derived from the NGT tool in hole T-2. In the left track are shown the total gamma radiation and the gamma radiation due to potassium and thorium with uranium excluded. The difference between the two is solid black. Even in the upper zone where uranium concentration is greatest, the contribution to the total gamma spectra by daughter products of uranium is much less than that from potassium and thorium.

Uranium concentration in silicic igneous rocks is generally within the range 1 to 10 ppm (Clark et al., 1966). Based on a large number of samples from sites throughout the world, Clark et al. (1966) report a mean value of 4.7 ppm and a median of 3.9 ppm. Uranium can be highly mobile in oxidizing environments; its anomalous presence in fractured rock is sometimes used to infer transport and deposition by circulating groundwaters (Fertl et al. 1980, West and Laughlin, 1976). Given the excellent correlation of uranium distribution with the diabase sill (figure 12) and with the copper oxide distribution (figure 23), it is quite likely that the pattern of uranium distribution in the T-holes is the result of dissolution and precipitation rather than primary distribution.

Sulfide Distribution.

Because they are electrically conductive, sulphide minerals are easily discerned on induced polarization, SP, and resistivity logs. In cored hole C-1, the induced polarization (IP) and SP logs (fig. 6) show that sulfide minerals occur at only four depths in the hole. The four excursions in IP and SP are confirmed by the observed presence of chalcocite in core (column 1 of fig. 6). Two of these appear to be in diabase and two are in granite. By way of contrast, the non-conducting oxide minerals atacamite and chrysocolla indicated in the first column of fig. 6 tend to occur within high resistivity intervals.

Small amounts of sulphide minerals are present in all five T-holes, and are especially abundant in T-1, as can be seen by comparing the resistivity logs in figures 7 through 11 or by viewing the composite figure 14. Resistivity logs over two sulphide-bearing intervals in T-1 are shown in figure 15. Note that all six resistivity curves produce a similar response across the diabase sill at 1450 feet. By comparing the details of the response to the diabase sill, it can be seen that the msfl has the greatest spatial resolution, as expected because it is a pad tool, and that the deep induction tool has the poorest resolution.

Quite different results are obtained across the two sulphide zones centered at 1495 and 1575 feet (figure 15). Here the two induction logs, ilm and ild, produce unrealistic data: the logs are often off-scale and show increases in resistivity in places where the other four logs do not. The induction tools are particularly susceptible to distortion in the presence of thin, highly conductive veins, which is probably the mode of occurrence here. Such distortion is inherent in the induction measurement, but, in cases of extreme resistivity contrast, is worsened by numerical filtering called deconvolution that is applied to the induction logs (Shen, 1989, fig. 7). The laterolog tool (msfl, lls, and lld) gives more realistic results where sulphide veins are present. Given the distortion of the induction in the presence of sulfide veins, and given the good agreement between laterolog and induction tools elsewhere, we see no reason to use the induction tools in further work at Santa Cruz. The laterolog tool does a superior job.

Fractures and Sonic Logs

The sonic slowness log overlies the mechanical strength log in cored hole C-1 (figure 5) with remarkable fidelity, particularly when we recall that the strength log is derived from observations on core whereas the sonic log is a continuous record of sonic speed at fairly high (20 kHz) frequency. The overlap is good even in the slow, low-strength rock above 1000 feet where the rock quality designation (RQD) (column 2 of fig. 5) records only a zero value because the core is so badly broken. The agreement between the strength log and the sonic log indicates a close tie between fracturing, porosity, and alteration. Viewing these two logs in conjunction with the neutron and resistivity, one gains the impression that the rock is pervasively fractured and that both alteration and porosity increase where the microfracturing is most pervasive.

Figure 16 shows the compressional and shear travel time logs in the five T-holes, scaled such that the two logs overlay one another wherever the shear to compressional travel time ratio is 1.8. As we have seen in hole C-1, where travel time increases, fracturing and alteration also increase. A zone of increased fracturing occurs in all holes except T-1 at a depth of 1400 to 1500 feet, an interval that includes the diabase sill discussed earlier. Other excursions in compressional and shear travel time are apparent. The character of the sonic logs below 1500 feet will be discussed in more detail under the "flow" section.

Although one would expect borehole "breakouts" to increase in fractured zones, the caliper logs (figures 7-11) show no consistent correlation with the sonic logs. Breakouts do occur in the fractured interval from 1400-1500 feet in holes T-4 and T-2 (figures 10 and 8), but the borewall is remarkably smooth in hole T-3 (figure 9). Nor is there any consistency from well to well regarding the depth where breakouts occur.

A reminder of the relationship between alteration, expressed by the total gamma-ray log, and sonic travel time is shown in figure 17. Correspondence between the two logs is generally quite good, except within the 1400-1500 foot interval where rock is believed to be highly fractured. The diminution of gamma-ray activity is attributed to reduced potassium and thorium content where potassium feldspars have been altered to kaolinite and sericite.

ELEMENTS AND MINERALOGY

Background

We now turn to the logging measurements which are either element-specific or else measure a macroscopic parameter that is dominated by a few elements. These logs are listed in table 11. Because these measurements will not be familiar to many readers, they are briefly described in the following paragraphs. General descriptions can be found in Ellis (1987) and Hearst and Nelson (1985).

Table 11. Nuclear and photoelectric measurements responding to specific elements used in 10-inch T-holes.

Measurement	Name	Elements
Natural Gamma Spect.	NGT	K, U, Th
Aluminum Activation	AACT	Al
Neutron Activation	GST	Cl, Ca, S, Si, Fe, Ti, Gd
Photoelectric Absorption	LDT	high atomic no.
Thermal Neutron Absorption	TDT	high cross-section {B, Cl, Cu, Fe, K ...}

Natural Gamma-ray Spectrometry

Three elements have a naturally occurring radioactive isotope in sufficient abundance that the gamma-rays are measurable with logging instruments. These are uranium, potassium, and thorium. The logging instrument requires no source, and uses a NaI crystal for detection, with energy windows set appropriately to detect the dominant gamma-rays of the three elements.

Neutron Activation

High-energy neutrons emitted from a neutron source into rock are quickly reduced to very low (thermal) energies by collisions with nuclei, chiefly hydrogen. At thermal energies, neutrons are readily captured. Following the capture of a thermal neutron, some elements immediately emit gamma-rays at one or more characteristic energies. Chlorine is one of these elements. Others are Ca, Si, S, Fe, Ti, and Gd. The resulting "prompt capture" gamma spectrum, consisting of contributions from each of these elements, is fitted with laboratory spectra for each element to determine the elemental yield, or contribution to the total spectrum. Elemental yields can be converted to weight percent, using a depth-varying calibration factor (Hertzog et al., 1989). An example of chlorine yield is plotted in figure 24.

Aluminum is determined with a separate tool that utilizes a different mode of capture, called delayed activation. In this mode, the activated element decays with a characteristic half-life, emitting gamma-rays of specific energy. Logging speed must be controlled to maximize the return energy in accordance with the half-life. Examples of aluminum logs are shown in figures 20 and 21.

Photoelectric Absorption ("Pe")

The high energy portion of the gamma-ray spectrum, where Compton scattering is the dominant mechanism, is used to measure rock density. Photoelectric absorption dominates the low-energy portion of the spectrum and is proportional to atomic number raised to a power. Thus the "Pe" response is especially sensitive to heavy elements. Figure 19 shows that copper and iron have exceptionally high Pe values relative to other elements present in the Santa Cruz deposit. Calcium and chlorine are other minor elements with substantial Pe values. Potassium is the only major element with a Pe value greater than 10. In oil exploration, the Pe log is used to distinguish lithology. In our application, it indicates the presence of diabase, iron oxides, and copper minerals.

Thermal Neutron Decay ("Sigma")

The rate of decay of thermalized neutrons following a burst from a 14-Mev neutron source is determined by the neutron capture cross-section "sigma". The capture cross-section of the rock is dominated by a few elements of singularly high cross-section or abundance. Table 12 shows that Cl has a high capture cross-section. Because of its abundance and relatively high sigma, potassium can be expected to contribute substantially to the total observed sigma. Other elements with high sigma include Gd, B, H, Mn, Ti, Cu and Fe.

Table 12. Thermal absorption cross section "sigma" of elements, normalized by mass (cm^2/gm). After Ellis, 1987.

Gd	188	Fe	0.0275
B	42.3	Na	0.0139
Cl	0.564	S	0.00977
Ag	0.355	Ca	0.00646
H	0.198	Al	0.00513

Mn	0.146	P	0.0035
Ti	0.0767	Si	0.0034
W	0.0606	Mg	0.00156
Ni	0.0454	C	0.00017
Cu	0.0365	O	0.0000102
K	0.0323		

Results

The geochemical tool, comprised of the NGT, AACT, and GST, was run in T-5 open hole (uncased) and in T-1, T-3, T-4, and T-5 cased hole (table 6). Neither situation was ideal. The open hole was logged without the boron sleeve customarily used to moderate neutrons. As a consequence, the spectral stripping could not be done with Schlumberger's commercial software and was sent to Schlumberger-Ridgefield for processing with research software. The cased holes presented a different problem because GLTs are usually run in open holes, so that no compensation is required for casing materials. Fiberglass contains boron, an element with high neutron cross-section. The cement annulus has a high calcium content. The existence of these and other elements in cement and casing creates uncertainties in the elemental analysis.

Elemental analysis from the open-hole run in T-5 is shown in figure 20. The order of presentation matches that of figure 18, so the elements determined by logs can be compared with chemical analysis. Because chlorine is given as yield in figure 20, it cannot be compared with weight percent values, leaving five elements (Al, Si, Ca, K, and Fe) to compare. Aluminum, at about 8% in both holes, compares quite well. But the silicon values from fig. 20 are somewhat lower than the chemical values. Moreover, the silicon values are very erratic and the sharp decreases are correlated with increases in calcium. Calcium from the geochemical log is much higher than from chemistry (note the change in scale for Ca between figs. 20 and 18). Clearly, the calcium estimates are erroneously high and have contaminated the silicon estimates. The iron estimate also appears to be too high. Especially worrisome is the high estimate of potassium (average of 6.4% from 1200 to 1840 feet in fig. 20) from the NGT log, compared with values of about 4 weight percent from chemistry. It appears that the results from the open-hole run in T-5 require re-analysis.

Similar problems were encountered with the geochemical logs run in cased hole. In particular, calcium values were much too high, and were attributed to cement. As a test, calcium was set to zero and the elements recomputed (figure 21). As a consequence, the spikelike decreases have disappeared from the silica trace. Potassium is somewhat higher than in the open hole (averaging 6.9% over 1200 to 1840 feet), presumably due to incorrect compensation for attenuation by casing and cement. And the chlorine yield appears to be more reasonable. Although the yields should be recomputed using redistribution coefficients rather than by setting calcium to zero (J. Schweitzer, p.c.), the results of figure 21 are reasonable enough that a trial mineralogical computation can also be presented.

Transforming the elemental data to mineralogical estimates requires that the mineral suite and mineral chemistry be specified, as in table 4. The transform was computed on Schlumberger software using methodology described by Herron et al. Results are shown in figure 22, with mineralogy and porosity shown as volume percent. Note that quartz and orthoclase each typically comprise about 40% of whole rock, values that appear to be reasonable when compared with the modal mineralogy cited in table 3. On the other hand, the kaolinite estimate may be too high and the sericite estimate too low. Chrysocolla estimates are too high. Porosity values, which were computed with the minerals, are about the same magnitude as core values. Overall, the results are encouraging, keeping in mind the uncertainties of the elemental inputs.

Copper Estimates

The copper assays are summarized in figure 23. The assay values have been apportioned among atacamite, chrysocolla, and copper-in-plagioclase based upon visual observation. Note that atacamite dominates in the lower ore zone, that copper content is less in the upper than in the lower ore zone, and that atacamite and chrysocolla appear to be equally abundant in the upper ore zone.

Copper was not directly detected by any of the logging tools. However, the most important copper mineral at Santa Cruz is atacamite which contains chlorine, and chlorine can be detected by several nuclear logging tools. These tools employ neutron capture, thermal neutron decay, and photoelectric absorption; examples of their response is plotted in figure 24, along with the atacamite distribution. Because three tools respond in part to chlorine, atacamite is well determined as long as no other chloride-bearing mineral is present. In this case, because chrysocolla is associated with atacamite, and because we are interested in total copper, we use total copper as the dependent variable to be predicted rather than atacamite. Multiple regression is used to establish a predictor of copper based upon well logs.

To establish a data set for regression, the copper assays were shifted upward three to five feet, depending on the well, so that copper peaks were aligned with peaks in the logs attributed to copper mineralization. Next, because copper values are given in ten-foot composites rather than as logs, the logs were averaged over ten-foot intervals. Averaging produced a data set of 126 samples from wells T-3 and T-4 combined. Wells T-1 and T-5, having low copper content, were held out to test the regression result. Because neutron capture and thermal neutron decay logs were not acquired in well T-2, data from T-2 were not included in this statistical exercise.

The six logs used for regression tests are listed in table 13, along with means and standard deviations. Four of these six logs turned out to be significant; they are shown in figures 25-28, along with the averaged values.

Table 13. Means and standard deviations of copper and six variables in wells T-3 and T-4, over the interval 1200 feet to total depth. Chlorine "yield" was used instead of weight percent.

Variable	Symbol	Units	Mean	Stddev
Copper	cu	wgt percent	0.57	0.80
Chlorine	cchl	percent yield	0.033	0.064
Potassium	pota	wgt percent	6.57	1.08
Neutron cross-section	sigma	capture units	17.15	2.71
Density	rhob	gm/cc	2.45	0.07
Photoelectric absorption	pef	barns/electron	2.90	0.61
Iron	wfe	wgt percent	2.73	1.18

The correlation between copper and some of the variables can be inspected in figures 25-28. Obviously chlorine and sigma are well correlated with copper. This visual comparison is substantiated by the correlation matrix of table 14, which gives correlation coefficients of 0.816 and 0.801 for chlorine and sigma. We see that the coefficient for the pef log is relatively low, 0.307, despite the good visual correlation at some depths. The low negative coefficient for potassium indicates that decreases in potassium are poorly correlated with copper increases.

Table 14. Correlation matrix of copper and six variables from well logs, based on 126 samples from T-3 and T-4.

	copper	pef	rhob	pota	cchl	wfe	sigma
copper	1.000	.307	.342	-.247	.816	.465	.801
pef	.307	1.000	-.387	-.280	.303	.328	.355
rhob	.342	-.387	1.000	.090	.390	-.062	.098
pota	-.247	-.280	.090	1.000	.046	-.422	-.121
cchl	.816	.303	.390	.046	1.000	.251	.764
wfe	.465	.328	-.062	-.422	.250	1.000	.616
sigma	.801	.355	.098	-.121	.764	.616	1.000

Establishing a correlation matrix is the first computational step in multiple regression. The next step, selection of variables, can be carried out automatically by computer software incorporating schemes called forward and backward regression. Forward regression seeks the independent variable having the highest correlation with the dependent (copper) variable. It then finds a second variable with the next highest correlation, while keeping the first variable. Backward regression begins with all variables and then sequentially removes the least important of those remaining. The results of these steps are shown in Table 15. Both the forward and backward stepwise methods selected the variables in the same order of importance. Chlorine was selected first, followed by potassium, then by sigma and so on. Note that sigma was not selected as the second variable despite its second highest correlation coefficient (table 14). This occurs because chlorine and sigma logs are highly correlated (coefficient of 0.764 in table 14) so that the sigma log does not add much new information if the chlorine log has already been used.

The R^2 coefficent listed in table 15, sometimes called the sample coefficient of determination (Walpole and Myers, 1989), represents the proportion of the variation of copper explained by the regression. Note that it increases rapidly as the second and third variable are added, then fails to increase after the fourth variable is added. Essentially the fifth and sixth logs, pef and wfe, do not further enhance the prediction of copper. We adopted the four-term regression equation,

$$cu = 5.702*cchl - 0.170*pota + 0.121*sigma + 1.554*rhob - 4.380$$

to predict the copper curves shown in figures 25-28.

The coefficients in this equation, computed for non-standardized variables in physical units, differ from those in table 15 which were computed for standardized variables. Standardized variables, having a mean of zero and a standard deviation of one, are useful because the regression coefficients can be compared one to another without regard to the magnitude and range of the variables. For prediction on the original variables, the coefficients of the above equation must be used.

Table 15. Regression coefficients, intercept (inter), and R^2 coefficent for copper with respect to six independent standardized variables.

cchl	pota	sigma	rhob	pef	wfe	inter	R^2
0.82						0.24	0.666
0.83	-.29					1.62	0.747
0.57	-.23	0.34				-0.25	0.792
0.46	-.23	0.41	0.14			-4.36	0.808
0.44	-.22	0.41	0.16	0.02		-4.87	0.808
0.46	-.22	0.39	0.15	0.02	0.02	-4.76	0.808

The predicted copper compares quite well with the measured copper assays in wells T-3 and T-4 (figures 25 and 26). Inspection of T-4 shows why potassium is an important contributor to the regression. The chlorine log does not respond to copper in the diabase at 1420 feet or to copper at 1770 to 1810 feet, but potassium decreases at both depths. Undoubtedly the regression equation would be substantially different if these two zones were excluded or if well T-3 were used alone to establish the regression.

Wells T-1 and T-5 were not used to establish the regression equation, and can be regarded as test wells, albeit poor ones because of their low copper content. Consequently, the comparison between predicted and measured copper in wells T-1 and T-5 (figures 27 and 28), is less satisfactory than in T-3 and T-4.

Suppose the neutron capture (GST) tool had not been run, could a good predictor be developed? The correlation coefficients of table 14 suggest that one could be, based primarily on the neutron absorption (TDT) tool. Excluding cchl and wfe from the regression yields,

$$cu = 0.206*sigma + 3.735*rhob - 0.112*pota + 0.199*pef - 11.97$$

with an R^2 coefficient of 0.758. Again, both forward and backward stepwise regression yielded the same ordering of the variables with sigma the most important and pef the least.

POROSITY

Porosity has been estimated in three ways: from core measurements, from linear transforms on open-hole logs, and from simultaneous solution with mineralogy. We discuss these three methods in sequence.

The most reliable measurements of porosity are usually those determined from core. The porosity measurements listed in table 2 are plotted as a function of depth in figure 29. Samples were taken from the lower ore zone of core holes C-2 and SC-19 and have average porosities of 7.5% and 7.6%. The range of values is greater in SC-19 (3% to 14%) than in C-2 (4% to 10% with one sample at 16%). Core-derived porosities can be higher than in-situ values if unloading as the core is brought to surface causes significant expansion of the pore space. On the other hand, core-derived porosities can be low if sampling tends to favor selection of more intact specimens, leaving unmeasured those zones of higher porosity. We suspect that if any bias exists, it is more likely due to sampling. If so, then the core-derived porosities are a lower bound to the in-situ values.

Porosity can also be estimated from simple linear transforms of the logs. The transforms, established from empirical correlations, work well where clay content is negligible and where mineralogy does not vary much. Figure 30 shows porosity derived from the thermal neutron, density, resistivity, and sonic travel time logs. The different estimates do not agree very well below a depth of 1700 feet, and the log-based estimates (shown on a 0-40% scale) are generally higher than the core-based measurements of Figure 29 (shown on a 0-20% scale).

The neutron log is shown as a reference in all three columns of figure 30. The presence of water and hydroxyls associated with clays boosts the neutron response. As a consequence, the neutron response indicates a porosity greater than that of the other logs.

Porosity was derived from resistivity R_o obtained from the shallow laterolog using Archies law

$$R_o/R_w = \phi_R^{-m} \qquad (1)$$

A value of 5.2 ohm-m for water resistivity R_w and m=2 were used to compute porosity, (ϕ_R), which ranges between 10 and 15%. These values are greater than true porosity due to excess conduction due mainly to clays. In addition, the high porosity spikes at 1760 and 1790 feet are attributed to sulfides.

Porosity is derived from the density log ρ_b by solving equation 2 for porosity ϕ,

$$\rho_b = (1-\phi)\rho_g + \phi\rho_f \qquad (2)$$

where the fluid density ρ_f=1.0 gm/cc and the grain density ρ_g=2.67 gm/cc, from table 2. In fact, the grain density is not constant but varies considerably with depth, as can be seen in table 2 and by the variation in Pe shown in track 2 of figure 30. Where Pe increases, the true grain density also increases, increasing the bulk density and artificially lowering the density-derived porosity. A good example occurs at a depth of 1730 feet in figure 30.

An empirical transform relating porosity to sonic velocity V_p in sandstones (Eberhart-Phillips, 1989) includes a term for fractional clay content, c:

$$V_p(\text{km/s}) = 5.67 - 6.94\phi - 1.73\sqrt{c} \qquad (3)$$

Equation 3 was solved for porosity, using $V_p = 304.8/\Delta t$ where Δt is the compressional travel time in microseconds/foot. A zero-clay assumption (c=0) produced trace ϕ_{v1} in figure 30 and an estimate of c=0.13 produced trace ϕ_{v2}. The reasonable agreement between ϕ_n and ϕ_{v1} reflects the dependence of both the neutron and velocity logs upon clay content. The lower porosity estimate of ϕ_{v2}, adjusted for clay content, is probably more realistic, but the fluctuations still reflect variations in clay content as well as porosity.

None of the logs in figure 30 are valid estimates of in-situ porosity, for reasons just cited.

A preferred method is to compute porosity simultaneously with mineralogy, thereby obtaining consistent estimates of volume percentages of both solid and fluid constituents. This computation was done by D. Johnston of Schlumberger using "Elan" software. The computation yields an "effective porosity", or volume of free water, and "bound water volume", or water associated with clays (curve fxbw in figure 22). Effective porosity is the variable of interest to us here.

Porosity values computed with Elan software are shown in figures 33-37 and 22. Generally, the values average less than 10% and track the resistivity variations, thereby giving confidence in their validity (resistivity was not used in the calculation). Over the interval 1550-1750 feet, the average porosities from the four cased-hole geochemical logs are: T-1, 6.6%; T-3, 4.4%; T-4, 6.5%; and T-5, 6.7%; average porosity from the open-hole geochemical log in T-5 is 6.0%. The porosity computations are preliminary, pending rework of the mineralogy computation. Given the problems with simple porosity transforms discussed above, and the reasonable preliminary calculations of figures 33-37, the mineralogical approach is preferred.

The recommended course of action is to refine the mineralogical estimates. Porosity can then be estimated in either of two ways. The first, a solution for porosity "as a mineral" has already been demonstrated. Second, the product of mineral volumes and mineral densities can be summed to obtain a grain density estimate. This estimate of depth-varying grain density can then be used to estimate porosity from the bulk density log.

FRACTURES AND FLOW

In this section we compare several types of flow-related measurements with wireline logs. A usable flow profile in open hole was obtained only in hole T-2 using the Schlumberger diverter flowmeter (figure 32). With the holes cased and perforated, flow profiles were obtained in all five T-holes using the Schlumberger full-bore spinner. In addition, we have the temperature log in C-1 as an indicator of fluid loss, and the records of maximum pressure applied during acidization.

Logs that can be used for fracture detection fall into two groups: borewall imaging and conventional open-hole logs. Imaging tools include television, televiewer, and formation microscanner; of these three, only television was run in one well, T-1. The dipmeter can also be considered as an imaging tool and we first show some comparisons between the dipmeter and television.

Figure 31 displays traces from the four dipmeter pads, with conductivity increasing to the left. Fractures detected with the television log are shown as ticks in the depth column. Hand-drawn arcs link the dipmeter response to fractures wherever conductive excursions could be correlated across several pads to a fracture. The television depths are generally one to three feet deeper than the dipmeter depths, an acceptable depth discrepancy. Some of the correlations are quite satisfactory, such as the ones from 1720 to 1740 feet; others are rather tenuous, such as the ones from 1770 to 1776 feet. In the interval from 1782 to 1800 feet, the lack of recognizable dipmeter excursions precluded any correlations with fractures. Overall, the record is mixed: not all fractures from television produce a correlatable conductive event, and not all conductive excursions can be matched with a visually detected fracture. However, there are enough correlations to believe that an electrical imaging tool (the formation microscanner) would be effective in detecting many of the conductive fractures. Of course, the question would remain: which fractures are permeable? A more direct approach is to compare logs with flow tests.

Of the open-hole logs, none can be considered as a direct indicator of permeability. However, several different logs have been found to serve as fracture indicators in some circumstances. Permeable zones are expected to occur in zones of high porosity, so a porosity log is the simplest indicator. If fractures are filled with conductive fluids or clays, then various combinations of electrical resistivity logs sometimes can be effective. The sonic arrival times and energies, particularly of the Stoneley wave, can be used. And finally, if borehole rugosity is due to fractures, then the caliper and the correction trace from the density tool may show correlations with flow. All of these logs are compared with the flow-related measurements. Keeping with the conventions for logs, we plot porosity and flow parameters increasing to the left.

The flow profiles shown in track 2 of figures 33 to 37 all show that most of the flow exited from the lowermost 10 to 25 feet of the perforated interval. The proportions of flow leaving these lowermost intervals range from 38% in T-4 to 63% in T-3 (Table 9). All five holes also show significant exodus from the uppermost intervals. To account for the low injection rates in T-1 and T-5, the nominal injection rate in a hole (fig. 3) has been multiplied by the fractional flow in each interval, so that the units plotted are gallons per minute. The resulting scaling of flow serves as a reminder that because of measurement resolution, the flow variations in T-1, for example, are much less significant and are less reliable, than in T-4.

First examine the electrical resistivity logs acquired with the laterolog tool, lls and lld, in figures 33, 36, and 37. In fractured rock with dominantly vertical fractures, the shallow and deep laterolog curves separate, with the shallow resistivity less than the deep resistivity (Rasmus, 1981; Sibbit and Faivre, 1985). In figures 33, 36, and 37, no such separation is seen. The lack of such separation is an argument against the concept of vertical fractures being predominant in the granite.

Now compare the flow profiles and sonic arrival times. We expect the arrival times to increase where flow increases. The best correlation occurs in well T-4 where the sonic times and the porosity both mimic the flow increase from 1569 to 1670 feet. No fluid exodus was detected from 1670 to 1755 feet, where the sonic arrival times are low. The large flow loss in the lowermost interval correlates with increases in sonic arrival times and porosity. In other wells, we see that the flow losses in the lowermost and uppermost intervals always coincide with increases in sonic arrival time. However, there are several instances where increases in sonic arrival time are not accompanied by flow increases (e.g., 1675-1710 feet in T-2). Sonic arrival times are very useful in delineating potential permeable zones, but they also show fractured intervals that are not permeable.

Even with the good correlation between sonic arrival times and fluid exodus, there is still something puzzling about the preponderance of flow from the lowermost intervals. Why is the lowermost zone consistently the highest flow zone in all five wells? It is more puzzling when we realize that the lowermost zone in T-3, through an accident in depth control, is some 20 to 30 feet deeper than the other holes. It seems possible that this coincidence may be in part an artifact of the completion. We know from theoretical work that a well that partially penetrates an aquifer distorts the potential and the velocity field around the lower extremity of the well (Muskat, 1937, fig. 81). This distortion must produce a higher flow into (or in our case, out of) the bottom interval of the well than in the center portion where the potential field is not distorted. Unfortunately, Muskat does not give an analytical solution for the flow distribution within the well.

Sonic waveforms were obtained with Schlumberger's sonic array tool in the five T-wells (Table 6). Data from two wells, T-1 and T-3, were processed to produce energy absorption curves for the Stoneley wave as well as the compressional and shear. The Stoneley wave is of interest because variations in its properties have been correlated with permeable fractures. The third arrival on most sonic waveforms, the Stoneley wave is a guided mode that travels along the interface between the rock and borehole fluid (Astbury and Worthington, 1986). Compression and expansion of the borehole fluid results in a "pumping" action where a permeable fracture occurs. The consequent loss of energy between receivers spanning a fracture can be diagnostic of the presence of the fracture.

After separation of the modes, the waveform is filtered and windowed (Brie et al., 1988). Relative energies are computed by squaring the resulting waveform. Differential energies are then calculated by taking differences between receivers in the array and averaging. Two schemes are used to minimize the effects of coupling between the tool and the rock, and these two results are averaged to form the normalized differential energy (nde). A decrease in nde corresponds to increased attenuation, and can be attributed to a permeable fracture.

In figures 38 and 39 we show the Stoneley mode results computed by Schlumberger for wells T-1 and T-3, accompanied by the flow logs run in perforated casing. The normalized differential energy (nde) curves do not decrease at the flow zones in either well. With the exception of the fractured zone extending from 1400-1480 feet in well T-3, the nde curves increase, not decrease, where the Stoneley energy recorded at a single receiver decreases. These increases in nde, which occur in both T-1 and T-3, can possibly be explained as reflected energy from fracture interfaces (K. Hsu, pers. comm.)

Because of this ambiguity in the nde curve, it seems best to consider the single-receiver energy, displayed immediately to the right of the depth track. The total energy curve does show the fractured interval in well T-3 between 1400 and 1500 feet: total energy is diminshed considerably and slowness increases. However, correlation between the flow profile based on the spinner log (track 1) and the Stoneley wave energy are not consistent. In well T-1, two of the three flow zones occur where the Stoneley energy diminshes, although the energy decrease at the depth of the most prominent flow zone is modest. In well T-3, there is no correlation between the lowermost flow zone and Stoneley energy. This lack of correspondence in well T-3 is disappointing.

CONCLUSIONS AND RECOMMENDATIONS

1. The complete logging suite used on the T-wells made it possible to learn a great deal concerning which logs are effective. For instance, we found that the induction tool produces erratic values in the presence of highly conductive sulphide veinlets whereas the laterolog produces reasonable responses. Consequently, the laterolog should be retained and the induction log should be dropped from future logging programs. The value of the dipmeter is questionable; it is probably more profitable to experiment with other imaging tools such as the televiewer and the formation microscanner. The television remains a candidate for imaging if a clear fluid and clean walls can be maintained in the borehole.

2. The logs show remarkably few correlations of physical property variations from one T-well to another. In other words, there are almost no indications of horizontal layering in either the upper or lower ore zone, not a surprising finding in Precambrian granite. An outstanding exception is the diabase sill, intersected by all five T-wells between 1410 and 1450 feet (figure 12). The sill occurs at the lower boundary of the upper ore zone. With this exception, hole-to-hole correlations are almost non-existent, that is, variations in porosity and alteration as manifested by variations in the logs, do not extend laterally over interwell distances of 90 feet.

3. A noteworthy feature is the fracture zone intersected by T-3 at a depth of 1400 to 1500 feet. It is best diagnosed by the increases in sonic transit times (figures 9 and 16) and decreases in sonic amplitude (figure 39). The degree of alteration does not appear to be any higher than in surrounding rock.

4. Of the candidates for "permeability indicators", the sonic array tool, with attendent processing to obtain energy as well as travel time, appears to be the most useful. Comparisons between sonic logs and flow logs were not entirely satisfactory on the T-wells. The flow logs were obtained after casing was installed and perforated, so the flow regime could have been influenced by the combination of casing and rock, rather than by the rock properties alone. For future work, we recommend that flow tests be done in open hole and compared to sonic travel time and attenuation.

5. The elemental determinations from the geochemical tool were flawed by omission of a boron sleeve from the open-hole run and by difficulties in compensating for casing and cement in the cased-hole runs. Some problems were mitigated by setting calcium to zero for a test calculation; the resulting mineralogical and porosity estimates were reasonable and encouraging. However, the calculations deserve rework, both to better account for the igneous environment and to deal more effectively with environmental corrections.

6. The association of chloride with copper (and apparently, only with copper) in this oxide ore body makes possible the direct detection of ore with nuclear logging tools. In particular, we have shown that the chlorine yield, in association with other logs, provides a powerful "predictor" of copper. Improvements in the chemical and mineral analysis from

nuclear logs can only improve the prediction capability.

7. Porosity averages 7.5%, based on core samples from the lower ore zone. Linear transforms of individual open-hole logs do not provide viable porosity estimates. Porosity estimates obtained simultaneously with mineral estimates from the geochemical logs are somewhat lower than the core values. Refinement of the geochemical computations is recommended before the porosity estimates are used for engineering purposes.

ACKNOWLEDGEMENTS

The data presented in this report has been drawn from many sources which have been acknowledged where possible. H. Kreis of ASARCO contributed the geological data, explained the geological concepts, provided samples, and made several important suggestions. D. Johnston of Schlumberger performed most of the calculations on the logs from the T-wells; P. Scholes of Schlumberger provided information on data acquisiton. J. Mikesell of the USGS contributed ideas on the neutron activation data and the problems inherent in extracting elemental estimates. D. Davidson and C. Manikas of SAIC provided the results of flow tests and well construction. D. Early, S. Paulson, and L. Dahl of the U. S. Bureau of Mines provided data and ideas on petrology, rock properties, and fractures. J. Kibler of the U. S. Geological Survey performed much of the data compilation and presentation of the figures in this report. And finally, D. Davidson of SAIC, S. Swan of the U.S. Bureau of Mines, and A. Raihl of ASARCO provided the support and cooperation required to keep us involved in a multi-faceted project conducted by diverse organizations.

REFERENCES CITED

Astbury, S. and M.H. Worthington, 1986, The analysis and interpretation of full waveform sonic data, First Break vol. 4, no. 4, p. 7-16.

Brie, A., K. Hsu, and C. Eckersley, 1988, Using the Stoneley normalized differential energies for fractured reservoir evaluation, paper XX in Soc. Prof. Well Log Analysts 29th Annual Symposium Trans., 25 p.

Clark, S.P., Jr., Z. E. Peterman, and K. S. Heir, 1966, Abundances of uranium, thorium, and potassium, in Handbook of Physical Constants, S.P. Clark, Jr., ed., Geol. Soc. of America Memoir 97, pp 521-541.

Eberhart-Phillips, D., D-H Han, and M.D. Zoback, 1989, Empirical relatinships among seismic velocity, effective pressure, porosity, and clay content in sandstone, Geophysics, vol. 54, no. 1, pp. 82-89.

Ellis, D. V., 1987, Well Logging for Earth Scientists, Elsevier, New York.

Fertl, W. H., W. L. Stapp, D. B. Vaello, and W. C. Vercellino, 1980, Spectral gamma-ray logging in the Texas Austin Chalk Trend, J. of Petr. Tech. pp 481-488.

Hearst, J. R and P. H. Nelson, 1985, Well Logging for Physical Properties, McGraw-Hill, New York.

Herron, S.L., M.M.Herron, J.A. Grau, and D.V. Ellis, Interpretation of Chemical Concentration Logs and Applications in the Petroleum Industry in Remote Geochemical Analysis: Elemental and Mineralogical Composition, C. Pieters and P. Englert, Eds., in press.

Hertzog, R. et al., 1989, Geochemical Logging with Spectrometry Tools, SPE Formation Evaluation, June, p. 153-162.

Melzer, L. Stephen, 1990, Review of borehole video camera images performed in the T-wells on 7 July 1990, memo to A. Raihl of ASARCO, 16 pp.

Montgomery and Associates, Inc.,1990, Summary of results of laboratory chemical analyses for routine constituents for groundwater samples obtained from injection and recovery test wells T-1, T-2, T-3, and T-5, four data sheets, Tucson, Az.

Muskat, M., 1937, The flow of homogeneous fluids through porous media, McGraw-Hill Book Co., New York.

Nelson, Philip H., 1988, Well logs from Shads No. 4 (Amoco), Catoosa, Oklahoma, U. S. Geological Survey Open-File Report 88-584, 11 p.

Piers, G. E., 1989, Inflatable diverter flowmeter, paper CC in Trans. 30th Annual Logging Symposium, Soc Prof. Well Log Analysts, 21 p.

Rasmus, John C., 1981, Fluid evaluation of fractured hydrocarbon intervals in the Twin Creek Formation of the Yellow Creek Field, Soc. Petr. Engr. no. 9587, Low Permeability Symposium, Denver.

Sibbit, A.M., and O. Faivre, 1985, The dual laterolog response in fractured rocks, paper T in Trans. 26th Annual Logging Symposium, Soc. Prof. Well Log Analysts, 34 p.

Shen, L. C., 1989, Effects of skin-effect correction and three-point deconvolution on induction logs, The Log Analyst, July-August, p. 217-224.

Walpole, Ronald E. and Myers, Raymond H., 1989, Probability and Statistics for Engineers and Scientists, Macmillan Publishing Co., New York.

West, F. G. and A. W. Laughlin, 1976, Spectral gamma logging in crystalline basement rocks, Geology v. 4, pp. 617-618.

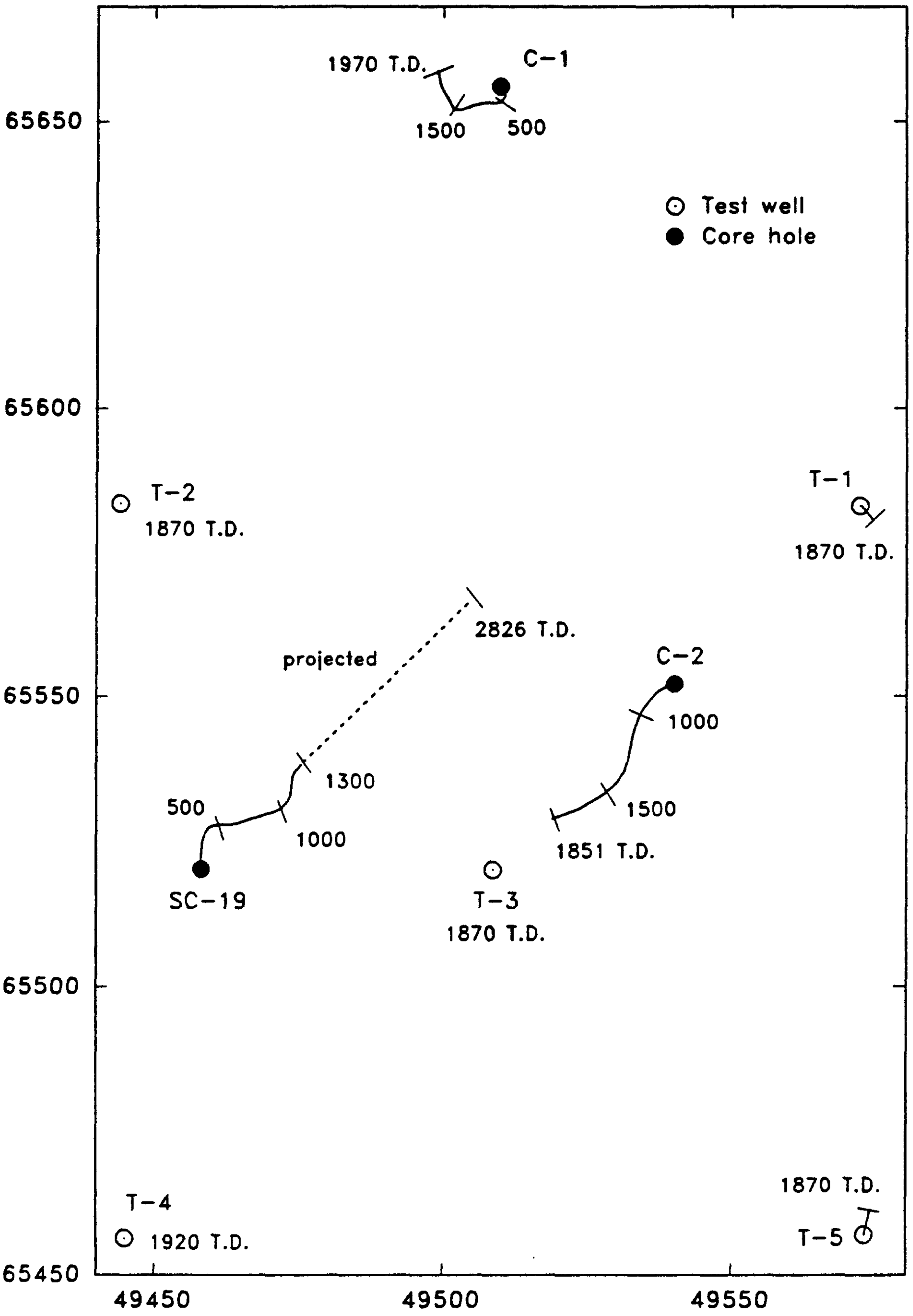

Figure 1. Plan map of cored holes and rotary test wells for leach tests. Distance between central injection well T-3 and any one of the peripheral recovery wells, such as T-2, is 90 feet.

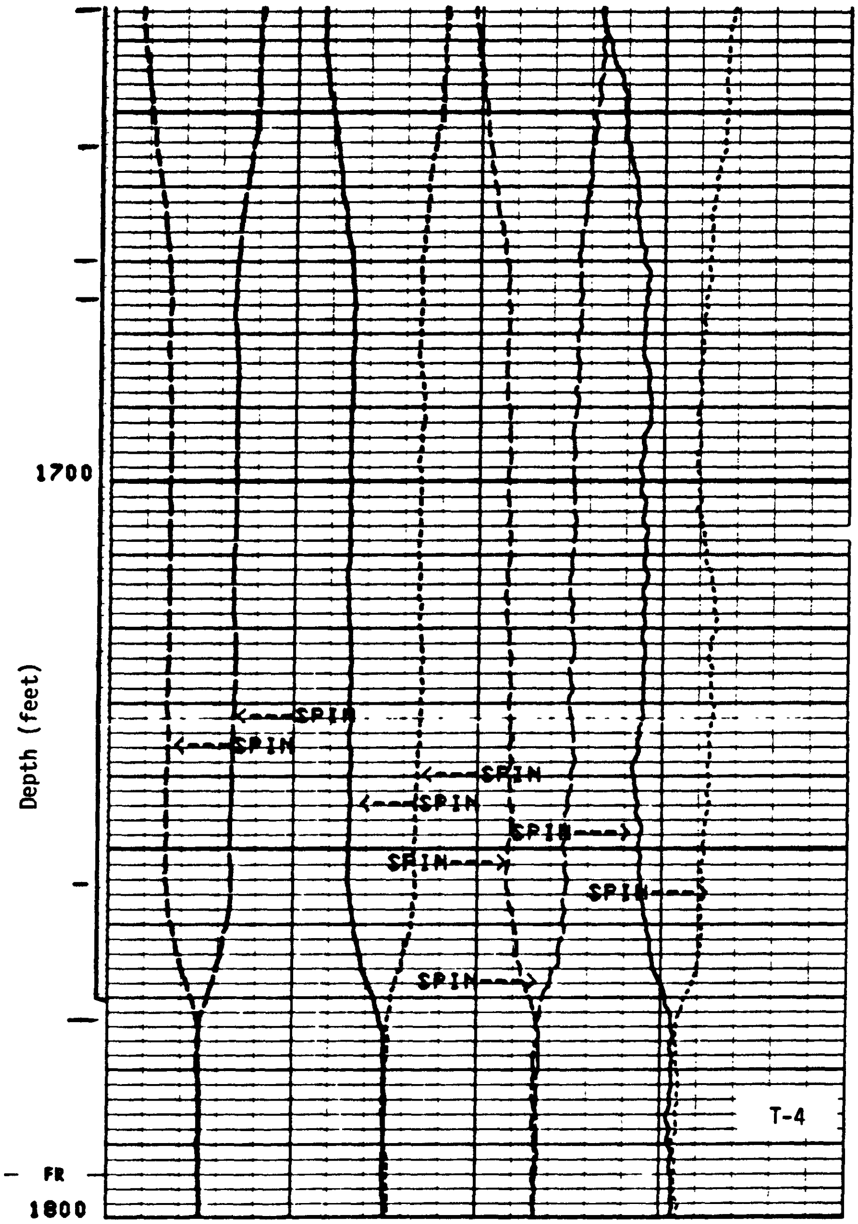

Figure 2. Flow logs obtained with full-bore spinner during injection in well T-4. Right-hand pair obtained at lowest logging speed; left-hand at highest. Each pair of traces consists of a down-run (left) and an up-run (right). Spin rate is 2.5 revolutions per second per large chart division. Ticks in depth column show intervals of similar flow character; a change in spin rate is attributed to fluid exodus.

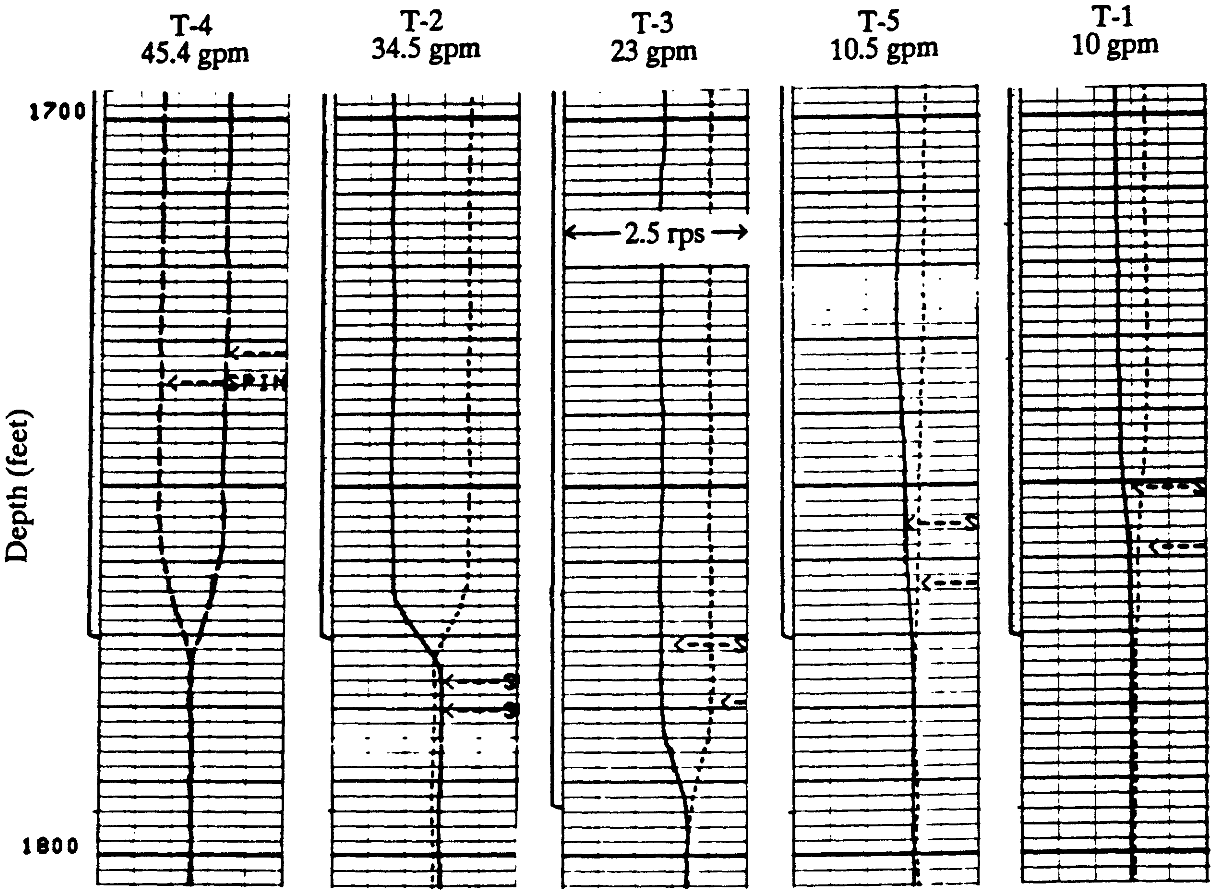

Figure 3. Spinner logs from lower section of five T-holes, obtained at highest logging rate. Typical injection rates given at top. Spin rate in revolutions per second (rps).

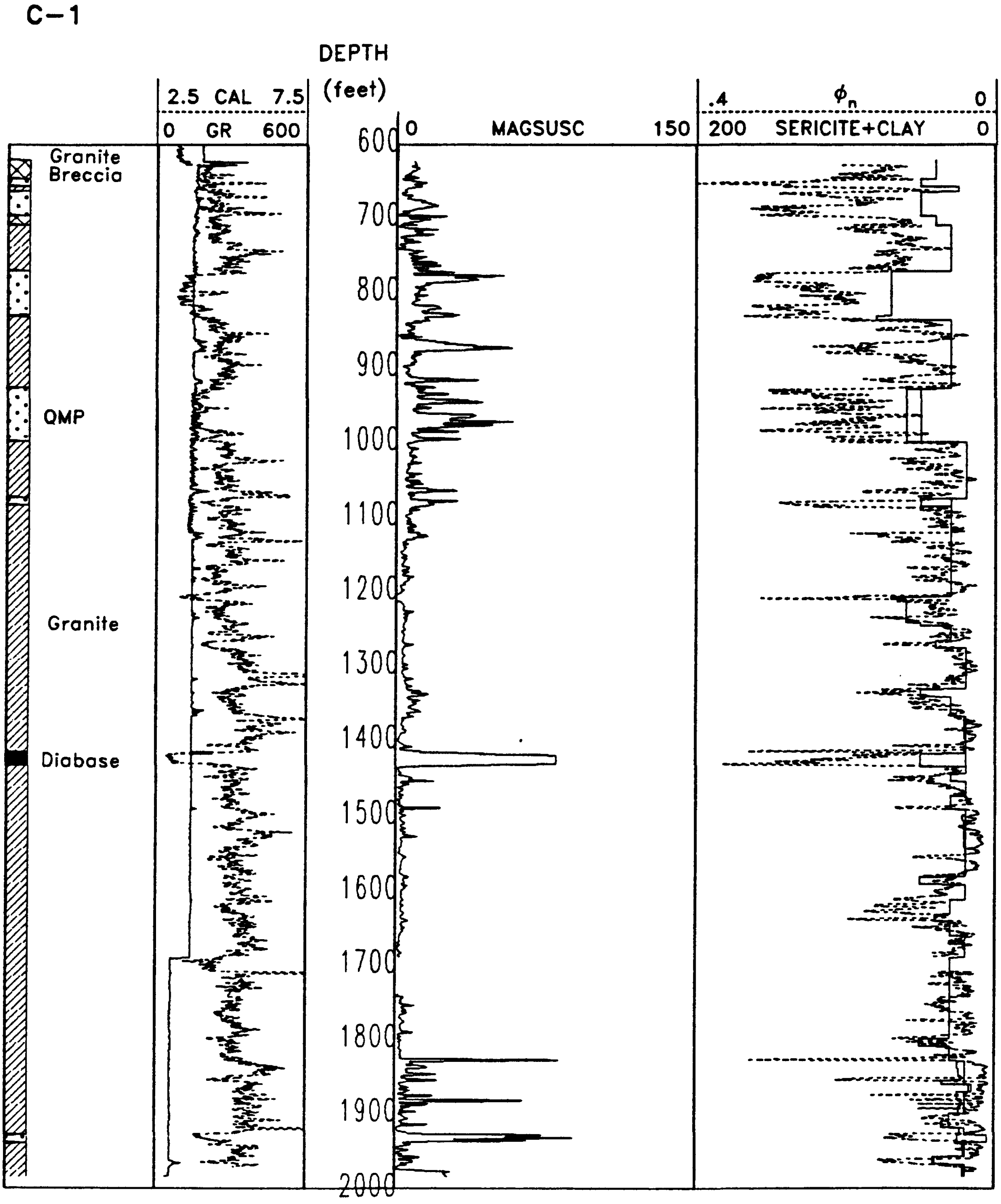

Figure 4. Magnetic susceptibility, neutron porosity (ϕ_n), and other logs from cored hole C-1. Visual estimate of sericite plus clay is shown with neutron porosity.

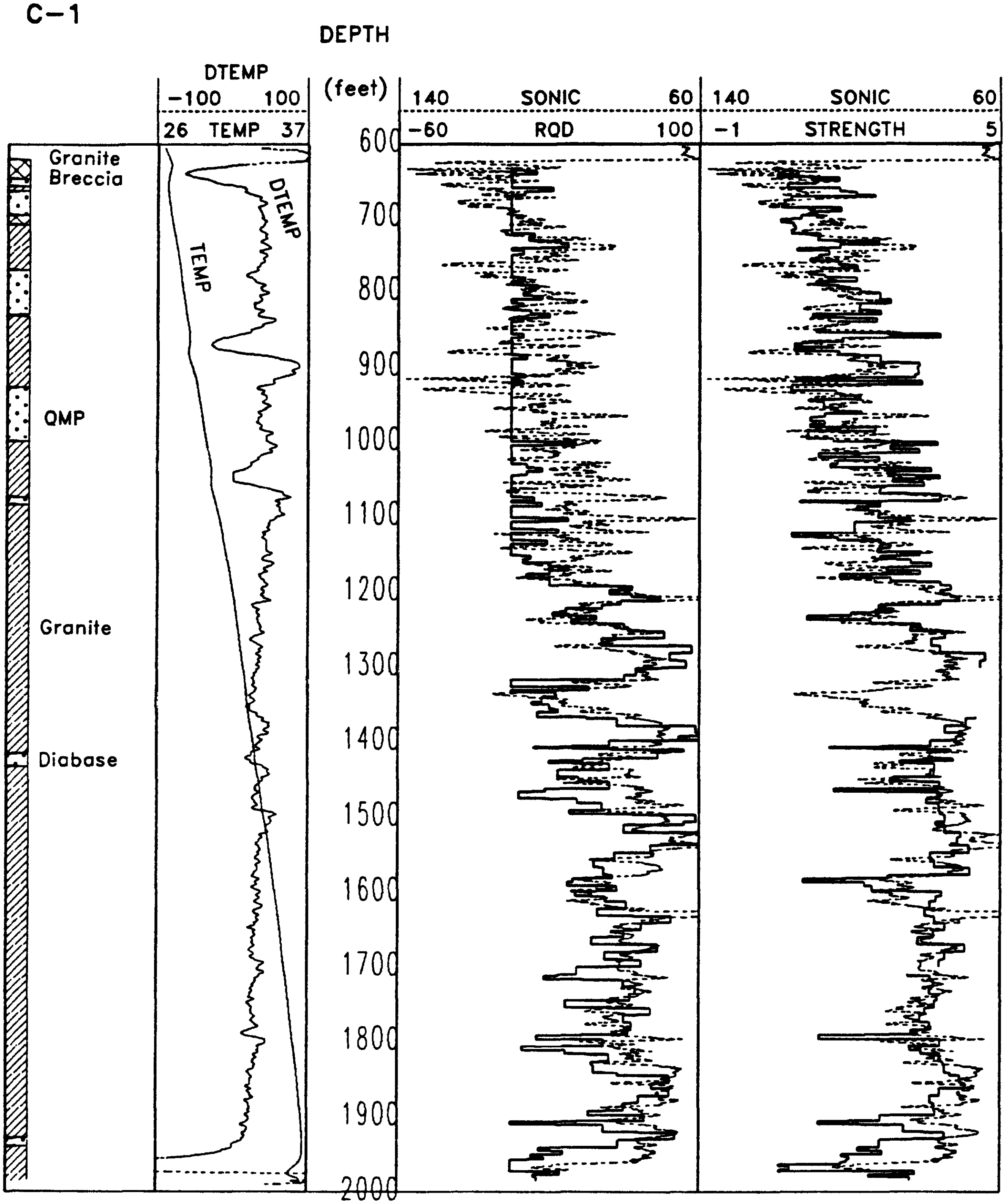

Figure 5. Sonic and temperature logs from cored hole C-1. Rock quality designation "RQD" and "strength" indices are based on inspection of core.

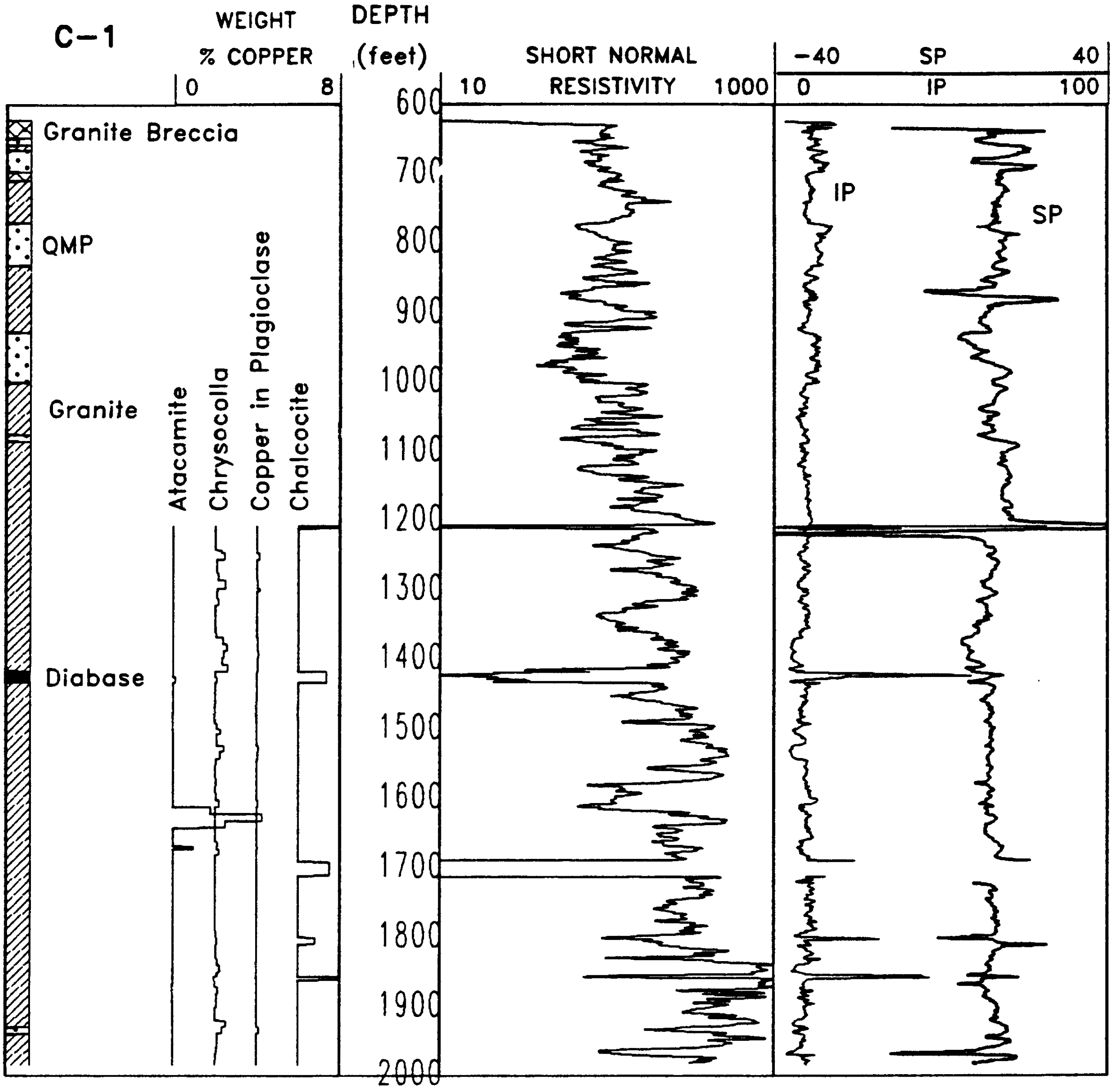

Figure 6. Electrical logs (resistivity, induced polarization, and spontaneous polarization) and copper analyses, prorated among four minerals, from cored hole C-1.

Figures 7-11. Nomenclature for Schlumberger logs, holes T-1 through T-5.

Type of Log	Symbol	Units
Gamma Ray	GR	API
Caliper	Cal	inches
Temperature	Temp	degrees Fahrenheit
Bit Size	Bit	inches
Uranium	U	ppm
Potassium	K	weight percent
Thorium	Th	weight percent
Micro-spherically focused log	msfl	ohm-m
Shallow laterolog	lls	ohm-m
Deep laterolog	lld	ohm-m
Self potential	sp	millivolts
Spherically focused log	sfl	ohm-m
Medium induction	ilm	ohm-m
Deep induction	ild	ohm-m
Compressional transit time	dtcomp	microseconds per foot
Shear transit time	dtshear	microseconds per foot
Stoneley transit time	dtstone	microseconds per foot
Thermal neutron porosity	nphi	volume percent
Epithermal neutron porosity	enphi	volume percent
Bulk density	rhob, ρ_b	gm per cm^3
Photoelectric effect	Pe	barns per electron
Capture cross-section	sigma, Σ	barns

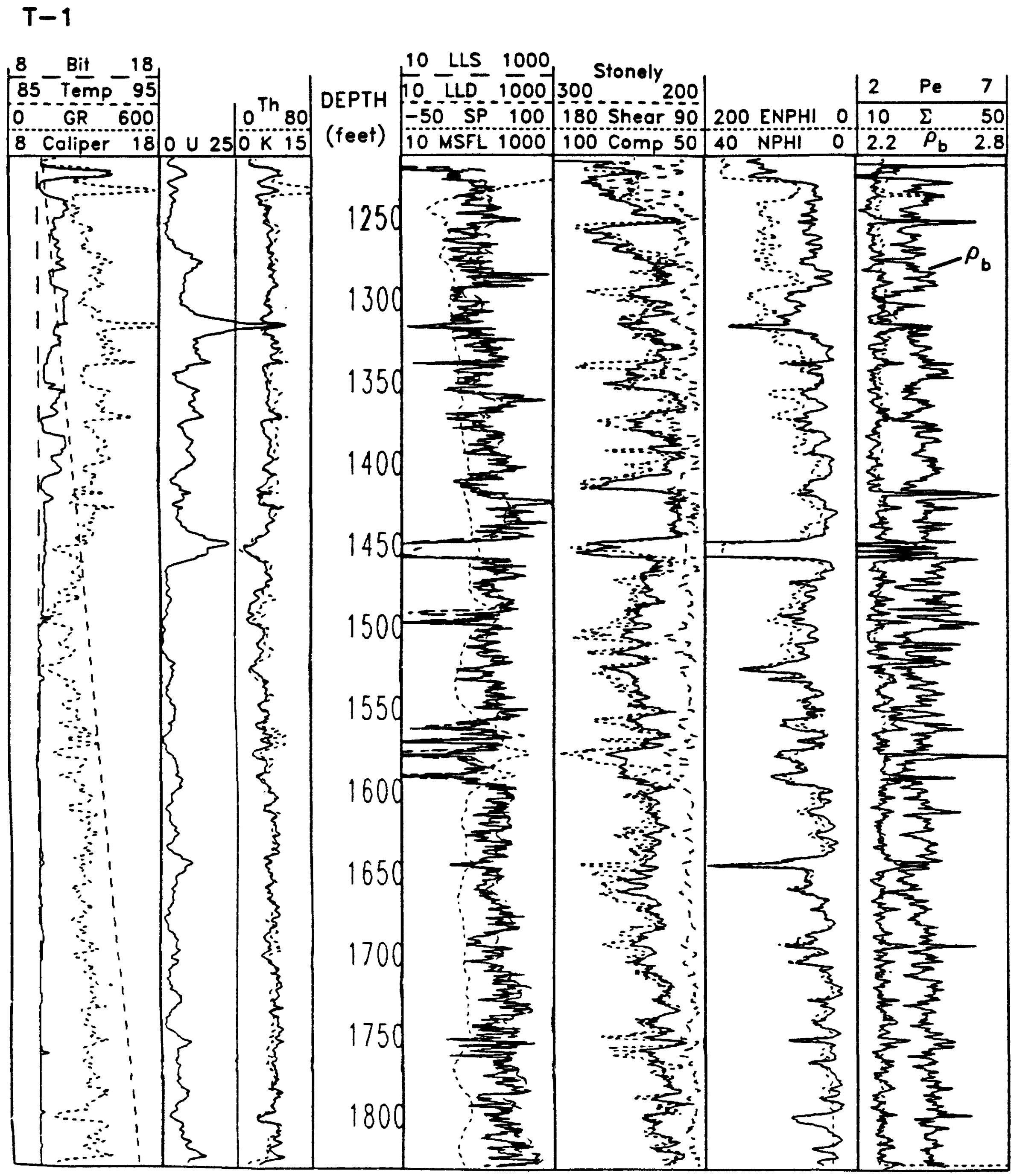

Figure 7. Schlumberger logs from hole T-1.

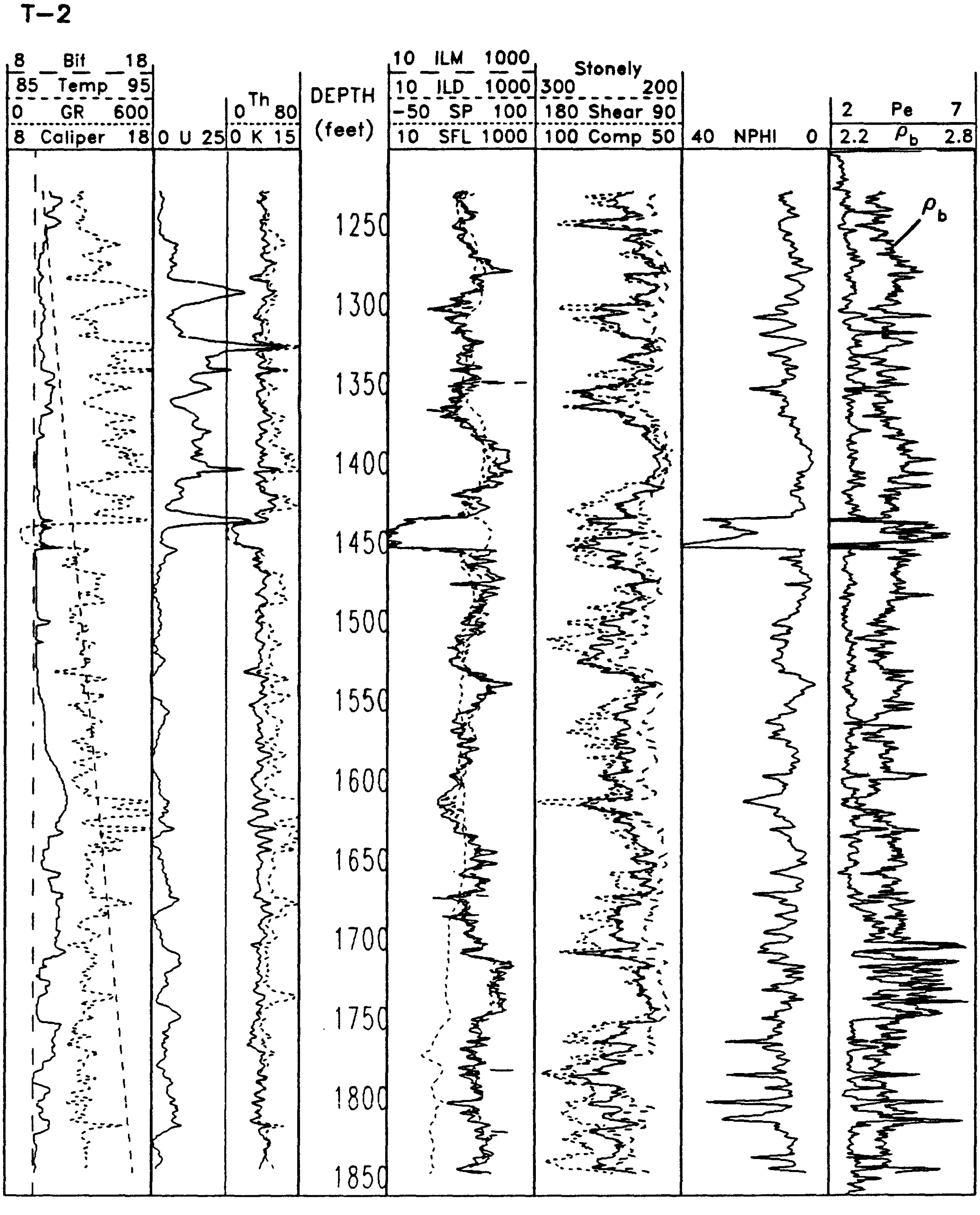

Figure 8. Schlumberger logs from hole T-2.

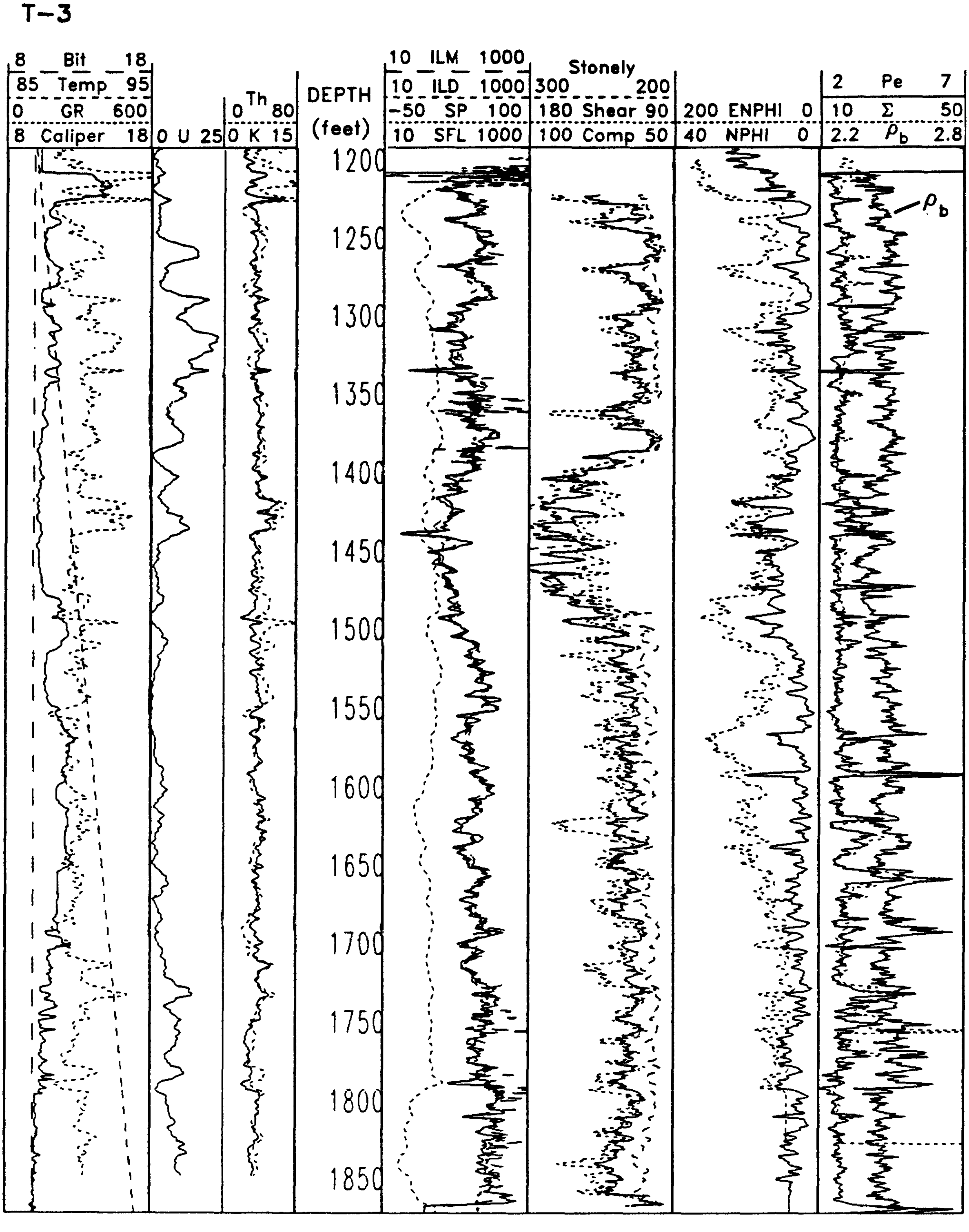

Figure 9. Schlumberger logs from hole T-3.

T-4

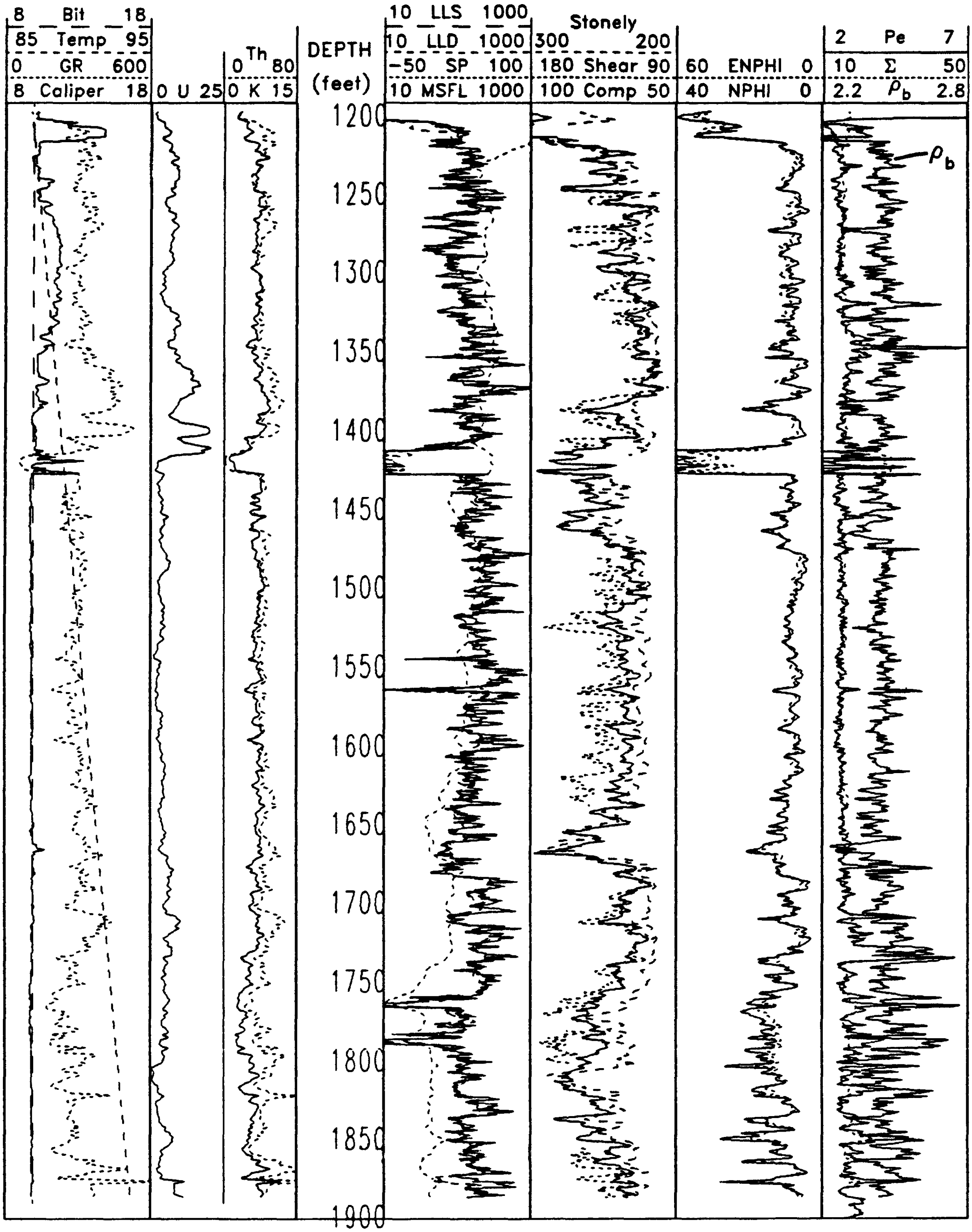

Figure 10. Schlumberger logs from hole T-4.

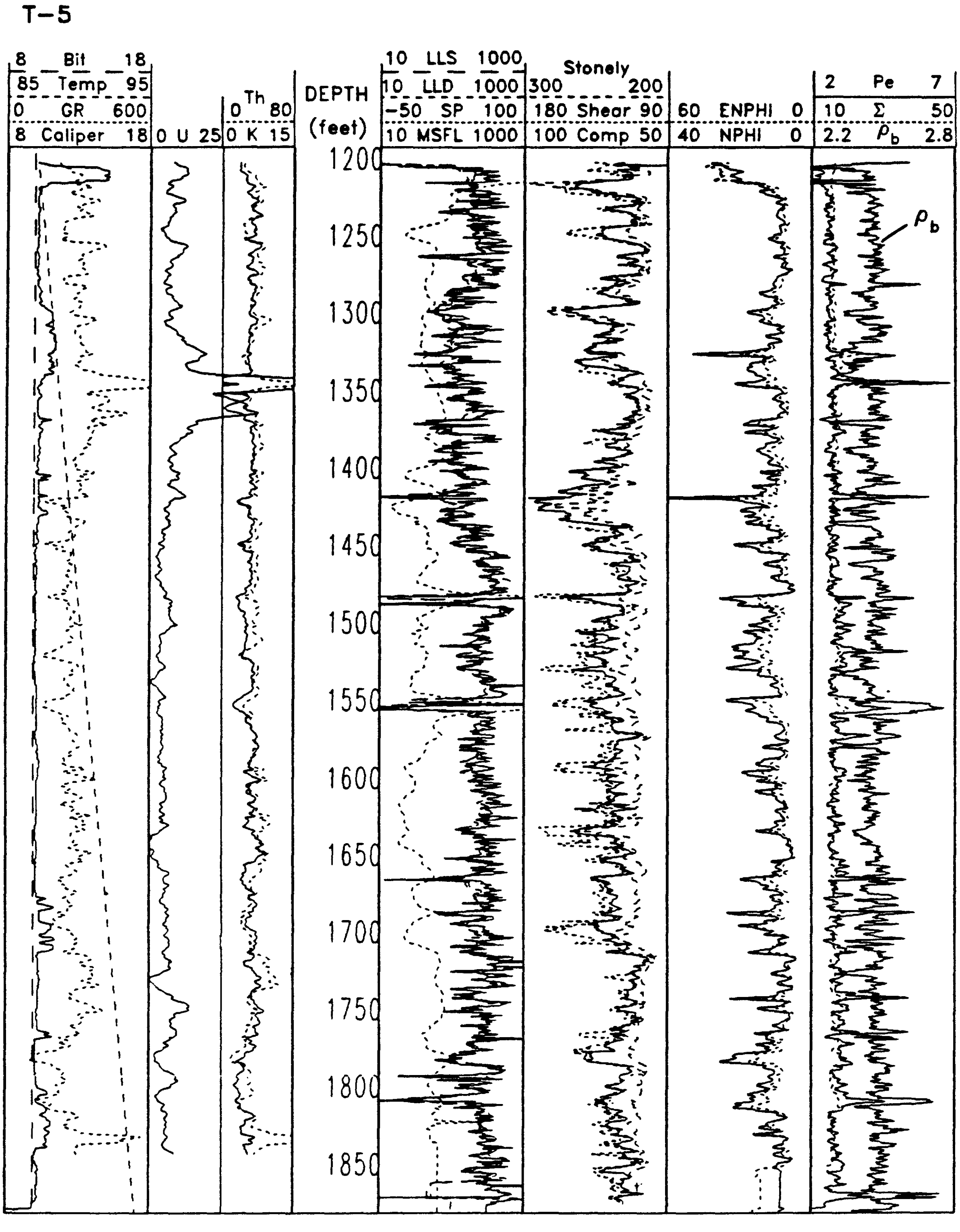

Figure 11. Schlumberger logs from hole T-5.

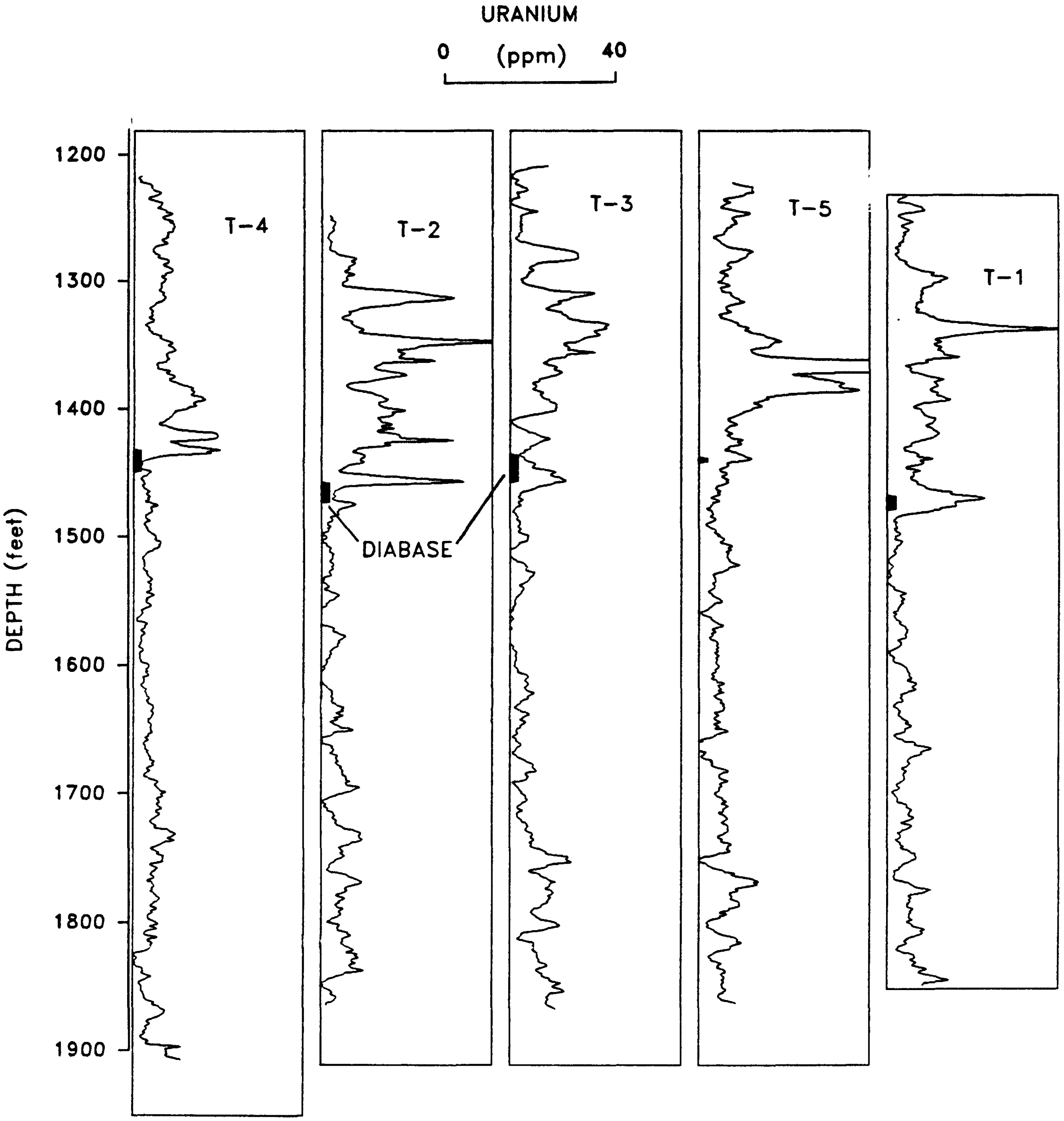

Figure 12. Uranium logs by natural gamma-ray spectrometry in five T-holes. Black box marks location of diabase sill as picked from logs.

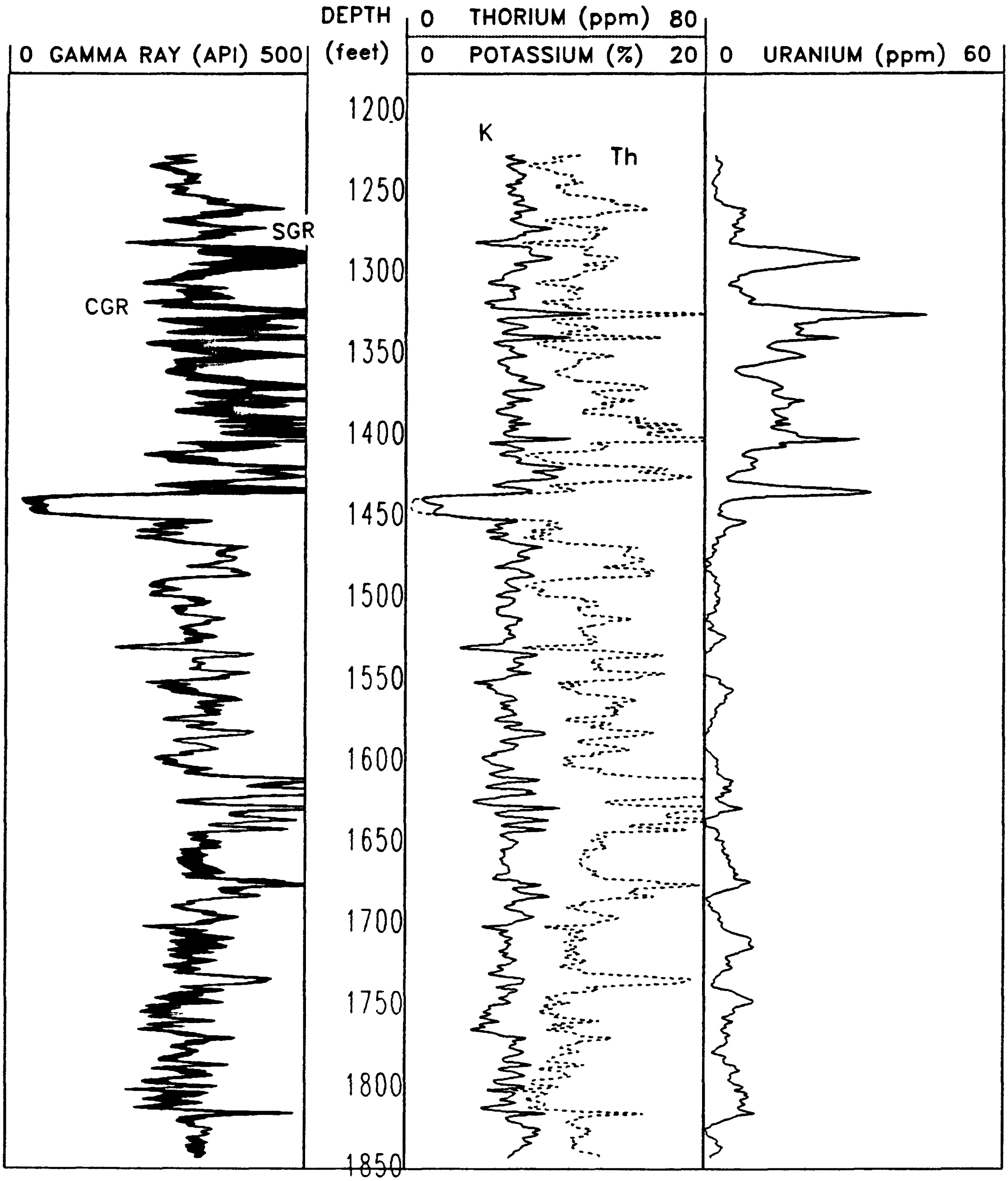

Figure 13. Gamma-ray results from spectral gamma-ray (NGT) tool in hole T-2. Left track shows total natural gamma radiation (SGR) and total less uranium contribution (CGR). Derived concentrations of potassium, uranium, and thorium are shown at right.

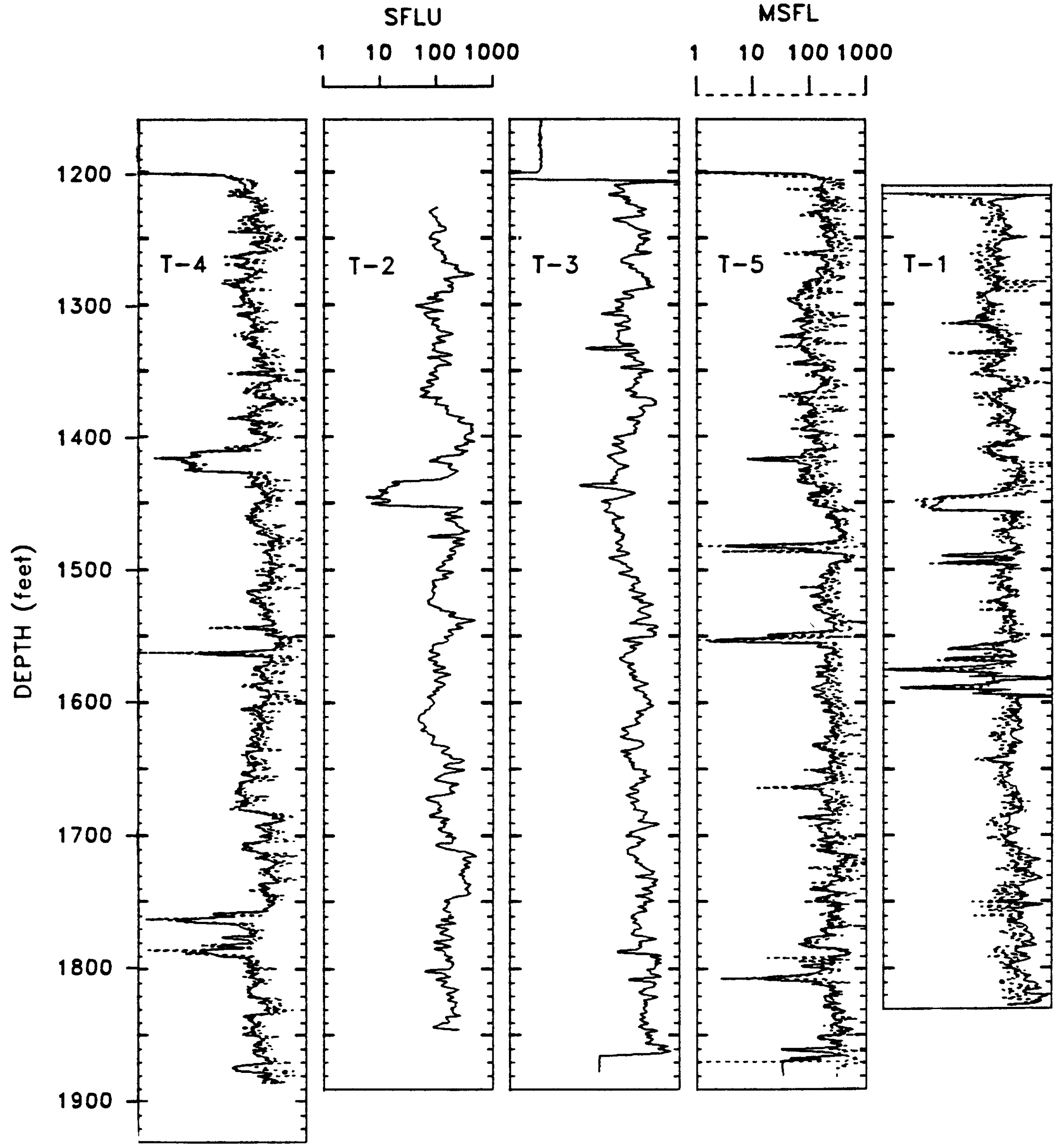

Figure 14. Resistivity logs from a pad tool, the msfl, or microspherically focused log (dashed line), and a mandrel tool, the sfl, or spherically focused log (solid line) in five T-wells.

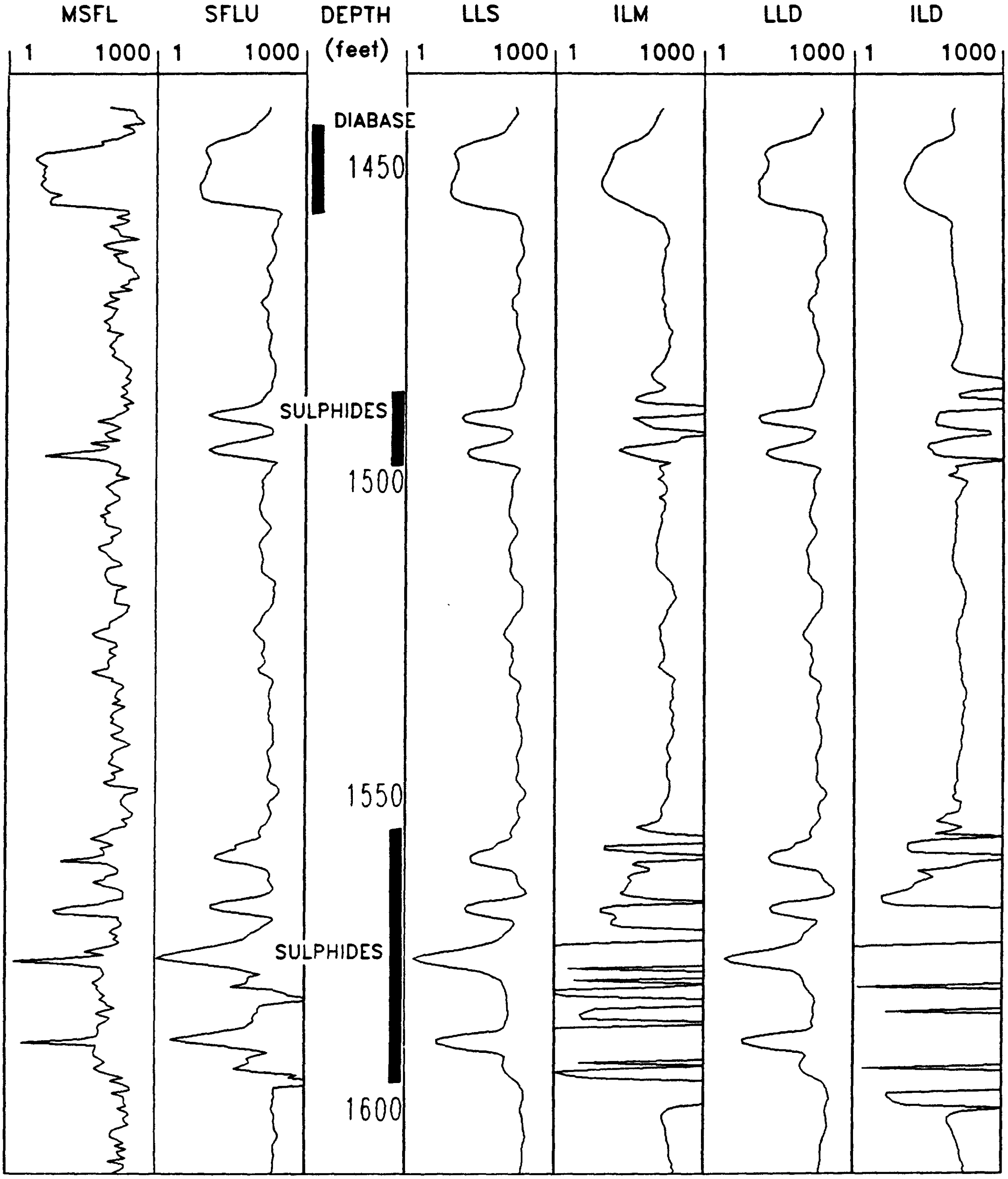

Figure 15. Resistivity logs in hole T-1 from a pad tool (MSFL), a spherically focussed tool (SFL), a shallow (LLS) and deep (LLD) laterolog, and a medium (ILM) and deep (ILD) induction.

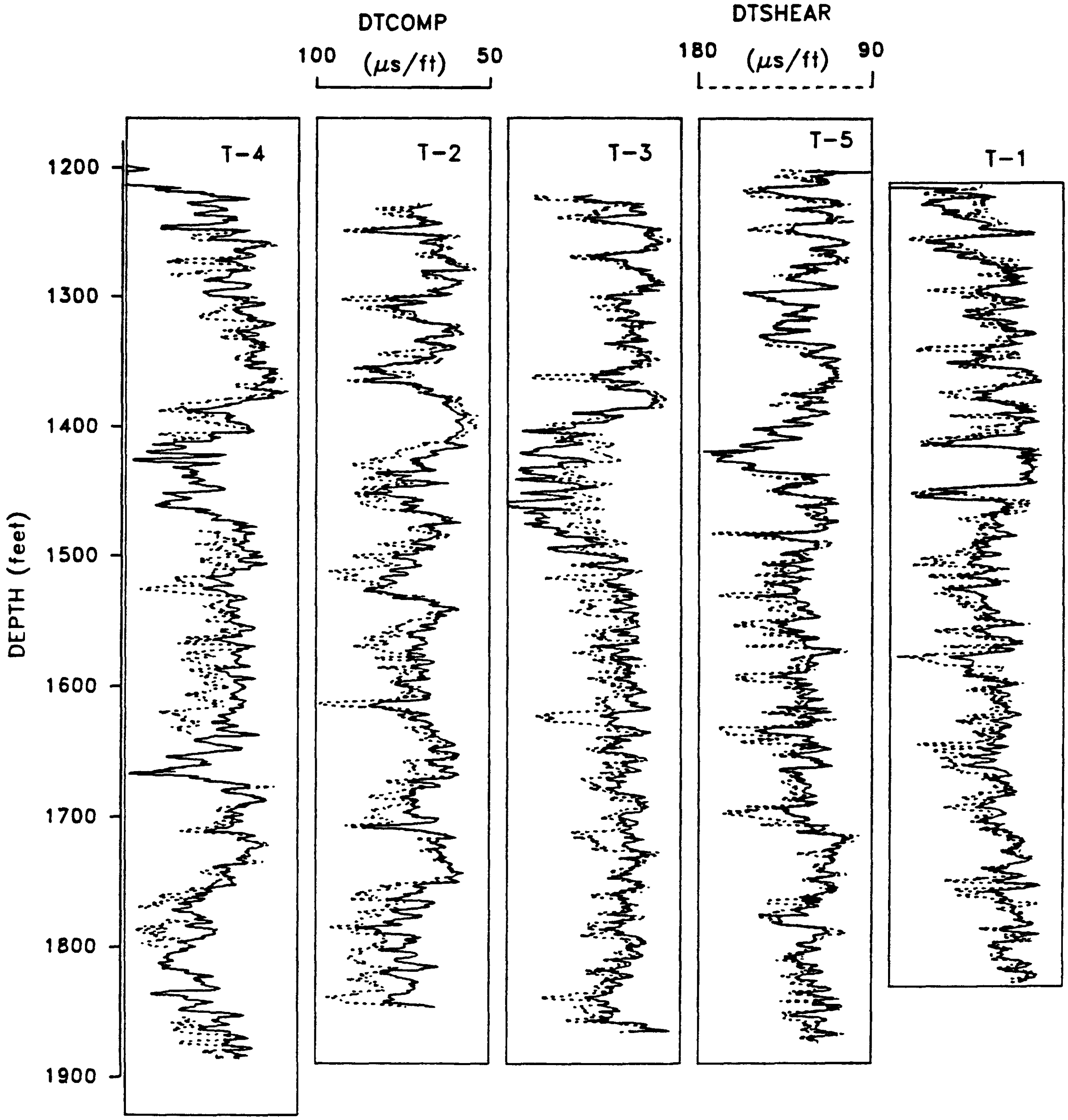

Figure 16. Compressional and shear travel time logs in five T-holes.

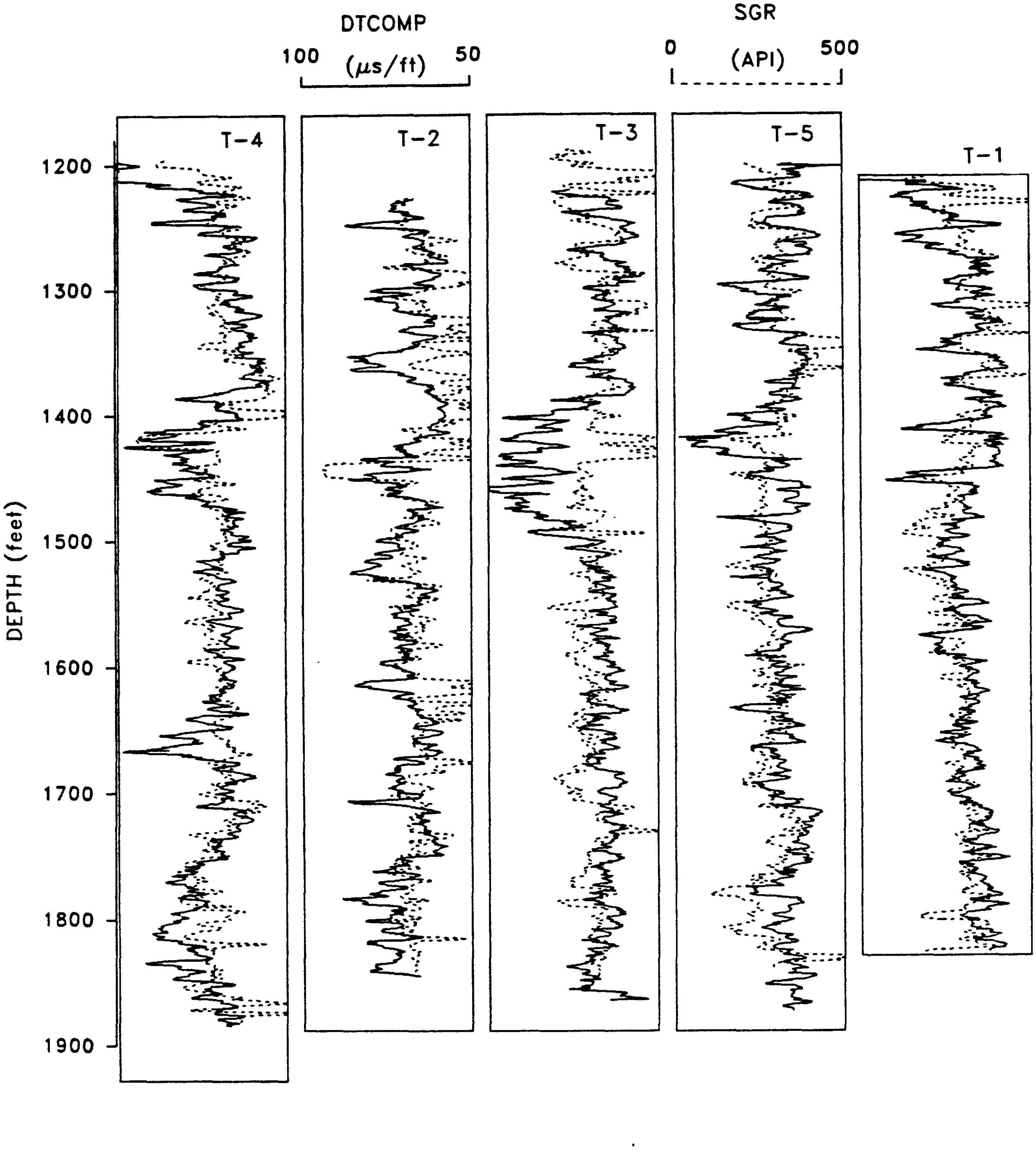

Figure 17. Overlay of compressional travel time (DTCOMP) and total gamma-ray (SGR) logs in five T-holes.

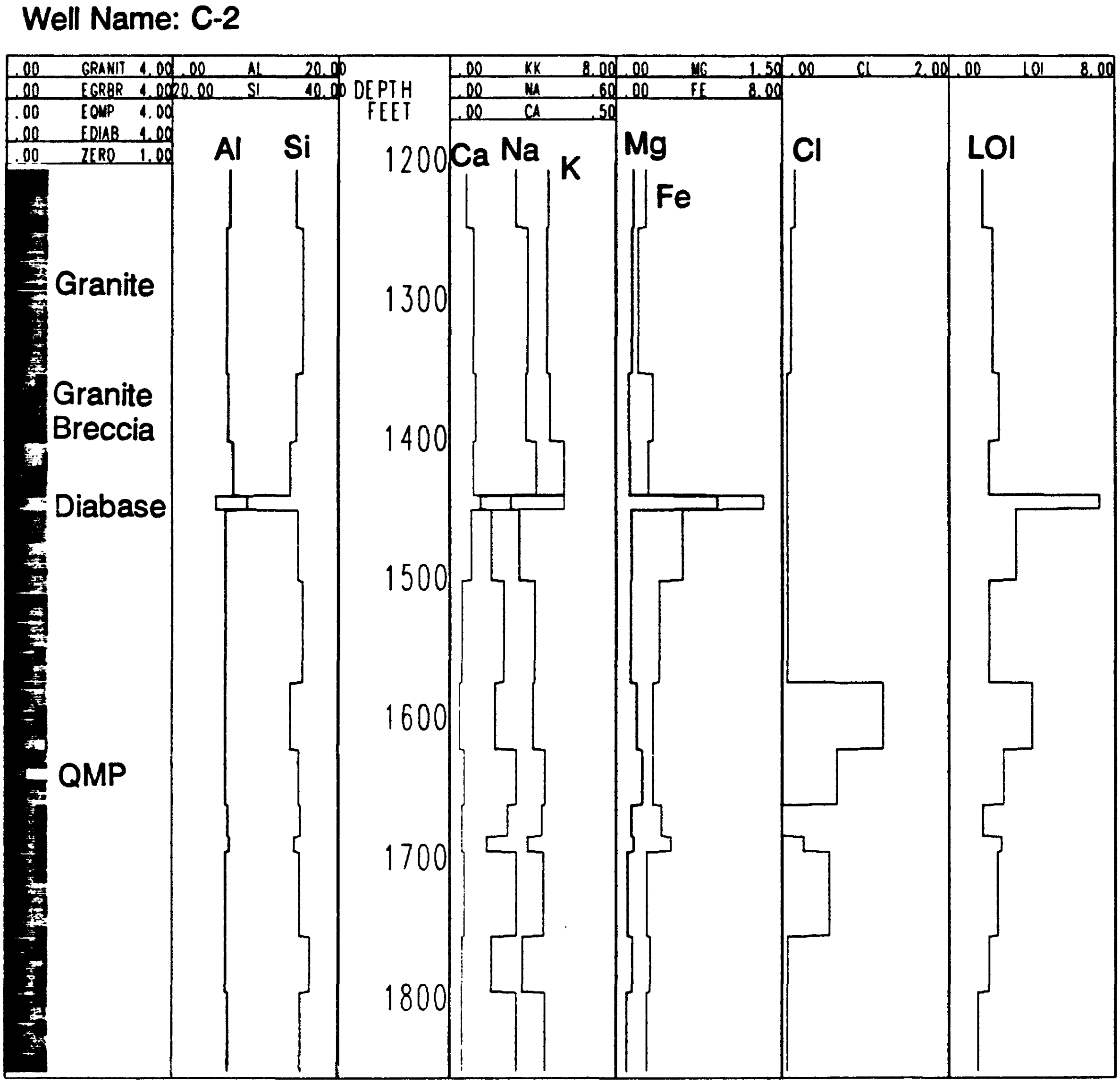

Figure 18. Chemical elements analyzed on composite samples from cored hole C-2. LOI represents loss on ignition.

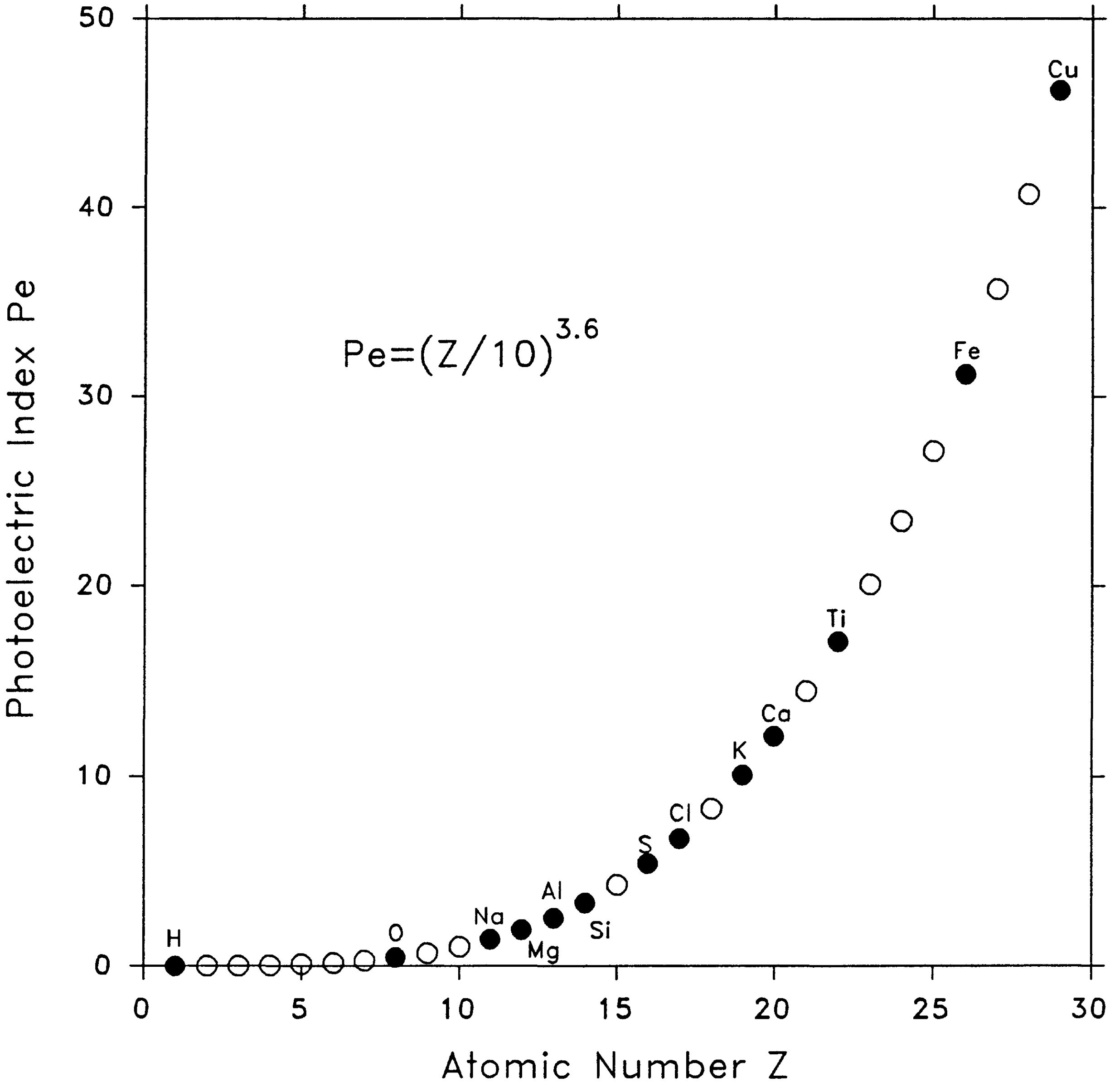

Figure 19. Photoelectric index as a function of atomic number.

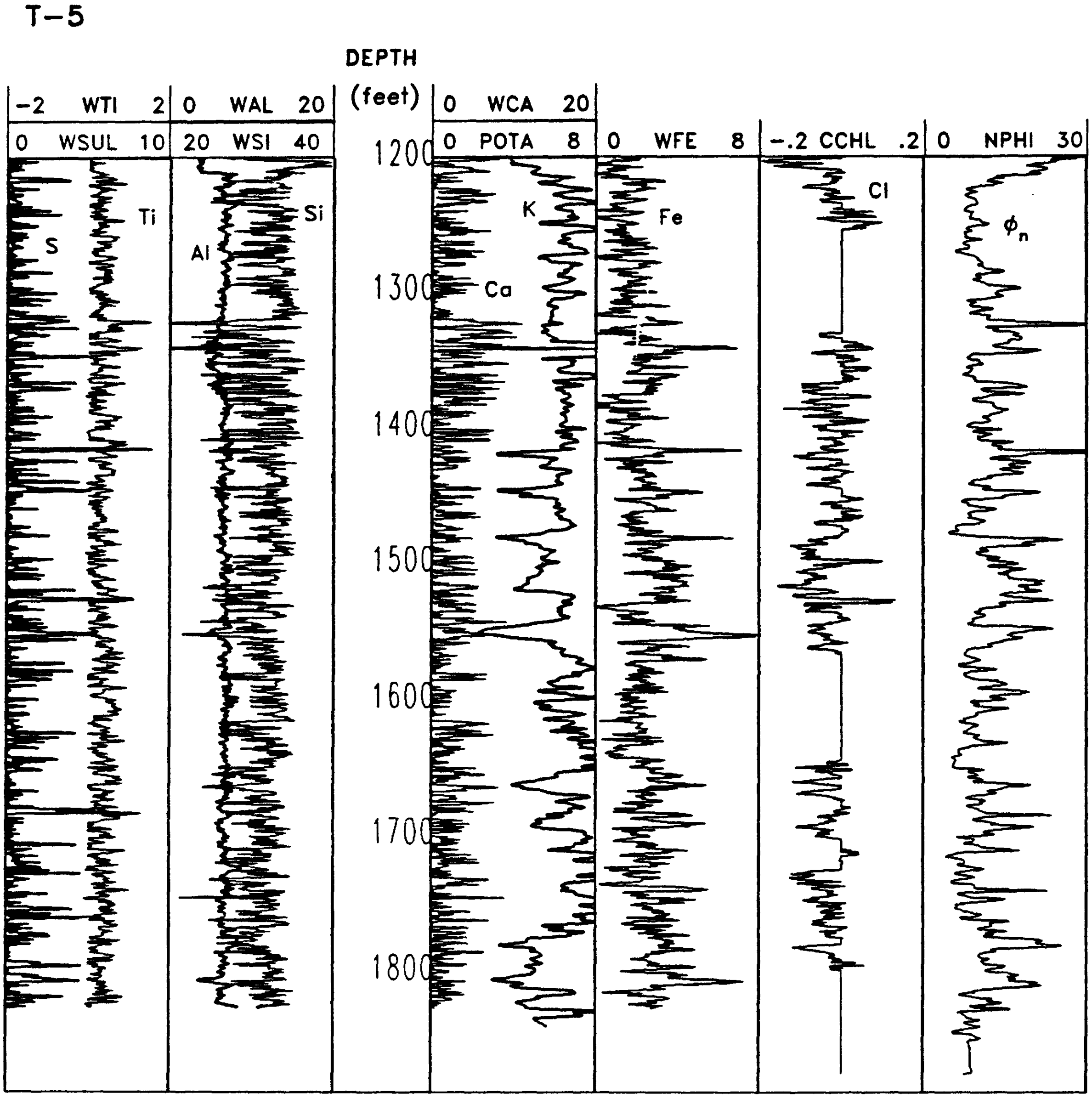

Figure 20. Elemental weight percents from geochemical log in open hole T-5 for titanium, sulphur, aluminum, silicon, calcium, potassium and iron. Also given are chlorine yield and neutron porosity.

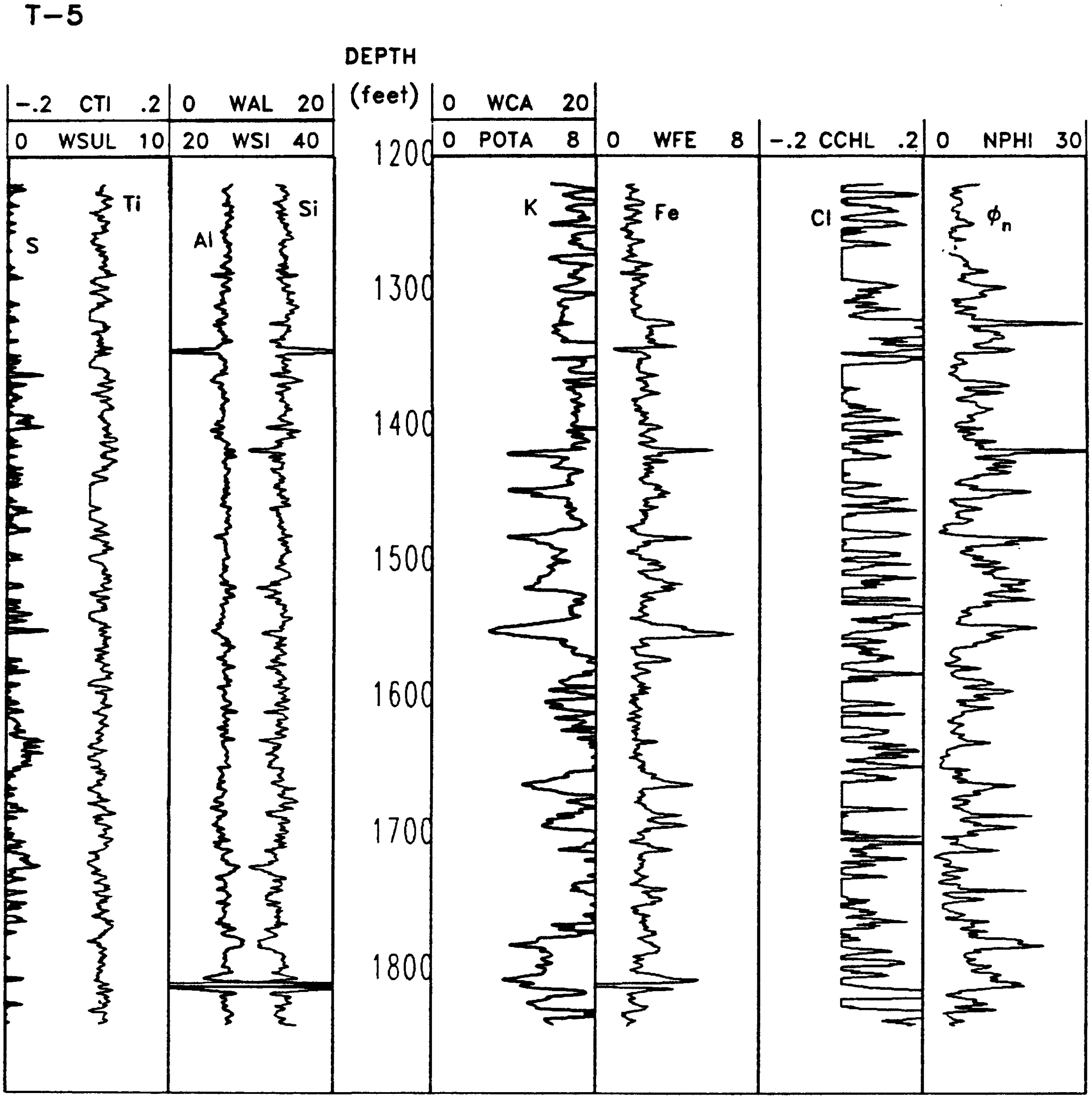

Figure 21. Elemental weight percents from geochemical log in cased hole T-5 for sulphur, aluminum, silicon, potassium and iron. Calcium has been set to zero. Also given are titanium and chlorine yields and neutron porosity.

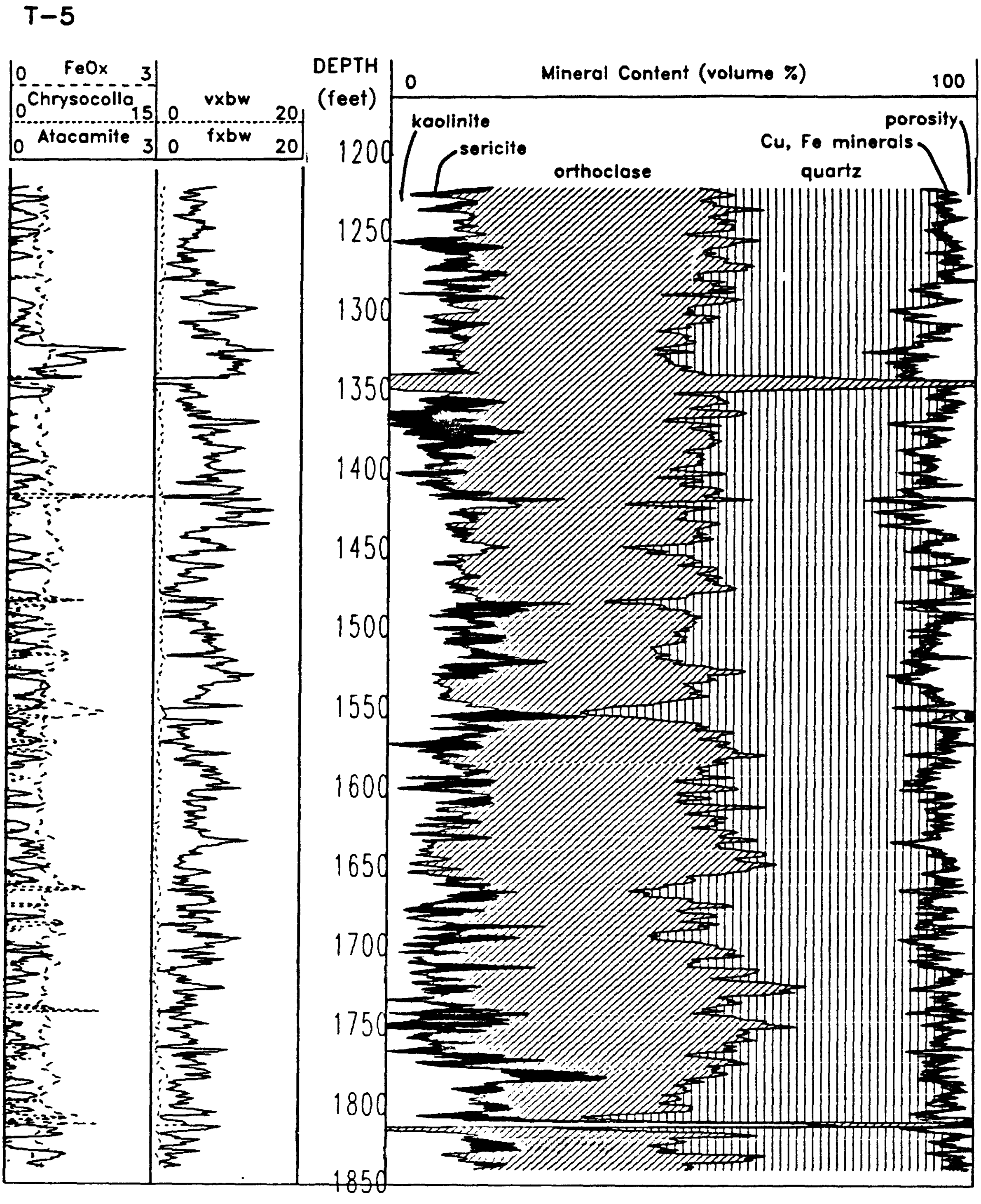

Figure 22. Mineral volumes in well T-5 computed from elemental weight percents, with calcium set to zero. Shown at expanded scale in left two tracks are volume percents of iron oxides, chrysocolla, atacamite, bound water, and porosity.

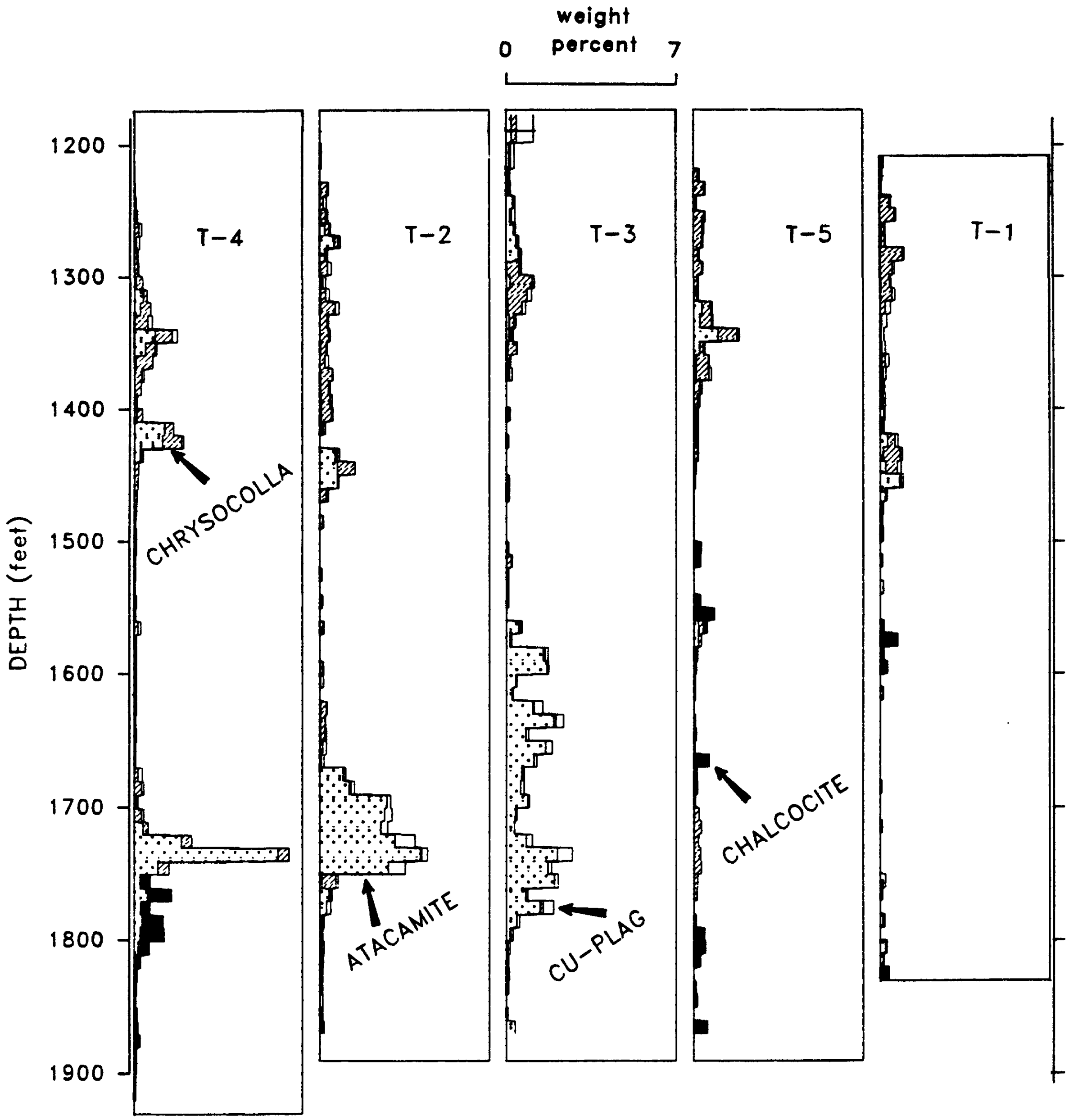

Figure 23. Weight percent copper by assay on cuttings from five T-wells, apportioned among four copper-bearing minerals.

T-3

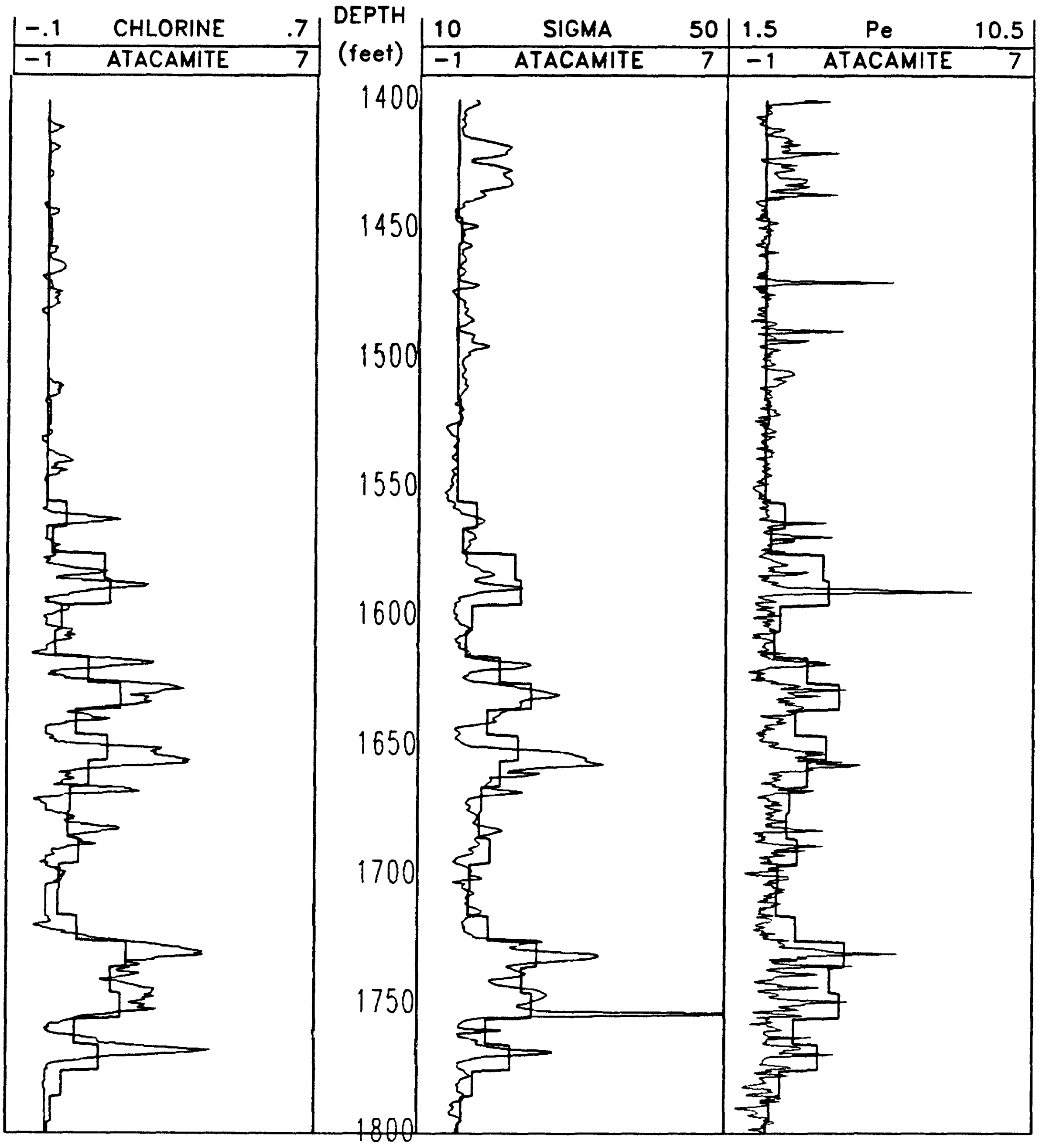

Figure 24. Atacamite distribution and three logs from lower part of hole T-3. Chlorine yield (cchl) is from the GST tool; capture cross-section (sigma) is from the TDT tool, and photoelectric absorption (pef) is from the LDT tool.

T-3

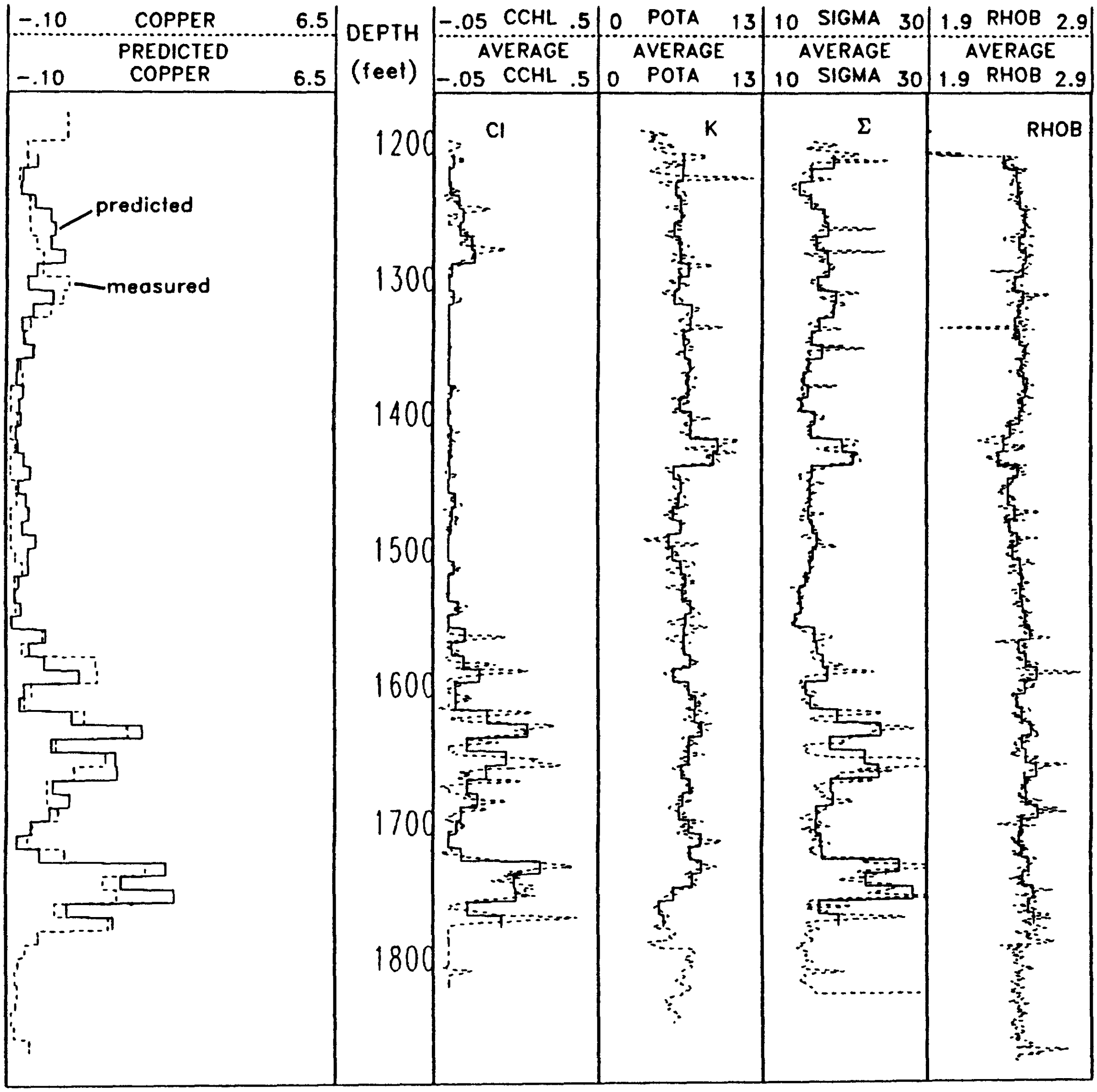

Figure 25. Predicted and measured copper from well T-3, shown with four logs, original and averaged, used to form the regression equation.

T-4

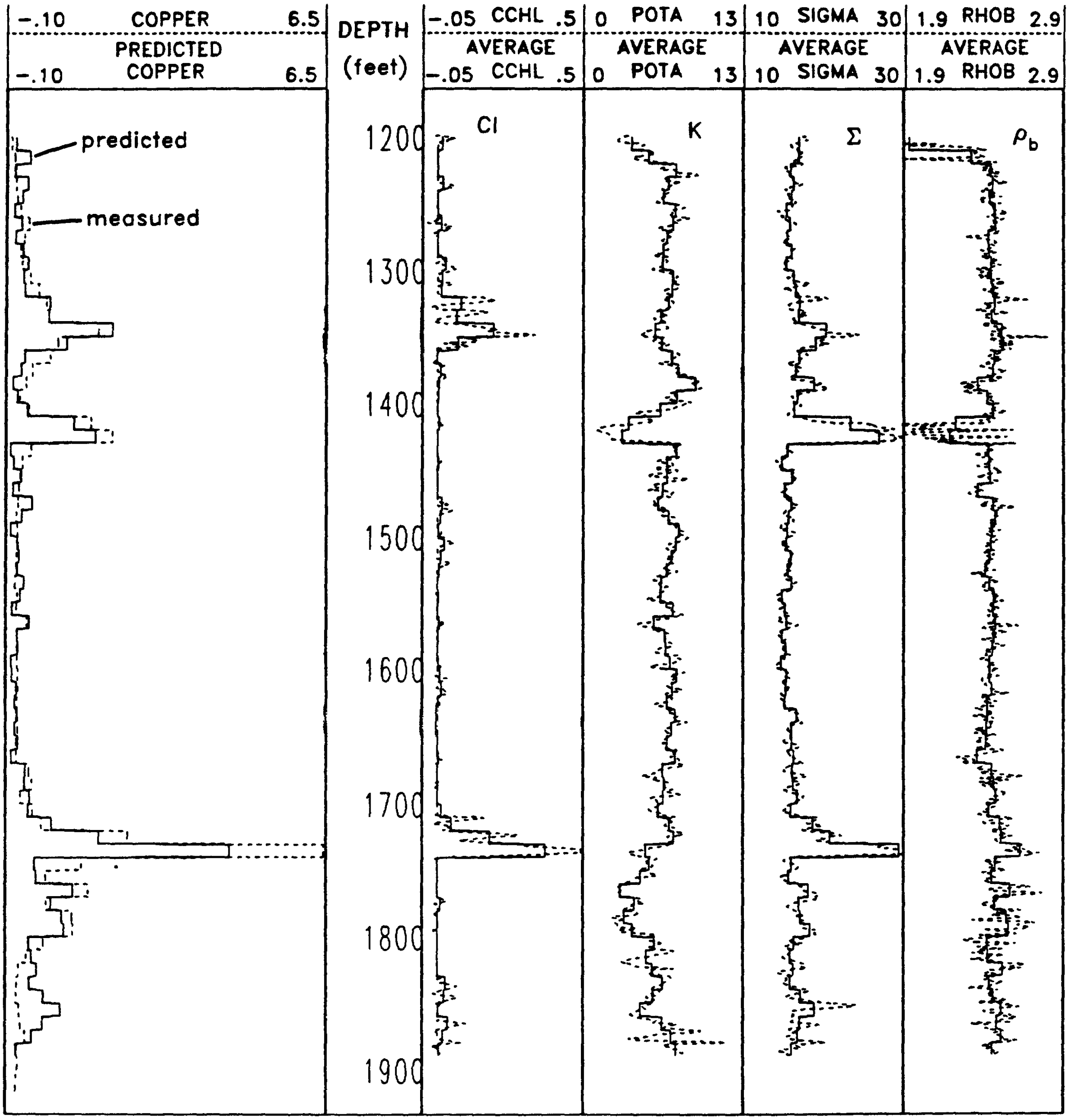

Figure 26. Predicted and measured copper from well T-4, shown with four logs, original and averaged, used to form the regression equation.

T-1

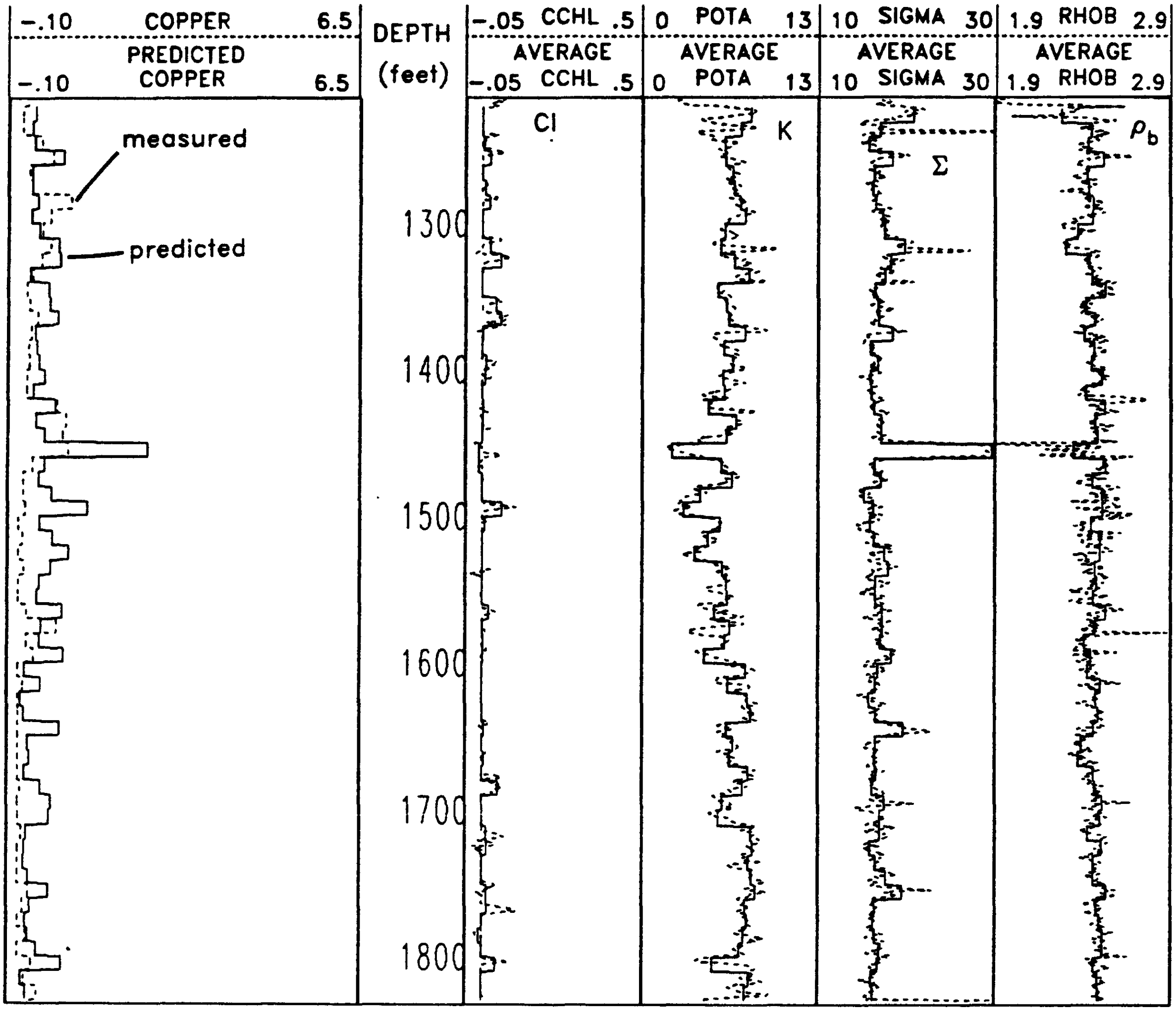

Figure 27. Measured copper and predicted copper in well T-1. Predicted copper utilizes regression equation based on data from wells T-3 and T-4.

T-5

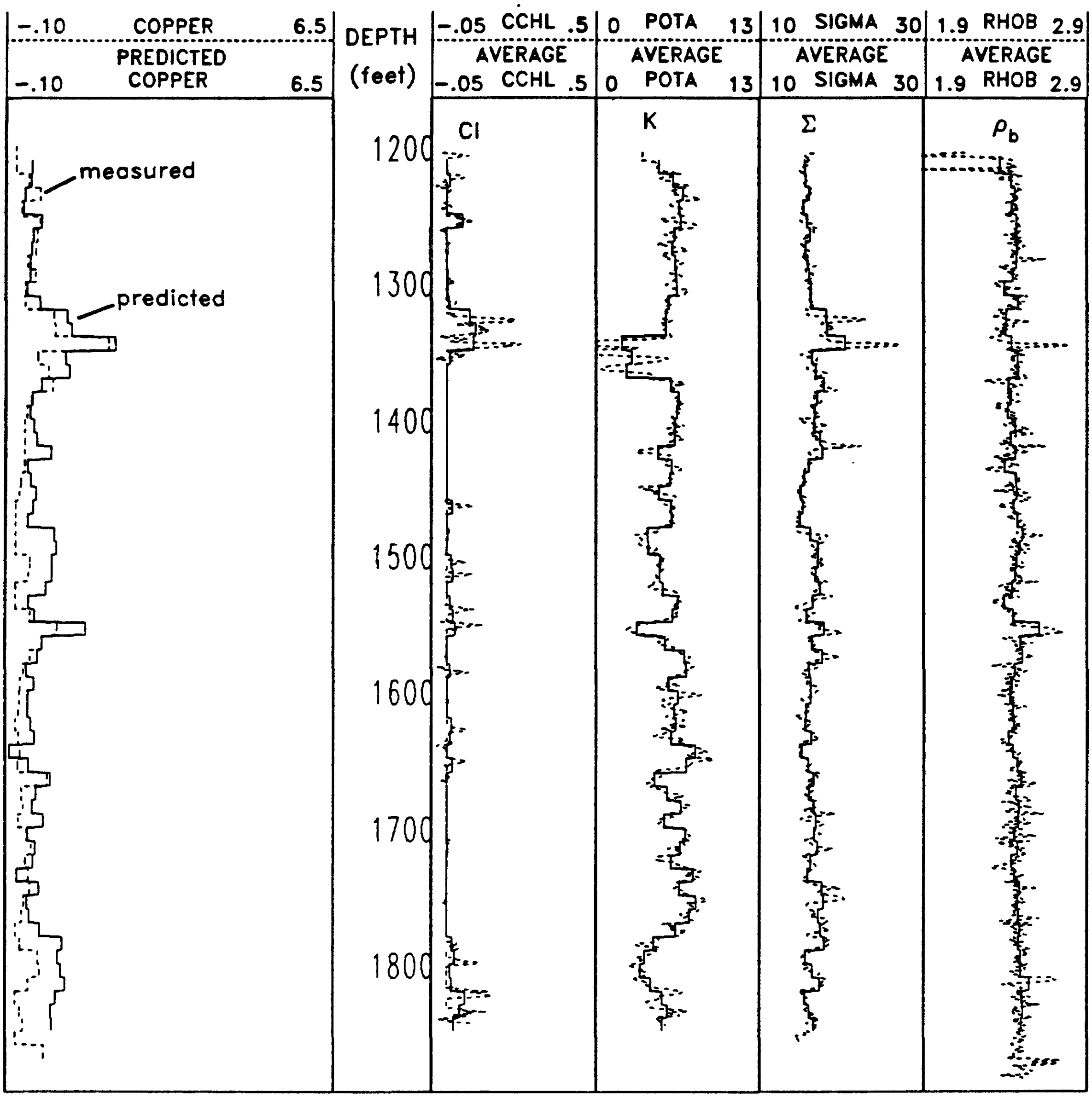

Figure 28. Measured copper and predicted copper in well T-5. Predicted copper utilizes regression equation based on data from wells T-3 and T-4.

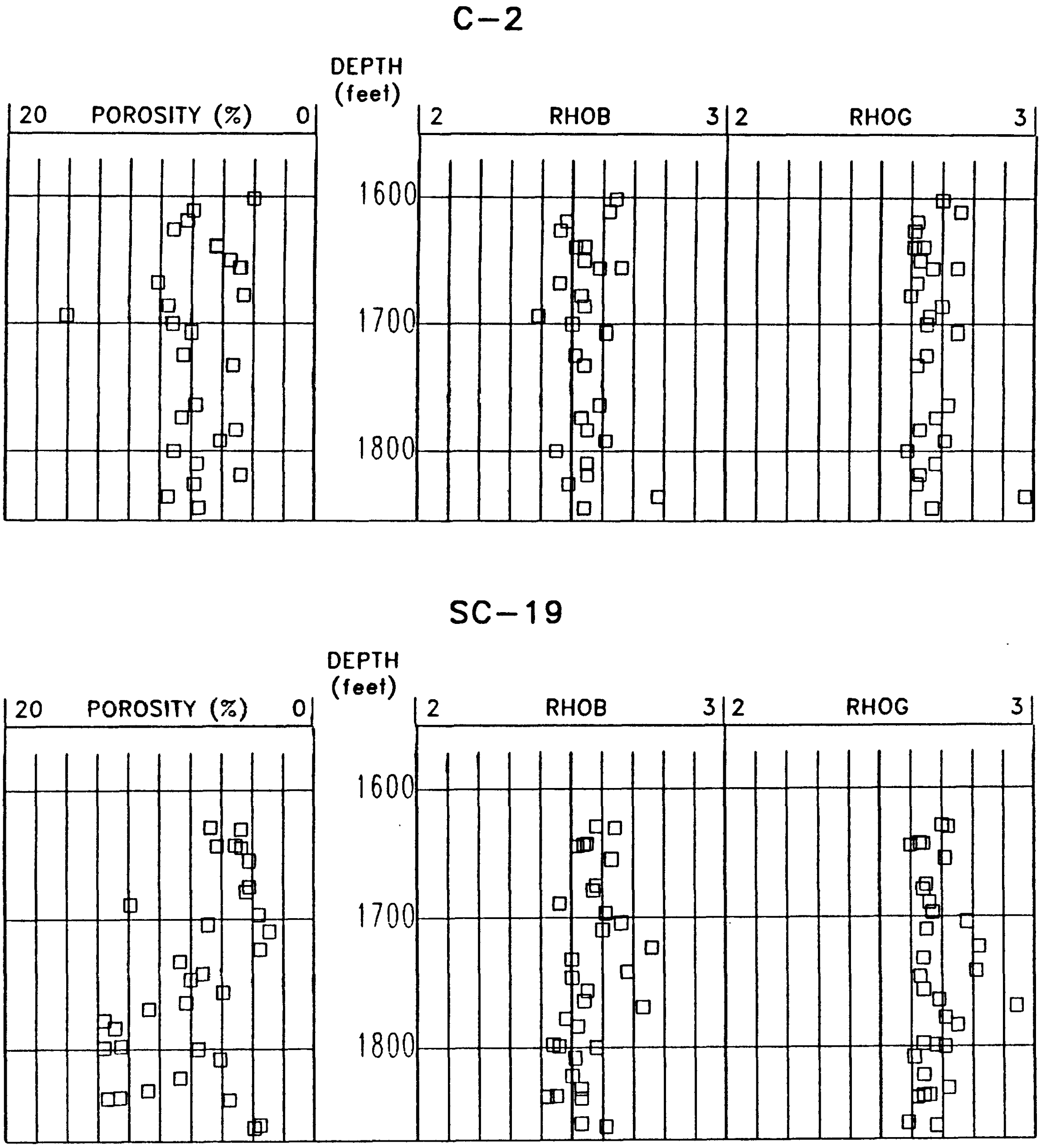

Figure 29. Porosity, saturated bulk density (rhob), and grain density (rhog) of core samples from holes C-2 and SC-19.

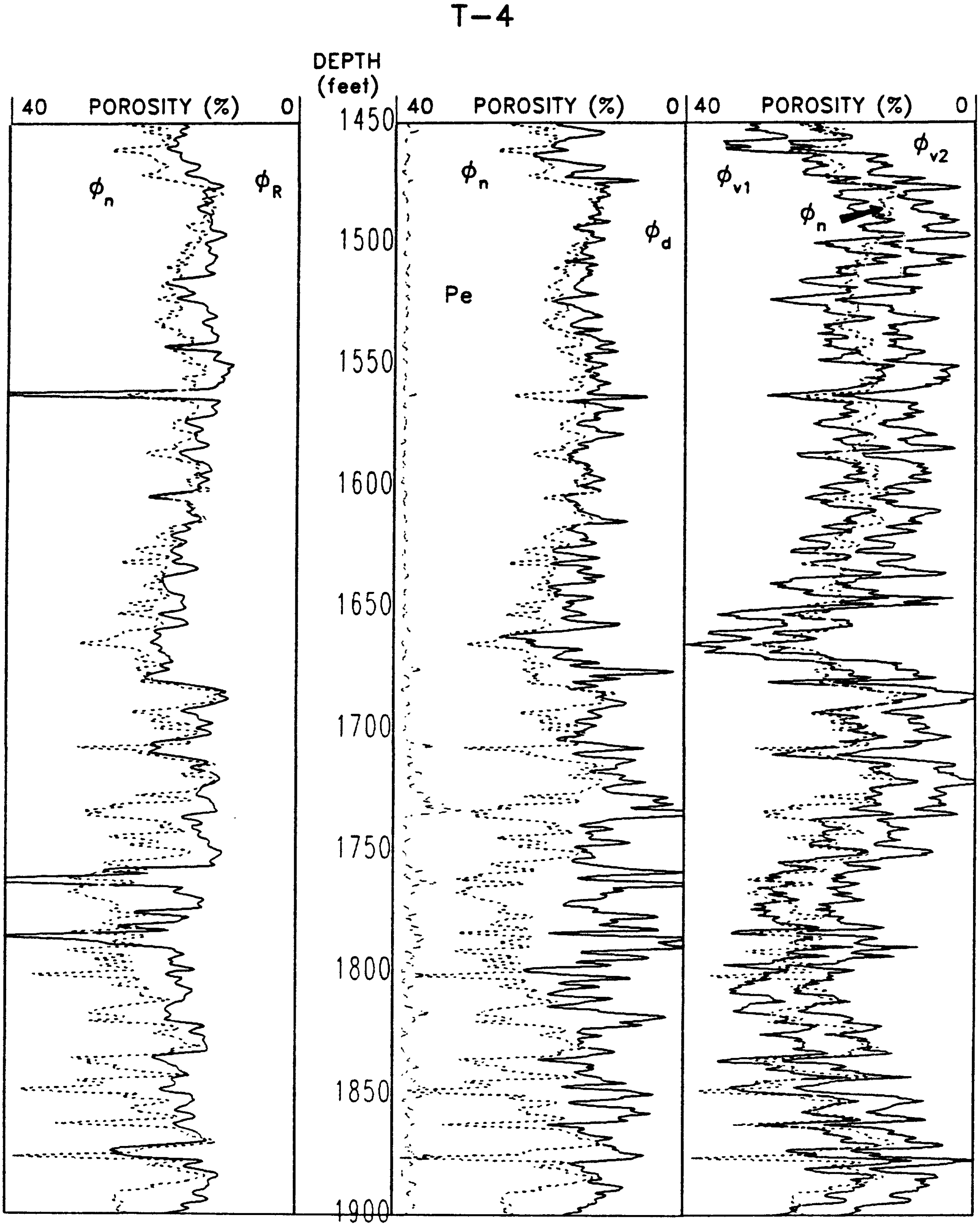

Figure 30. Porosity from thermal neutron log (ϕ_n, shown in all three tracks), and computed from resistivity (ϕ_R), density (ϕ_d), and sonic velocity logs. The two sonic velocity curves assume no clay (ϕ_{v1}) and a clay content of 13% (ϕ_{v2}). Photoelectric (Pe) log is shown in track 2.

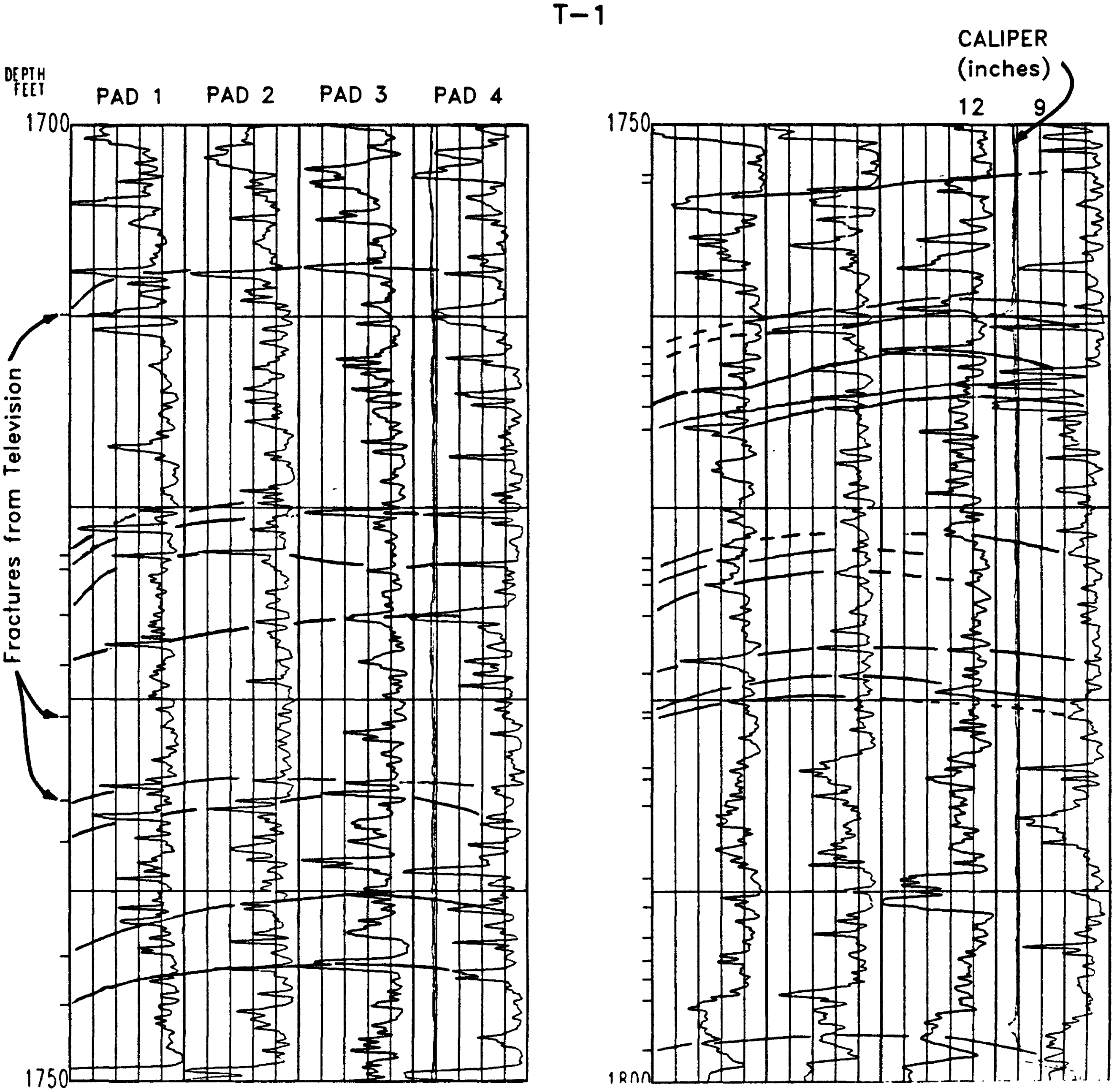

Figure 31. Electrical response in hole T-1 from four dipmeter pads, with conductivity increasing to the left. Fractures detected with borehole television are shown as ticks in the depth column. Four-arm caliper from dipmeter tool is also shown.

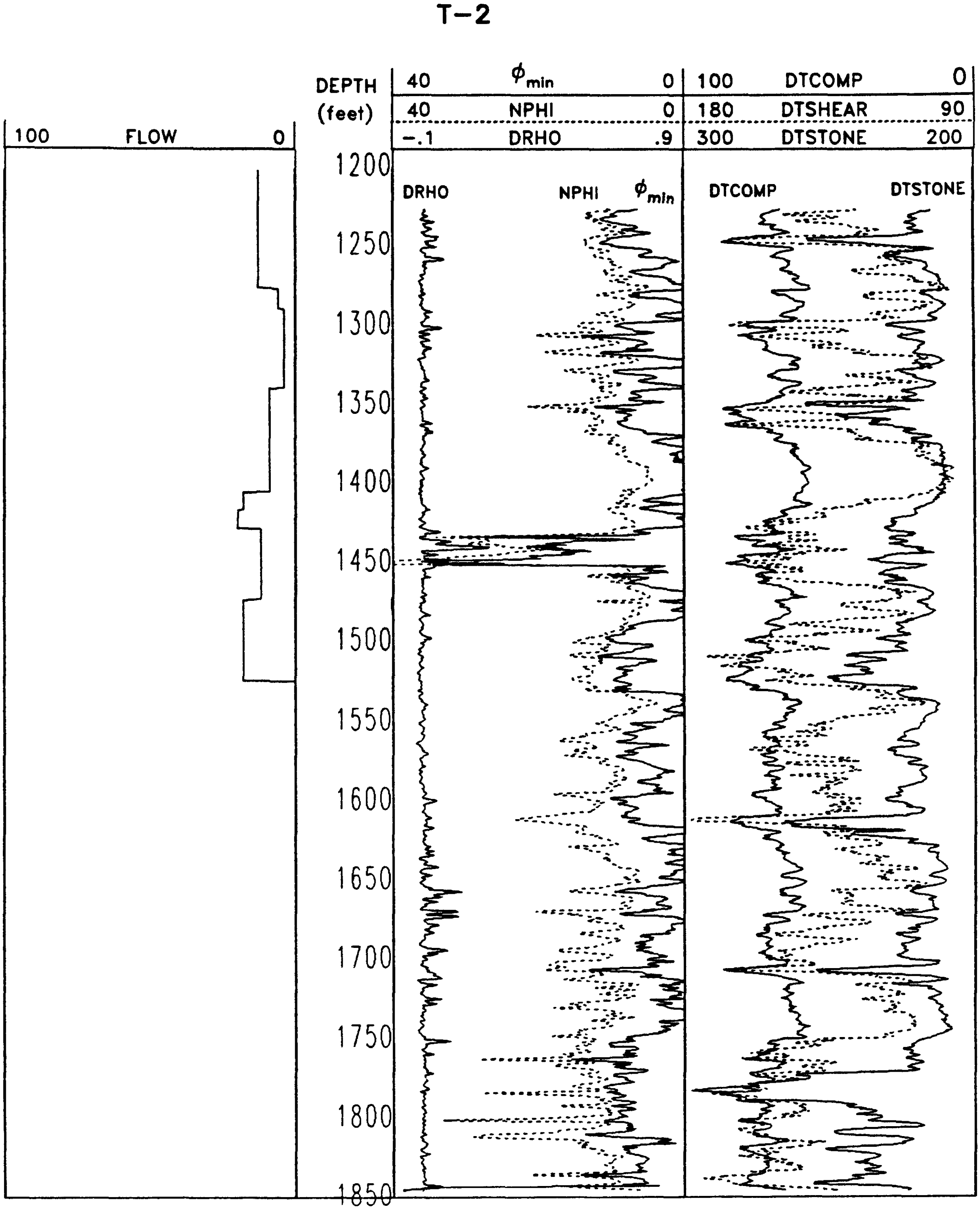

Figure 32. Flow log (percent of total flow) from hole T-2 obtained with diverter flowmeter, shown with density correction (drho), thermal neutron porosity (nphi), porosity calculated with mineralogy (ϕ_{min}), and sonic travel time from compressional (dtcomp), shear (dtshear), and Stoneley (dtstone) arrivals.

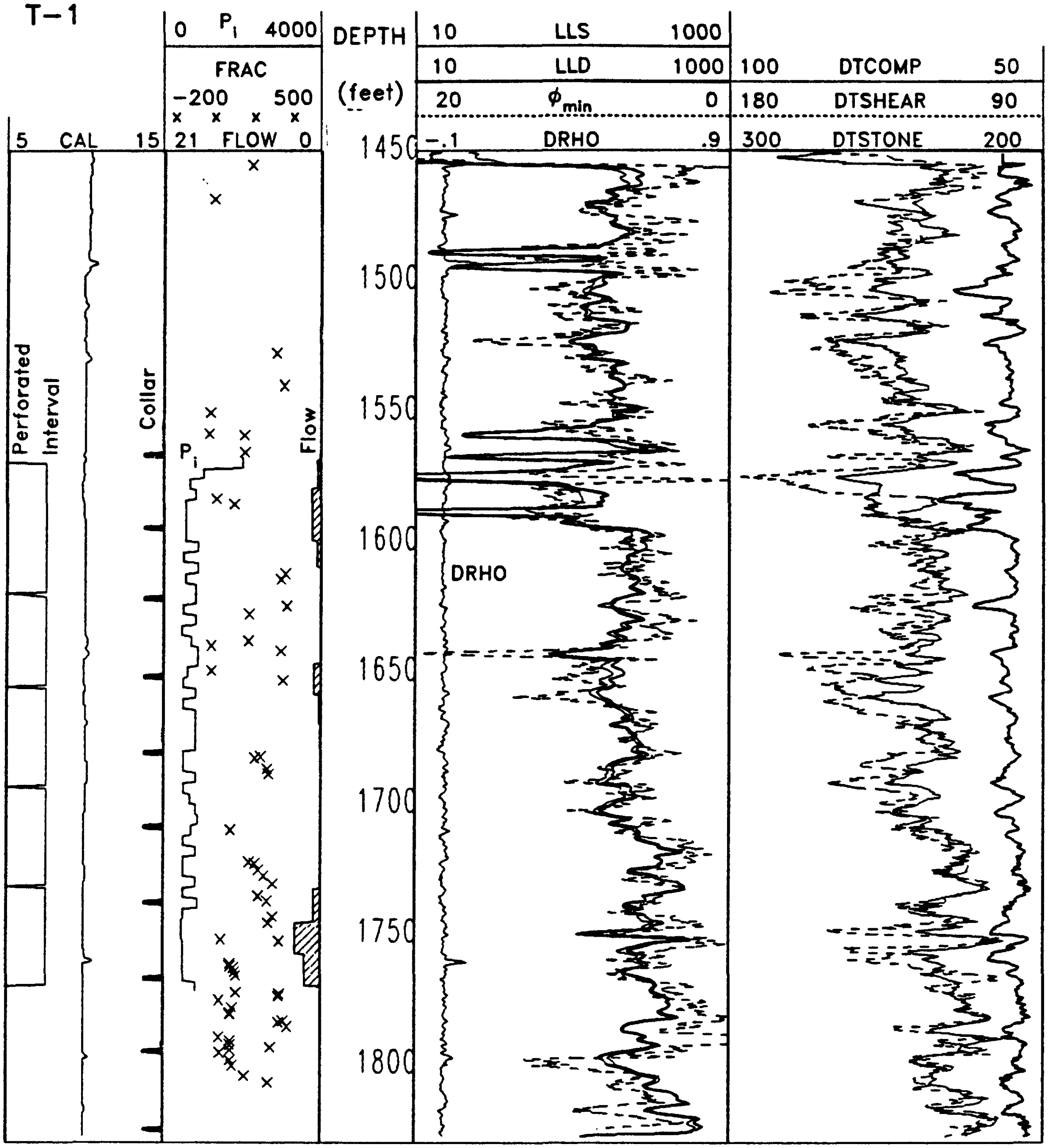

Figure 33. Flow log from full-bore spinner (track 2), perforated intervals (track 1), pressure applied during acidization (P_i in track 2), fractures identified with borehole television (x in track 2), and several open-hole logs from hole T-1.

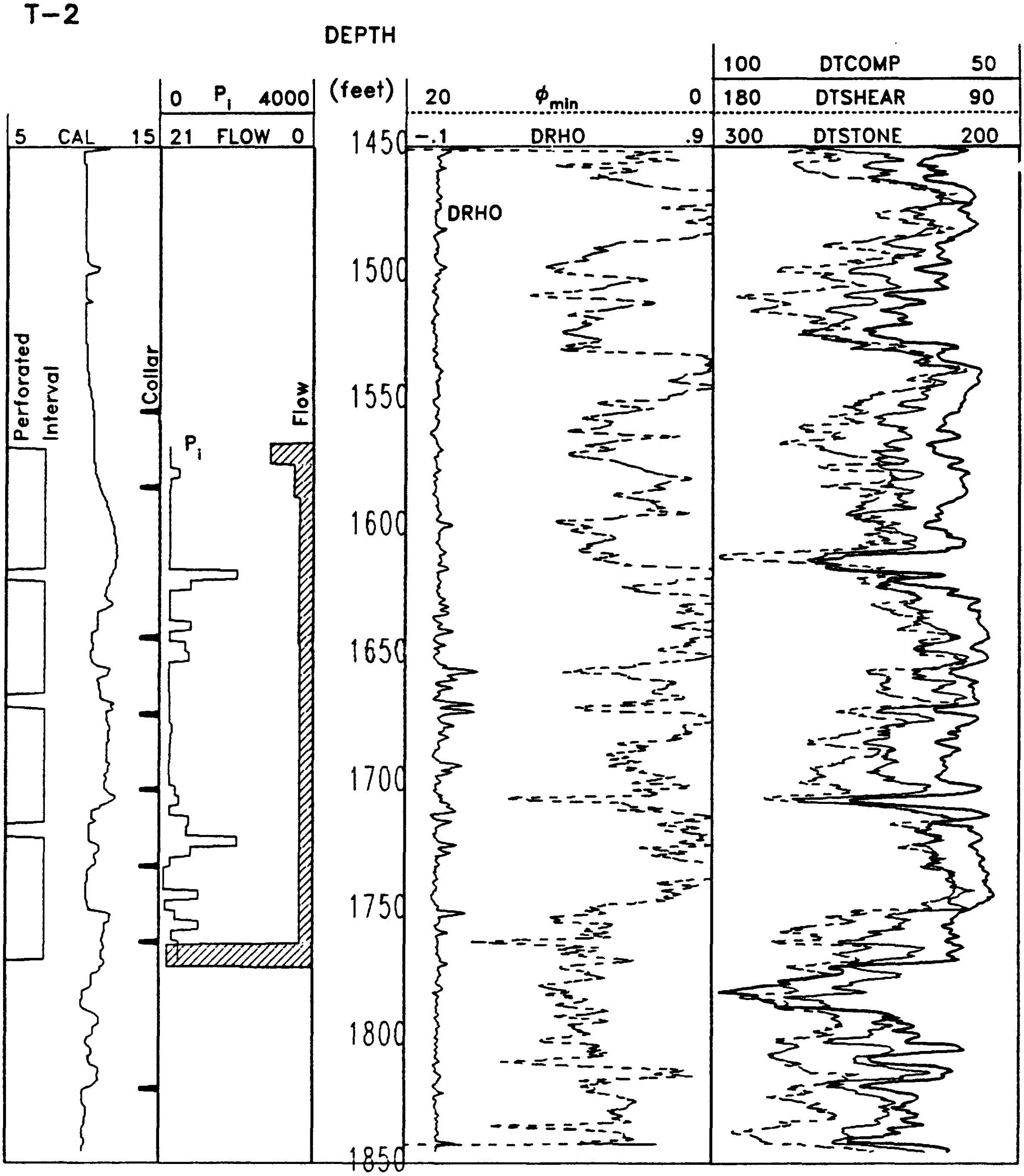

Figure 34. Flow log from full-bore spinner (track 2), perforated intervals (track 1), pressure applied during acidization (P_i in track 2), and several open-hole logs from hole T-2.

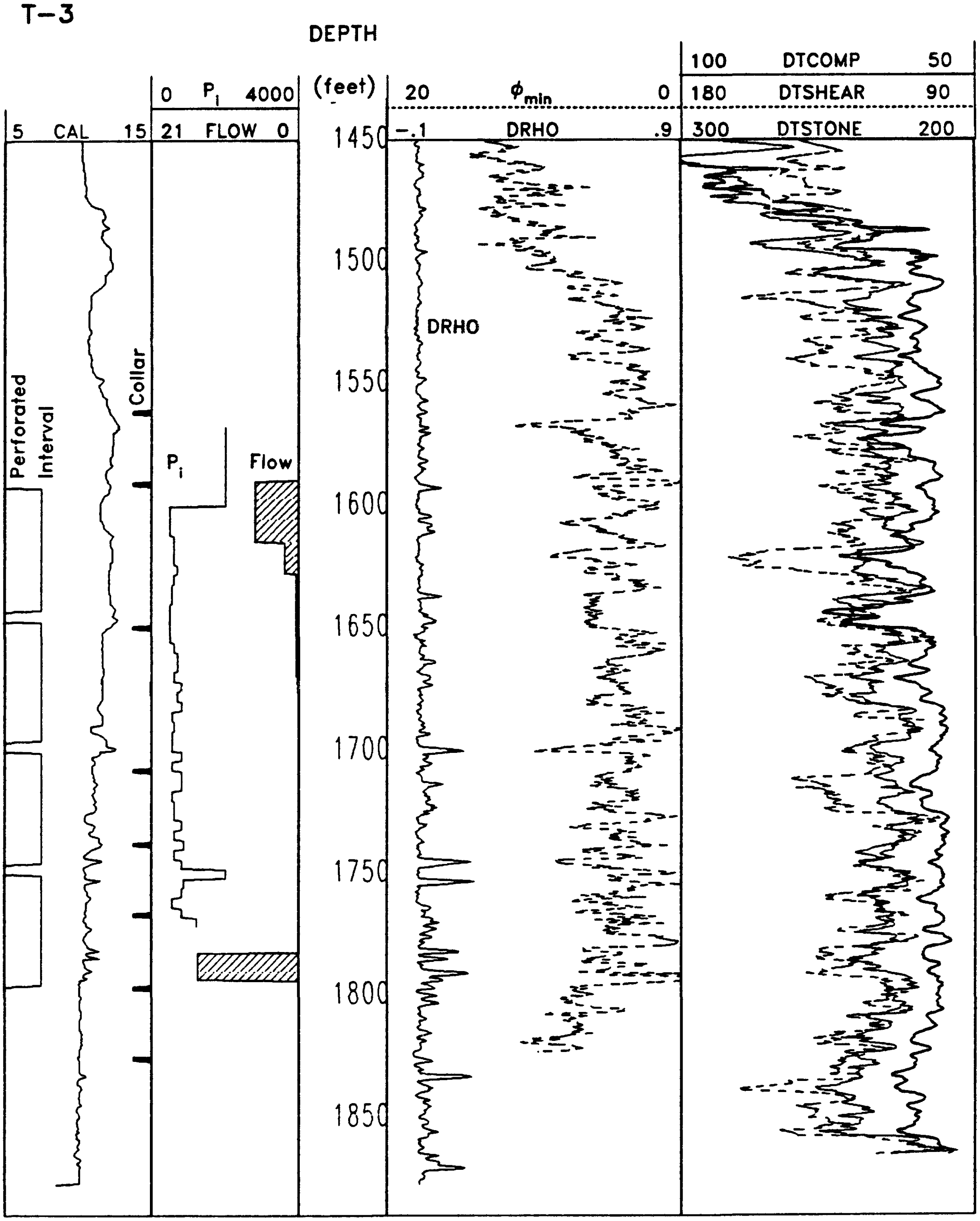

Figure 35. Flow log from full-bore spinner (track 2), perforated intervals (track 1), pressure applied during acidization (P_i in track 2), and several open-hole logs from hole T-3.

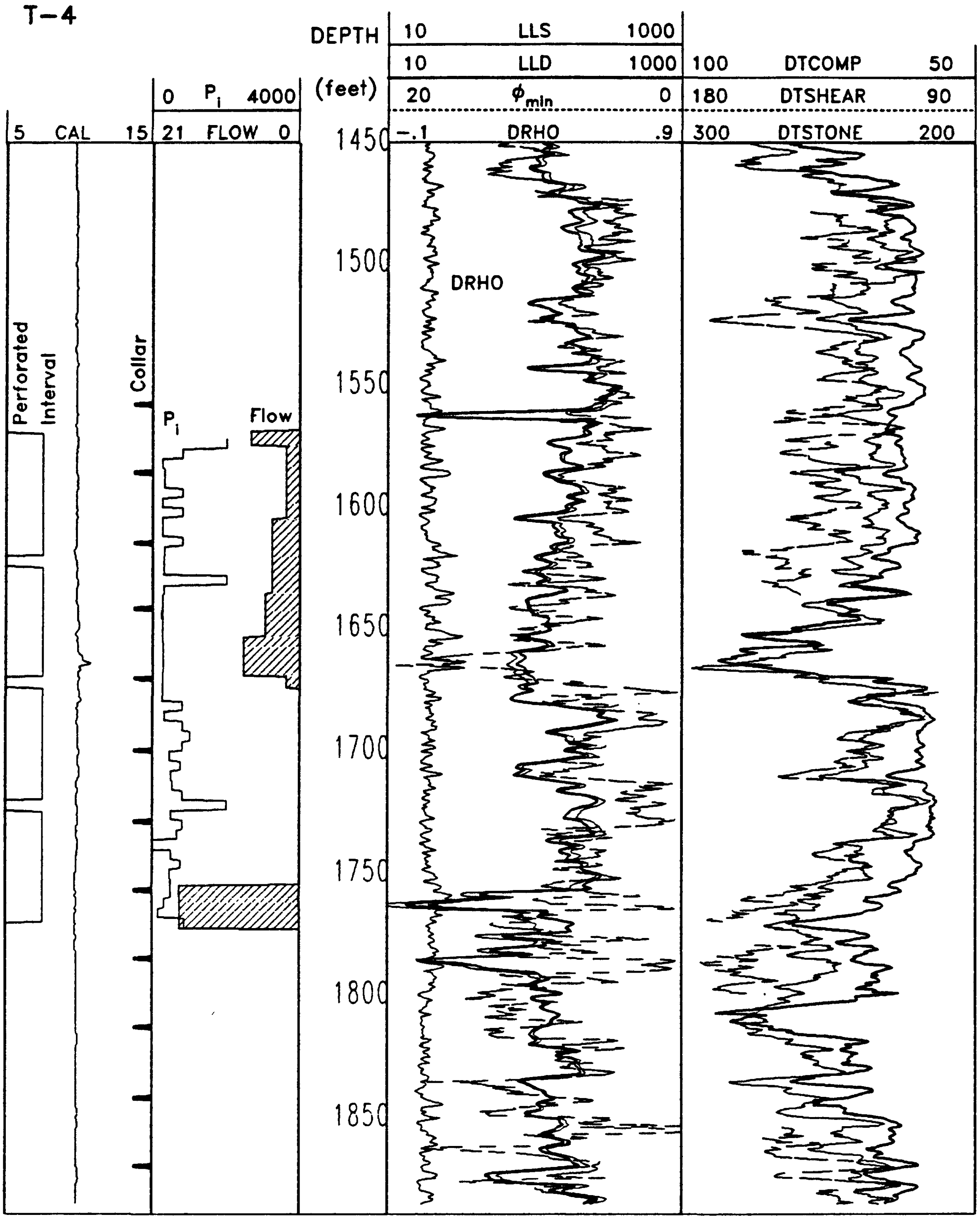

Figure 36. Flow log from full-bore spinner (track 2), perforated intervals (track 1), pressure applied during acidization (P_i in track 2), and several open-hole logs from hole T-4.

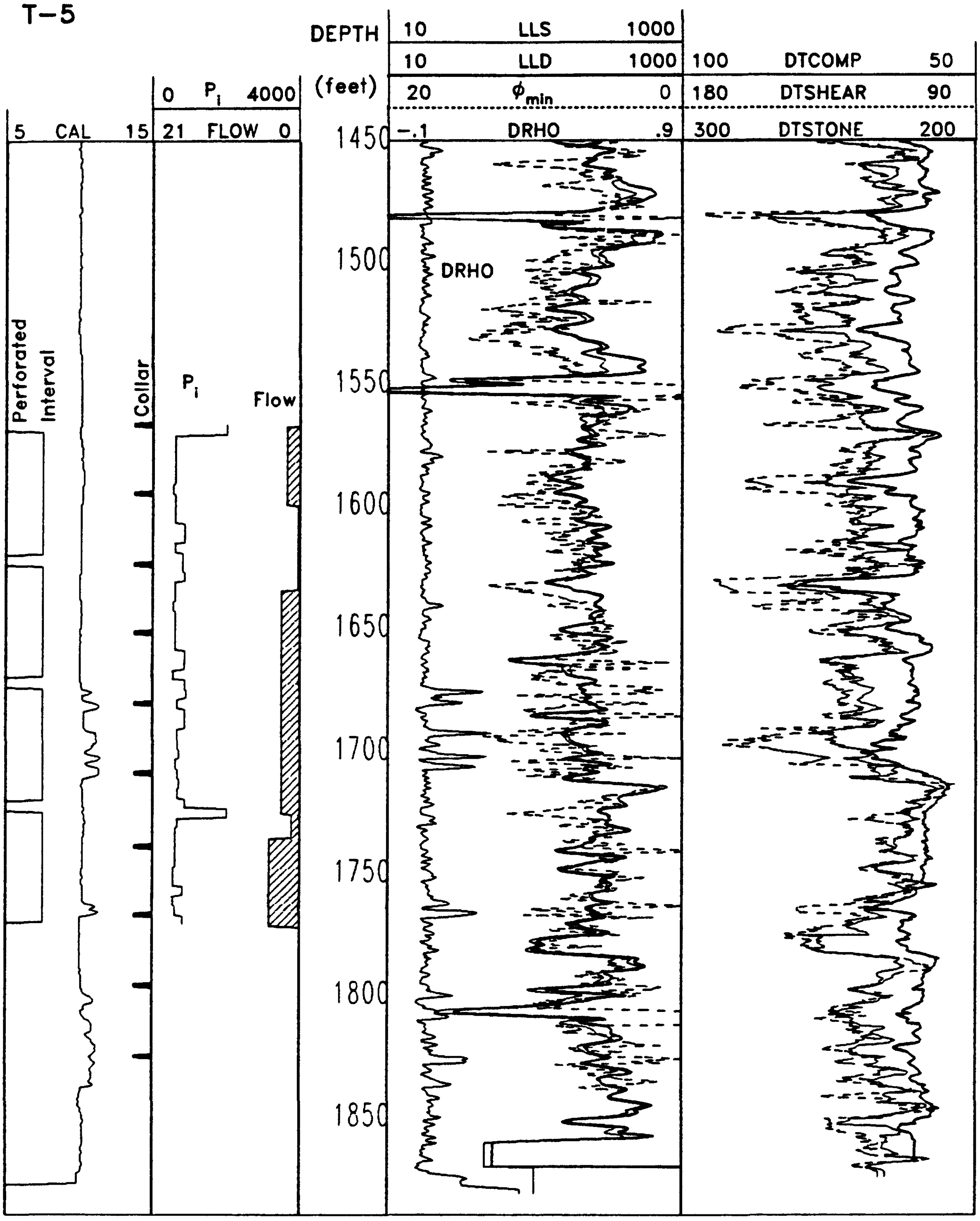

Figure 37. Flow log from full-bore spinner (track 2), perforated intervals (track 1), pressure applied during acidization (P_i in track 2), and several open-hole logs from hole T-5.

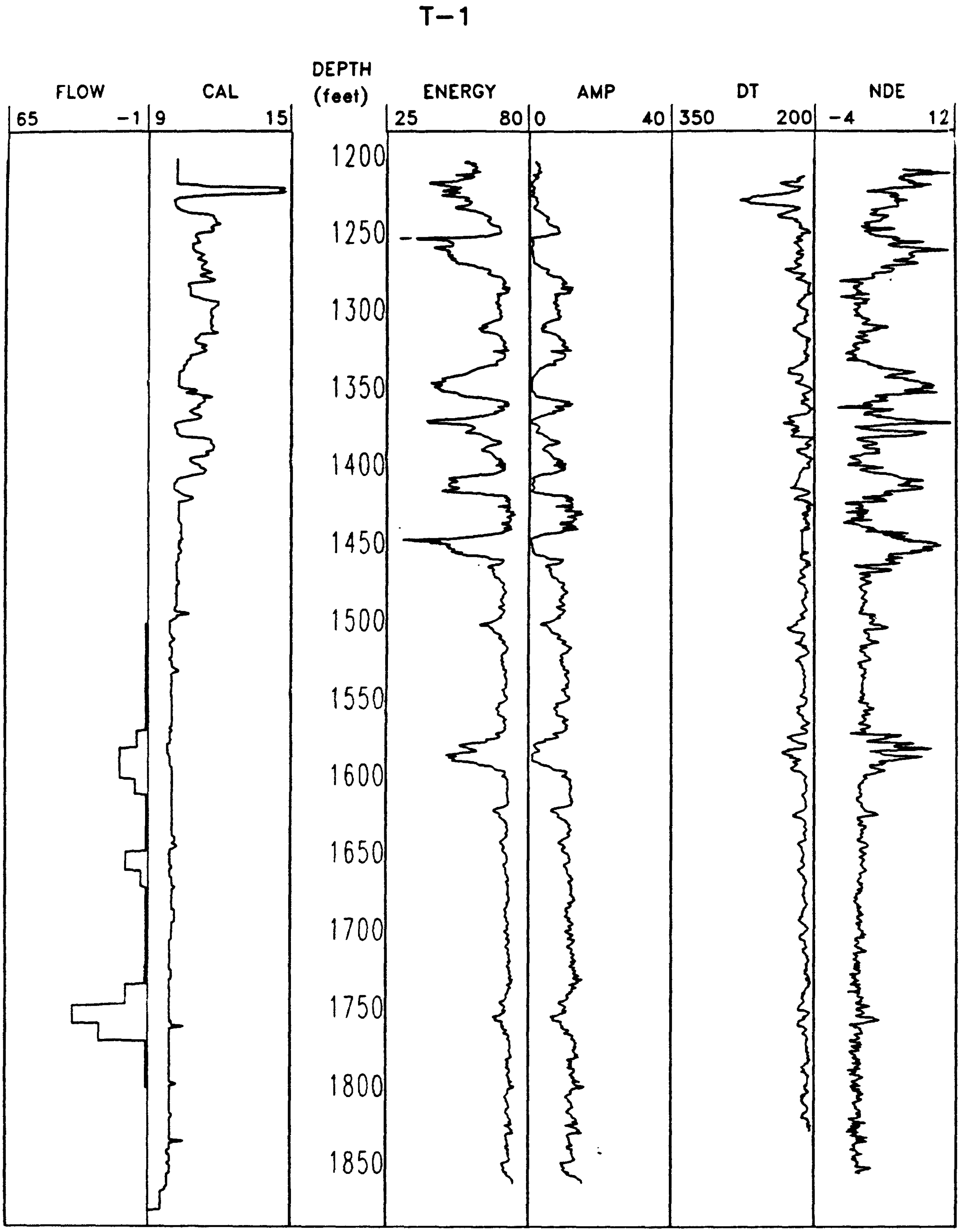

Figure 38. Stoneley wave energy in decibels, amplitude (amp), slowness (dt), and normalized differential energy (nde) from well T-1, along with caliper and percent flow from injection test.

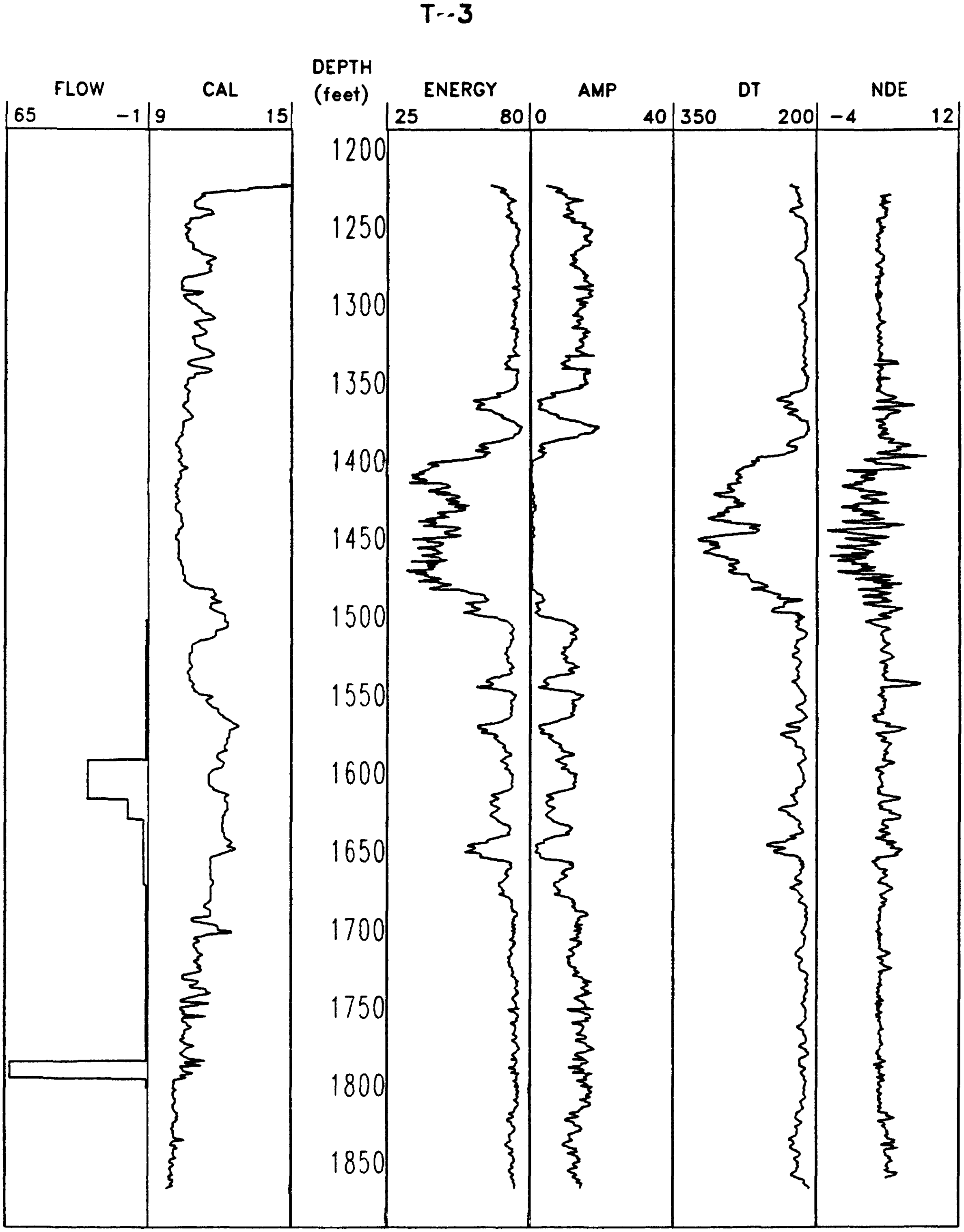

Figure 39. Stoneley wave energy, amplitude, slowness, and normalized differential energy from well T-3, along with caliper and flow profile.